PNAS
www.pnas.org

Supplementary Information for

Lifetimes of interstellar dust from presolar silicon carbide cosmic-ray exposure ages

Philipp R. Heck, Jennika Greer, Levke Kööp, Reto Trappitsch, Frank Gyngard, Henner Busemann, Colin Maden, Janaína N. Ávila, Andrew M. Davis, Rainer Wieler

Philipp R. Heck
Email: prheck@fieldmuseum.org

This PDF file includes:

Supplementary text
Figs. S1 to S8
Tables S1 to S5
References for SI reference citations
Datasets S1 (SEM images of samples with geometric measurements)

www.pnas.org/cgi/doi/10.1073/pnas.1904573117

Supplementary Information Text

Methods and extended data discussion

Samples. The large presolar SiC are from the original so-called "LS+LU" separation from the Murchison meteorite performed at the University of Chicago (1). Large SiC grains are extremely rare (<10 ppm by number of the SiC population from Murchison; (1)). The grains were transferred and placed widely spaced onto a clean gold foil with a micromanipulator at Washington University in St. Louis and subsequently pressed into the gold with a quartz disk.

Electron microscopy. Scanning electron microscopy and energy dispersive X-ray spectroscopy (SEM/EDS) was used to image and identify the samples. Grain volumes were estimated based on two-dimensional SEM images taken before and after SIMS analyses (SI Appendix). Because of the large size of the grains, and possibly also because of the better thermal contact of the angular SiC grains (compared to spherical graphite grains in (2)), heating with the electron beam during SEM imaging was negligible (cf. grain heating model in (2)).

Secondary ion mass spectrometry (SIMS). At Washington University in St. Louis isotopes of Li and C, N, Si were measured using O^- and Cs^+ primary ion beams, respectively. Isotope ratios for Li were normalized with analysis of a NIST-610 standard. All surfaces were pre-sputtered before analysis. On some samples spots at different positions were analyzed for Li isotopes. Li isotope data are discussed in more detail below. Grain heating during SIMS analysis was negligible (2). NanoSIMS analyses of C, N, Si were performed to classify the grains prior to Li and noble gas analyses (Table S2). The majority of the grains are mainstream SiC grains and three grains are of AB type SiC (Fig. S1).

Noble gas mass spectrometry. At ETH Zurich analyses of He and Ne isotopes were carried out with an ultra-high-sensitivity noble gas mass spectrometer equipped with a compressor ion source (3). We extracted noble gases with an IR laser in a ultra-low-blank extraction line specifically built to extract small gas amounts from small, µm-sized samples (4). For calibration we used an artificial gas mixture with amounts known to about 2% accuracy, as determined by laboratory cross-calibrations (5). The mass spectrometry system and extraction method are described in detail elsewhere (2–4, 6). We extracted noble gases by heating a sample with a ~60 µm laser spot for 210 to 240 s at 70–100% of the continuously adjustable output power; 100% = 16 W max. These conditions are sufficient to melt each SiC grain and completely degas its He and Ne. The detection limit is defined as twice the standard deviation (2SD) of all blanks of a run added to the mean blank value, as defined in Heck et al. (2). Average blanks and detection limits are given in Table S5.

Production rate calculation. Interstellar production rates for He, Ne, and Li isotopes are determined with the purely physical model from Trappitsch & Leya (7). This model uses a state-of-the-art nuclear cross-section database, i.e., experimentally determined cross sections are used when available, otherwise they were calculated with INCL4.5/ABLA07 and TALSYS-1.2 (see ref. (7) for details) and for the first time a full interstellar GCR energy spectrum based on data collected by NASA's *Voyager* space probe (8). The adopted production rates for ^{3}He, ^{21}Ne, ^{6}Li, and ^{7}Li are 317 ± 135, 40.8 ±

14.3, 165 ± 101, and 205 ± 85.7 × 10^{-10} cm^3 STP g^{-1} Ma^{-1}, respectively (standard temperature and pressure; 1 cm^3 STP = 2.6868 × 10^{19} atoms). Uncertainties of these production rates are based on the quality of the nuclear cross sections that were used for the calculations. Note that an uncertainty in the production rate will manifest itself as a systematic rather than a statistical uncertainty on the production rate and will be treated as such in this manuscript.

Recoil loss modeling. The physical recoil model is consistent with the production rate model, considers the full spectrum of GCR protons and alpha particles, and was first presented in Trappitsch & Leya (7). The recoil correction used in this study is based on less assumptions than previous corrections, e.g., (6, 9, 10). Therefore, we assume this physical recoil model to be more accurate. Trappitsch & Leya (7) assumed 50% uncertainties for all modeled recoil losses. Recoil losses were purely calculated and could not be compared over the whole range of the spectrum with measurements. Large grains loose only small amounts of the produced cosmogenic nuclides and, thus, only get a small contribution in their CRE age from the recoil loss uncertainties.

Uncertainties. In the following, we discuss several uncertainties that were not propagated through the data processing. 1. In order to determine grain volumes we used two-dimensional SEM images of grains pressed into the gold. From these images we obtained the geometric cross-section of the grain and assumed that the third dimension of the grain is equal to the smallest axis of the cross-section. In the absence of a three-dimensional analysis this is the best estimate for estimating a volume. Using the density of SiC (~3.2 g cm^{-3}; (1)) the mass of the grains was calculated. We estimate the mass uncertainty from this method to be ~1.5×. The grains were pressed into the substrate long before these samples were designated for this study. 2. Uncertainty of the presolar, interstellar GCR spectrum. The difference of the Voyager 1 spectrum (8) to the one outside of heliosphere is probably negligible for our production rates. 3. We do not give an uncertainty for the presolar GCR flux as no uncertainties for the GCR flux before 4.6 Ga is available. Based on studies of iron meteorites, e.g., (11), the samples with the longest exposure ages in the solar system, there is no indication that the average GCR flux in the past was different compared to today.

Ages calculated via ^{3}He tend to have large uncertainties, since ^{3}He has large recoil ranges and can be easily lost at typical presolar grain sizes. Since ^{21}Ne is the heaviest cosmogenic nuclide discussed in this paper, and thus has the smallest recoil losses at a given grain size, it will also have the smallest contribution to the overall uncertainty. As for the production rates, recoil loss uncertainties are also systematic errors and are shown in Fig. S2.

Another assumption of the correction is that the grains were spherical. While none of the SiC grains analyzed is spherical, most are reasonably approximated by a spherical envelope. If the third dimension of the grains was smaller than estimated, which could be the case for several of our samples, this would lead to an undercorrection of the recoil loss, opposite to the nominally higher ^{3}He ages than ^{21}Ne ages that we observe for many grains (Fig. 2 and Fig. S3).

Calculation of He and Ne exposure ages. Because there are three main Ne components in presolar SiC from AGB stars and three stable Ne isotopes, we can, therefore, determine the fractions of each component (Fig. S8): air (12), cosmogenic (7, 13), and nucleosynthetic Ne-G (4), as shown in (6). In addition to the presolar cosmic-ray

exposure, the grains were also exposed in the solar system during the transit of the Murchison meteoroid from its parent asteroid to Earth. This meteoroid exposure age is ~1.6 Ma (14) and is so low that it is negligible compared to the uncertainties of the presolar exposure ages.

We estimate the exposure of the analyzed presolar SiC grains to enhanced solar cosmic rays (SCR) of the early active Sun. The large presolar SiC grains, except for the largest aggregates, are smaller than hibonite grains of Kööp et al. (15), thus increasing the probability for them to be transported to or above the surface of the disk, e.g., (16). We assume as an upper limit the highest measured cosmogenic Ne concentration in hibonite (15), adjusted for the different production rate in silicon carbide. We obtain an upper limit of 2×10^{-7} cm^3 STP (gas volume at standard temperature and pressure; P=101,325 Pa; T= 273.15 K; 1 cm^3 STP = 2.6868×10^{19} atoms; (17)) if the cosmogenic ^{21}Ne came from exposure to solar cosmic rays in the early solar system (Fig. S7). We do not correct the cosmogenic nuclides for the possible early solar system exposure of presolar grains to energetic particles from the early active Sun. As discussed above, it is unclear to what extent, if at all, the grains studied here were exposed. More importantly these effects are mostly negligible as discussed in the main text. Due to these uncertainties we do not correct for early solar system exposure.

The composition of the implanted AGB star neon in mainstream SiC (Ne-G) is well understood. No other nucleosynthetic components are detectable in single SiC grains from AGB stars. No envelope Ne (Ne-N) was detected, nor is Ne from other stellar sources, Ne-R or Ne-HL, present, see (18) for current definitions of these components. Almost pure ^{22}Ne formed in AGB stars by α-capture reactions: ^{14}N(α, γ)^{18}F(β+)^{18}O(α,γ)^{22}Ne (19). Isotopic compositions of Ne-G are reported in Heck et al. (4). The composition of Ne-G in J-type C-stars, which are possible sources of AB grains (20–22), is not specifically known but probably not very different to the He-shell Ne of the parent stars of mainstream grains. We have shown in earlier work that the choice of the He-shell Ne composition has only a small effect on the Ne exposure age of the large SiC grains studied here (6). This is mainly because the fraction of Ne-G in large grains is small compared to µm-sized grains (Fig. S5b). So, even if the Ne-G composition of J-type C-stars would be slightly different than for the mainstream SiC parent AGB stars, the effect on the ages of these grains, L2-27 and L2-57, would be small. Therefore, and for practical purposes, we assume the same Ne-G for J-type C-stars as for AGB stars. Liu et al. (23) recently suggested that ^{15}N-rich AB grains are from core-collapse supernovae (Type II SN). Our AB grains were consumed by analyses before the Liu et al. paper came out and were not measured for N isotopes. We therefore can neither rule out nor confirm if these two grains are from J-type C-stars or from Type II SN. If they are from Type II SN we currently cannot estimate a cosmogenic component, as the nucleosynthetic Ne input from Type II SN can vary by orders of magnitude, depending of the degree of mixing of Ne from different SN zones (24).

The new production rates for ^{3}He and ^{21}Ne ($[3.17\pm1.35]\times10^{-8}$ cm^3 STP g^{-1} Ma^{-1} and $[4.08\pm1.43]\times10^{-9}$ cm^3 STP g^{-1} Ma^{-1}, respectively) are similar to those determined earlier (4.15×10^{-8} cm^3 STP g^{-1} Ma^{-1} and 5.60×10^{-9} cm^3 STP g^{-1} Ma^{-1}, respectively; reported in (6) based on Reedy (13).

We bear in mind that the large SiC grains studied here are not necessarily representative of much smaller, more abundant interstellar dust on the nanoscale, such as

nanodiamonds, silicates, nanooxides, and presolar organic matter. Large SiC is currently the only type of presolar matter that can be dated. Dust grains smaller than the ones studied here have nuclear recoil losses that are too large to obtain useful exposure ages, except for Xe (25), which is currently not detectable in such grains. Although most of our ages are similar to the nominal bulk SiC ages published by Ott et al. (25) comparing our data directly with the bulk age estimates is not really useful even though both studies report predominantly young ages. The agreement might not have a physical meaning, because at the time of publication of (25) production rates of cosmogenic Xe were not well known (7) and very likely unknown amounts of nucleosynthetic Xe from supernovae, something that hasn't been corrected for in (25), were in the analyzed bulk SiC samples that would skew the average bulk Xe age and only by chance match our ages. Amounts of radionuclides in nanograins are even lower than in large grains. This makes both approaches, exposure age and radionuclide dating, not yet feasible for nanograins. Therefore, presolar exposure age dating on large SiC grains is currently the only technique that provides age information of individual interstellar grains.

Li isotopes. Apart from noble gases, Li is the most promising element to possibly detect a cosmogenic component in the grains studied here, due to its very low natural abundance in presolar SiC. Gyngard et al. (10) published interstellar exposure ages of nine SiC grains from Murchison, ranging from about 40 to 1000 Ma. In this work, we attempted to determine Li-based exposure ages on a subset of the grains, on which subsequently He and Ne were measured. Analytical techniques (see Materials and Methods section) were identical to those described by Gyngard et al. (10). The Li NanoSIMS analyses carried out prior to the noble gas measurements consumed only small <1‰ volume fractions. On many grains two or three different spots were analyzed at different positions (see Table S4).

The measured Li isotope data require several critical corrections in order to obtain the cosmogenic fraction of ^{6}Li (10). The first is a correction for isotopic fractionation of the ^{7}Li/^{6}Li ratio on the order of ~8%, as determined with standard analyses on a synthetic SiC grain (measured ^{7}Li/^{6}Li ratio is 11.5±0.1, compared to the chondritic standard value of 12.06±0.03); (26). Second, to convert ion beam intensities into Li concentrations, analyses of a polished glass standard (NBS 610) were used (average measured ^{7}Li/^{6}Li ratio is 12.1±1; n=83), as no suitable SiC standard exists. This may lead to uncertainties that are difficult to quantify. Third, because only Li residing in the uppermost < 1 μm of a grain was analyzed, the relevant recoil loss for Li is larger than it would be calculated for noble gases where the gas amounts from the entire grain are measured. Fourth, and presumably most importantly, a very large correction for noncosmogenic Li is required, see (10): The cosmogenic ^{7}Li/^{6}Li ratio is 1.2 (7), whereas for all noncosmogenic Li in the grains we assume the chondritic or "solar system" ratio of 12.06±0.03 (26). This assumption appears justified, since it is unlikely that the grains contain substantial amounts of Li from their parent stars or the interstellar medium. It is also likely that the noncosmogenic Li in the grains represents contamination from the meteorite parent body or the grain handling. However, the exact ^{7}Li/^{6}Li ratio of the noncosmogenic Li is crucial, since measured ^{7}Li/^{6}Li ratios in all analyses differ by less than 20% from the assumed value of 12.06±0.03 for noncosmogenic Li. The lowest measured ratio is 9.8 (analysis "L3-17_spot_2, Table S4), but most values range between about 11 and 12, and some ratios even exceed the assumed 12.06±0.03 value for noncosmogenic Li by more

than their 1σ uncertainty. These analyses thus lead to formally negative Li exposure ages. We use the production rates given in Trappitsch & Leya (7).

The following discussion is based on the ages not corrected for recoil, i.e., recoil-corrected nominal Li ages will be even much higher. Nominal ^{6}Li exposure ages are given in Table S4. Values vary between –324 and 4300 Ma. Apart from the several negative age values there are other observations which clearly indicate that the nominal Li exposure ages shown in Table S4 are problematic. First, for many grains with more than one analysis, nominal ages from different spots vary by large factors. Extreme cases are L3-05 with one value being –59±36 Ma, the other +4300±2600 Ma, L3-14 with +210±130 and +2200±1400 Ma, respectively, or L3-08 with +200±120 and +2000±1200 Ma, where the nominal cosmogenic Li excess is >2σ for both spots. The sheer facts that different spots of the same grain yield highly discrepant ages and that some analyses yield higher ^{7}Li/^{6}Li ratios than our adopted value for noncosmogenic Li show that there are some unresolved problems with these nominal ages. In some cases, the largely different ages still agree within their very large uncertainties, the uncertainties largely being the result of very large corrections for noncosmogenic Li. However, Fig. S4 shows that nominal Li exposure ages correlate with Li concentrations. The four analyses that have the highest ages (L3-05_spot2, L3-08_spot2, L3-14-spot2, and L3-47_spot1) have the (by far) highest Li concentrations. While this may sound reasonable at first sight, this would actually only be expected if these grains would have lower measured ^{7}Li/^{6}Li ratios than other grains, i.e., much higher fractions of cosmogenic Li. This is not the case, strongly indicating that the correction for noncosmogenic Li is unreliable, as it is unreasonable to assume that grains with a high Li contamination (e.g., 1 ppm of ^{7}Li) have much higher exposure ages than grains with low ^{7}Li (e.g., 0.02 ppm). Hence, the correlation in Fig. S4 seems to be an artifact. Such a correlation is not observed for neon isotopes and neon concentrations.

This leads us to conclude that the present Li data cannot be used to determine reproducible exposure ages of these samples. In the future, we will use ion imaging to obtain data sets that can be better cleaned from areas contaminated by normal Li.

Determination of lifetimes of presolar grains parent stars

The ^{21}Ne-exposure age distribution of presolar SiC grains, shown in Fig S5a as a blue filled Kernel Density Estimation curve (KDE, bandwidth 36.1; ref. (27)) is the same as in Fig. 3 except that it is plotted here with a linear abscissa. Single steady-state model lifetimes $e^{-t/\tau}$ are shown in Fig S5a as dotted lines with average model lifetimes of τ=50, 100, 300 and 1000 Ma. It is evident in the figure that the observed age distribution cannot be explained by a single steady-state model lifetime. Adopting a short lifetime would leave the older grains unexplained, adopting a longer lifetime would not explain the overabundance of younger grains. Explaining the age distribution by a single steady-state process would require vastly different average dust lifetimes for SiC grains of similar sizes through time – something that is unlikely to have occurred and difficult to explain. A more natural explanation is the consideration that the overabundance of younger grains with presolar ages <300 Ma is the reflection of the combined action of grain destruction and grain formation in late stages of parent stars that formed in the most recent presolar peak of a moderately enhanced star formation rate (SFR). In Fig. S5a we show three different proposed SFR curves. Two of them (Noguchi (28) and Rocha-Pinto et al. (29)) show peaks of enhanced SFR around 7 Ga ago, which might represent the same event.

The Rowell (30) SFR curve shows a broad peak around 8.6 Ga, which can be explained as being the weighted average of the unresolved peaks of different intensity (7.4, 9.4, 10.5 Ga) reported by Rocha-Pinto et al. (29).

In Fig S5b we show stellar lifetimes of proposed parent stars in support for our hypothesis discussed in the main text. We hypothesize and make the case here that the ~7 Ga peak produced stars of masses abundant enough and short-lived enough to become dust-producing between 4.6 and 4.9 Ga ago, <300 Ma before the start of the Solar System. Different workers use different parameter values for determining stellar lifetimes, see discussion in Romano et al. (31), Rocha-Pinto et al. (29), Kippenhahn et al. (32), Ryan & Norton (33). The choice of the power law index is particularly sensitive for low-mass stars <1 $M_\odot$ but not so much for the mass range of the presolar grains' parent stars. To take these different approaches into account we have calculated stellar main sequence lifetimes (in Ga) with selected different power laws for solar metallicity stars. Stars with metallicities close to solar are likely sources of mainstream SiC grains (e.g., Heck et al. (34)).

After Matthews et al. (35), for $M/M_\odot < 1.6\ M_\odot$,

$$\tau = \frac{14.8067}{m^{3.8672}}$$

and for $1.6 < M/M_\odot < 3.0$,

$$\tau = \frac{9.8737}{m^{3.1037}}$$

after Padovani & Matteucci (36) for $M/M_\odot < 6.6\ M_\odot$,

$$\tau = (10^{\left[1.338-\sqrt{1.79-0.2232 \times (7.764 - \log m)}\right]/0.1116} - 9) \times 10^{-9}$$

after Maeder & Meynet (37) for $M/M_\odot \geq 1.3\ M_\odot$,

$$\tau = 10^{-3.7 \times \log(m)+10.35} \times 10^{-9}$$

and after Kippenhahn et al. (32),

$$\tau = \frac{9}{m^{2.5}}$$

Figure S5b shows as a grey shaded area Δt the 300 Ma presolar time interval when the ~60% of the analyzed SiC grains, the young grains with $T_{21} < 300$ Ma, formed, assuming that the grains' parent stars formed in the ~7 Ga enhanced SFR peak. Where the Δt intersects the lifetime curves we can read off the stellar masses of the grains putative parent stars that formed in the ~7 Ga SFR peak. Depending on the lifetime estimate used we find stellar masses ranging from ~1.3 $M_\odot$ to ~1.9 $M_\odot$, a mass range that yields abundant stars (31). However, we cut the mass range below 1.5 $M_\odot$ as these stars lose their envelope by stellar winds before SiC can form (38). This makes the Padovani & Matteucci lifetime curve shown in Fig S5b not viable for our hypothesis. Based on our

data and our assessment, the hypothesis is plausible that the 60% of the analyzed SiC grains condensed from stars in the ~1.6 $M_\odot$ to ~1.9 $M_\odot$ mass range, which formed in a ~7 Ga moderately enhanced SFR peak. However, the hypothesis' robustness needs to be tested with more age data and sophisticated modelling such as presented by Zhukovska et al. (38, 39) which is beyond the scope of this work.

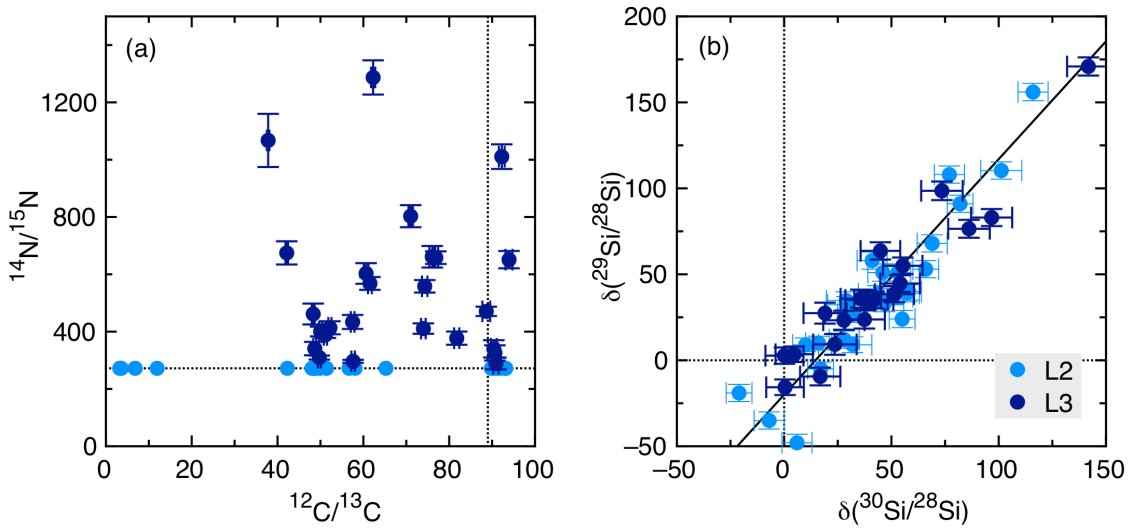

Figure S1. Classification of presolar SiC grains. (a) Carbon and nitrogen isotopes. Nitrogen isotopes were not analyzed for grains on the L2 mount. Compositions are consistent with mainstream SiC except for three grains: $^{12}C/^{13}C$ ratios for three grains are low classifying them as AB type SiC grains. (b) Silicon isotopes. Mainstream line ($\delta^{29}Si=1.37\times\delta^{30}Si-20$, in ‰). Silicon isotopes of the samples are consistent with mainstream SiC. L2 data were reported in Heck et al. (6). All figures: analytical uncertainties are shown as 1σ error bars if larger than the symbol.

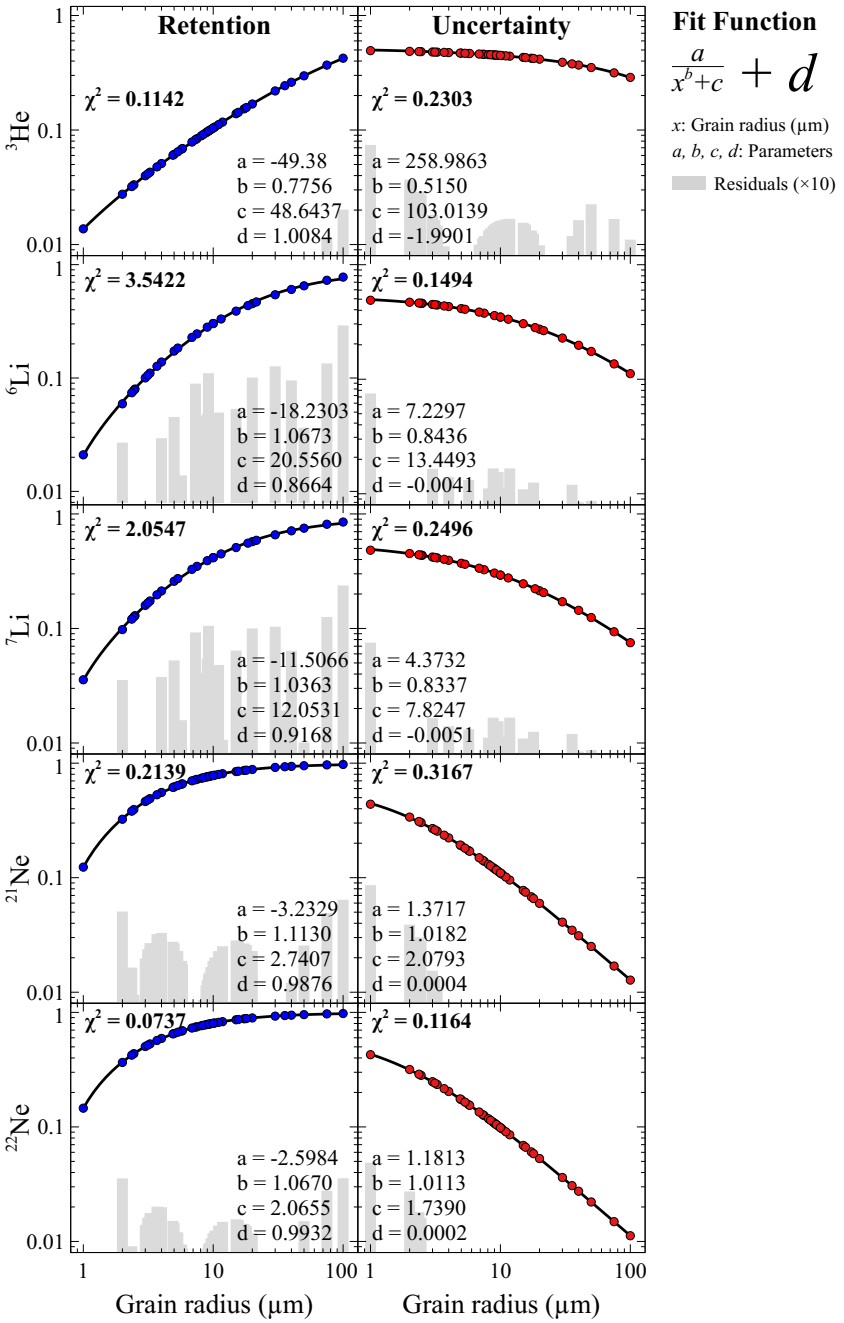

Fig. S2. Retention of cosmogenic He, Li, and Ne isotopes. All modeled values and the associated uncertainties were fit using the best-fit function shown in order to present a simple method for calculating production rates in presolar grains with different sizes. The gray bars show the residuals multiplied by ten, which were calculated for each modeled point by comparing the data point and the calculated value using the fit. The low residuals show that this unphysical fitting describes the calculated retentions and associated uncertainties well and can be used for future cosmogenic presolar grain studies for presolar SiC grains with radii between 1 and 100 μm.

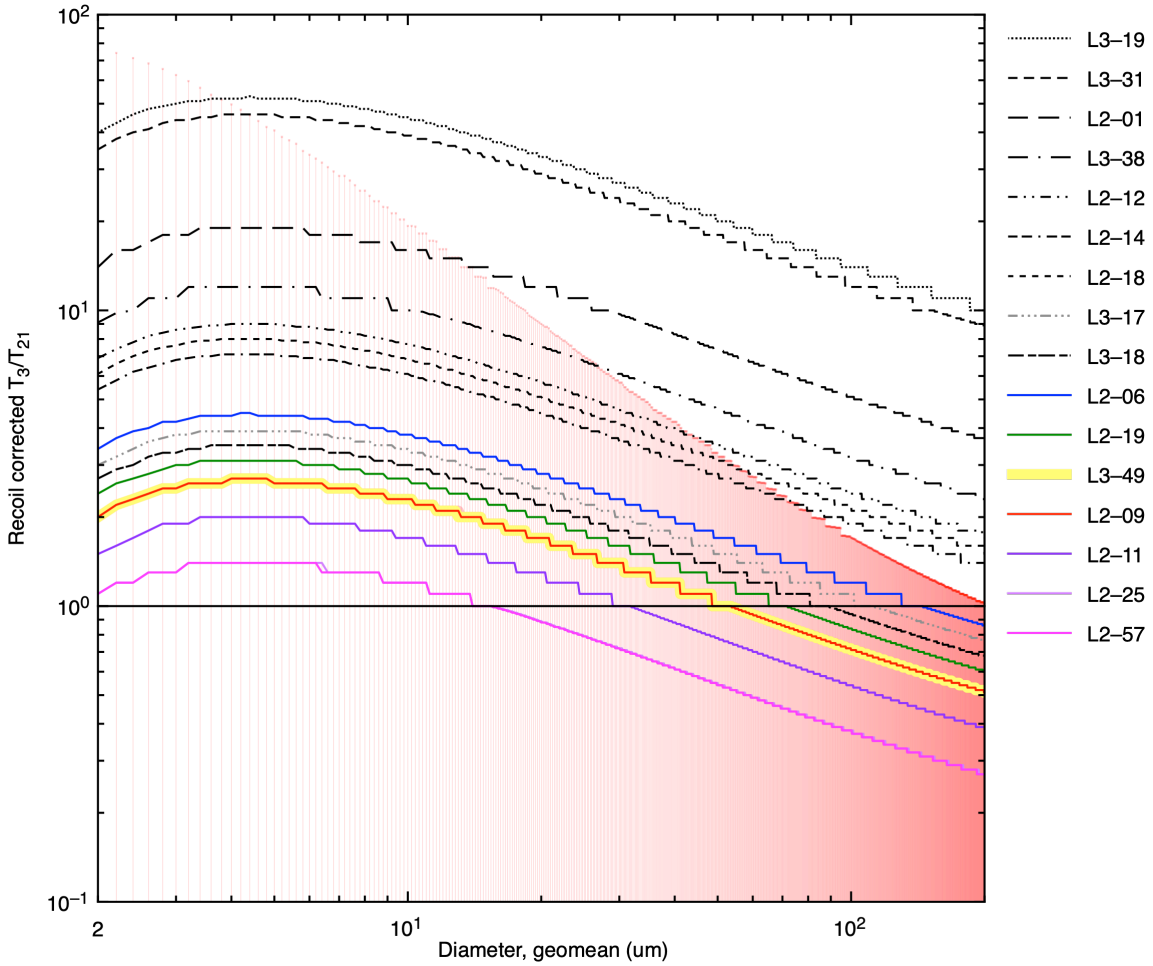

Fig. S3. Ratios of nominal recoil corrected ^{3}He and ^{21}Ne exposure ages, T_3/T_{21}, as functions of grain size. The ratios are shown as curves with different color and line style. The estimated diameter of the irradiated object (aggregate or grain) containing the analyzed grain is given by the intersection of the curves with the horizontal line at 1, where $T_3=T_{21}$. The error bars for L2-09 are representative of the other grains' T_3/T_{21} ratios and are shown as red vertical bars that appear as a red shaded area where the spacing between datapoints appears narrow.

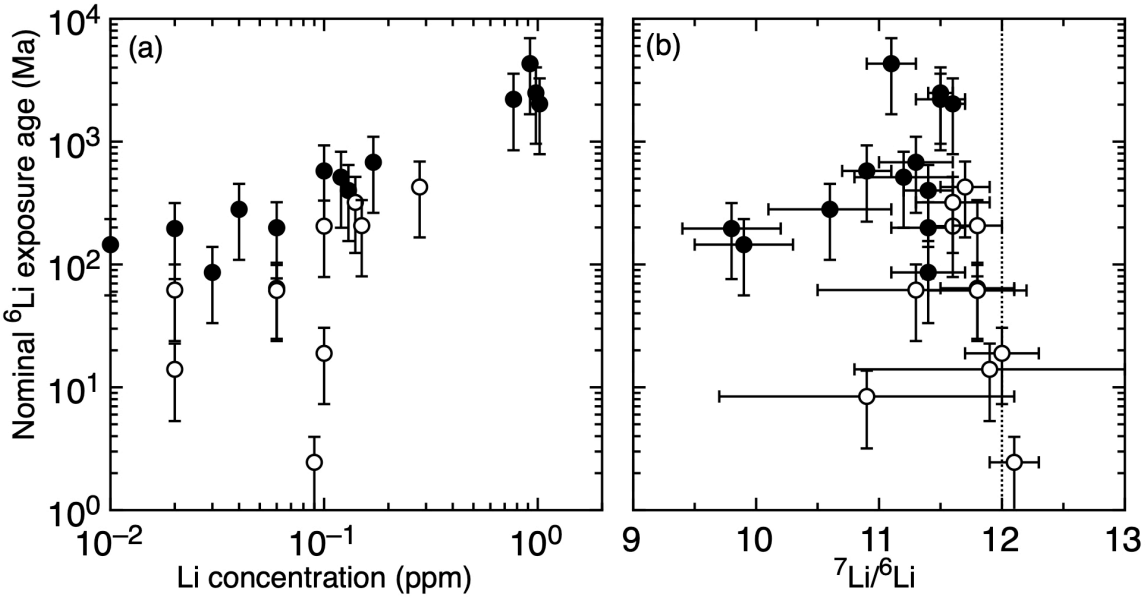

Figure S4. Li isotopes. (a) The estimated Li concentrations correlate with the nominal ^{6}Li exposure ages (not corrected for nuclear recoil loss), something that is not observed for Ne. (b) However, the nominal ^{6}Li exposure ages do not anti-correlate with the ^{7}Li/^{6}Li ratios. One would expect grains with longer cosmic ray exposures to be closer to the cosmogenic Li endmember composition at a ^{7}Li/^{6}Li ratio of 1.2 and grains with shorter exposure ages closer to the solar/terrestrial Li endmember composition (dotted line ~12), something that is not observed here but observed for neon. This observation suggests significant and variable Li contamination of unknown origin to be the reason for the correlation in (a). Closed and open symbols have δ^6Li $\geq 2\sigma$ and δ^6Li $< 2\sigma$ below solar/terrestrial endmember, respectively.

(a)

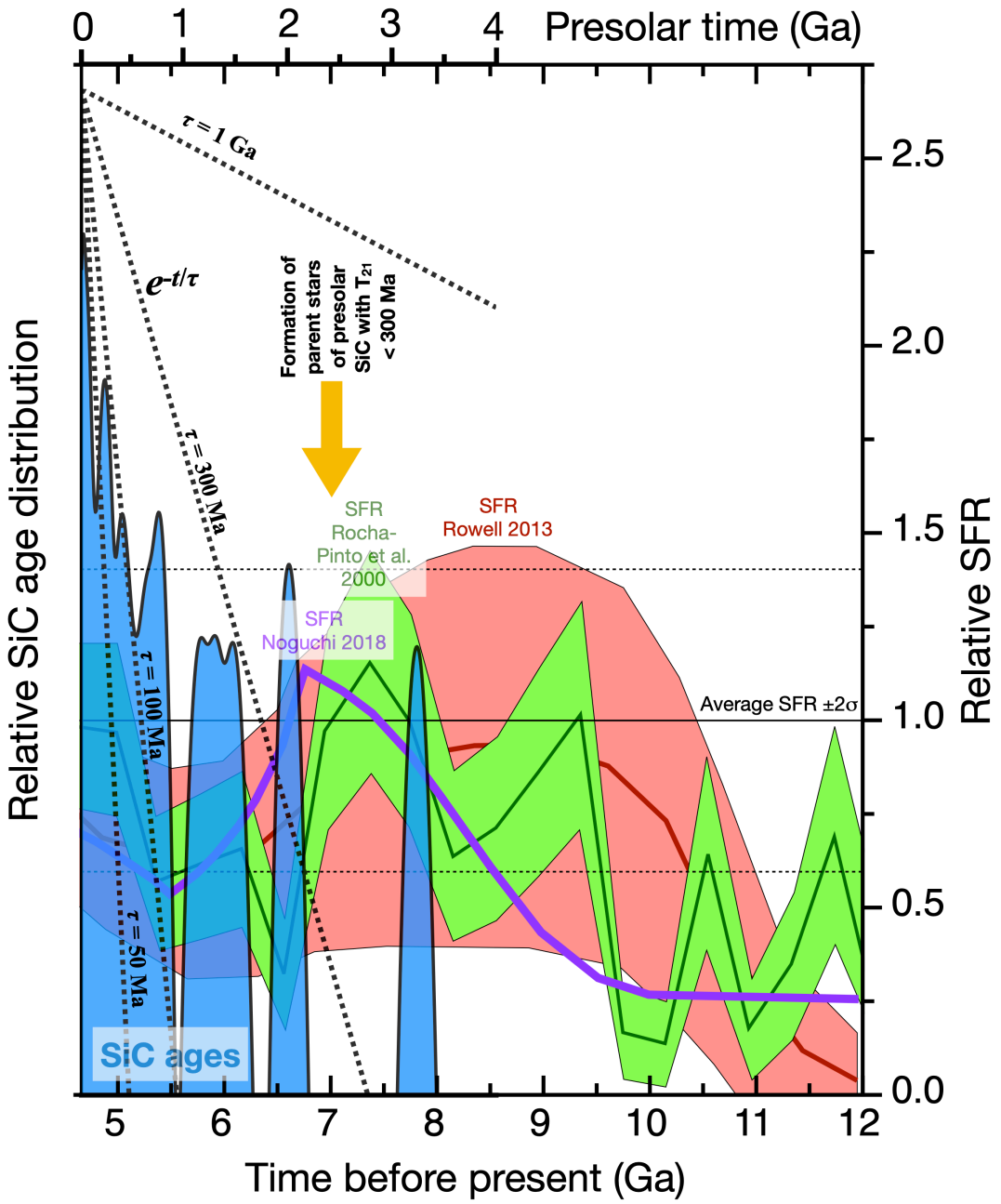

Figure S5. (a) The ^{21}Ne-exposure age distribution of presolar SiC grains, shown as the Kernel Density Estimation (27) (blue). Steady-state model lifetimes $e^{-t/\tau}$ are shown in Fig. S5a as dotted lines with average model lifetimes of τ=50, 100, 300 and 1000 Ma. The dark purple line shows the star formation rate (SFR) curve reported by Noguchi (28), the green and red lines represent the SFR curves given by Rocha-Pinto et al. (29) and Rowell (30), respectively, with the uncertainty envelopes of the latter two curves shown by light green and light red shaded areas. We also show an average SFR as a solid horizontal line with its ±2σ as dashed lines. The yellow arrow points to the hypothesized time of formation of parent stars of the SiC grains with T_{21} < 300 Ma in the ~7 Ga SFR peak.

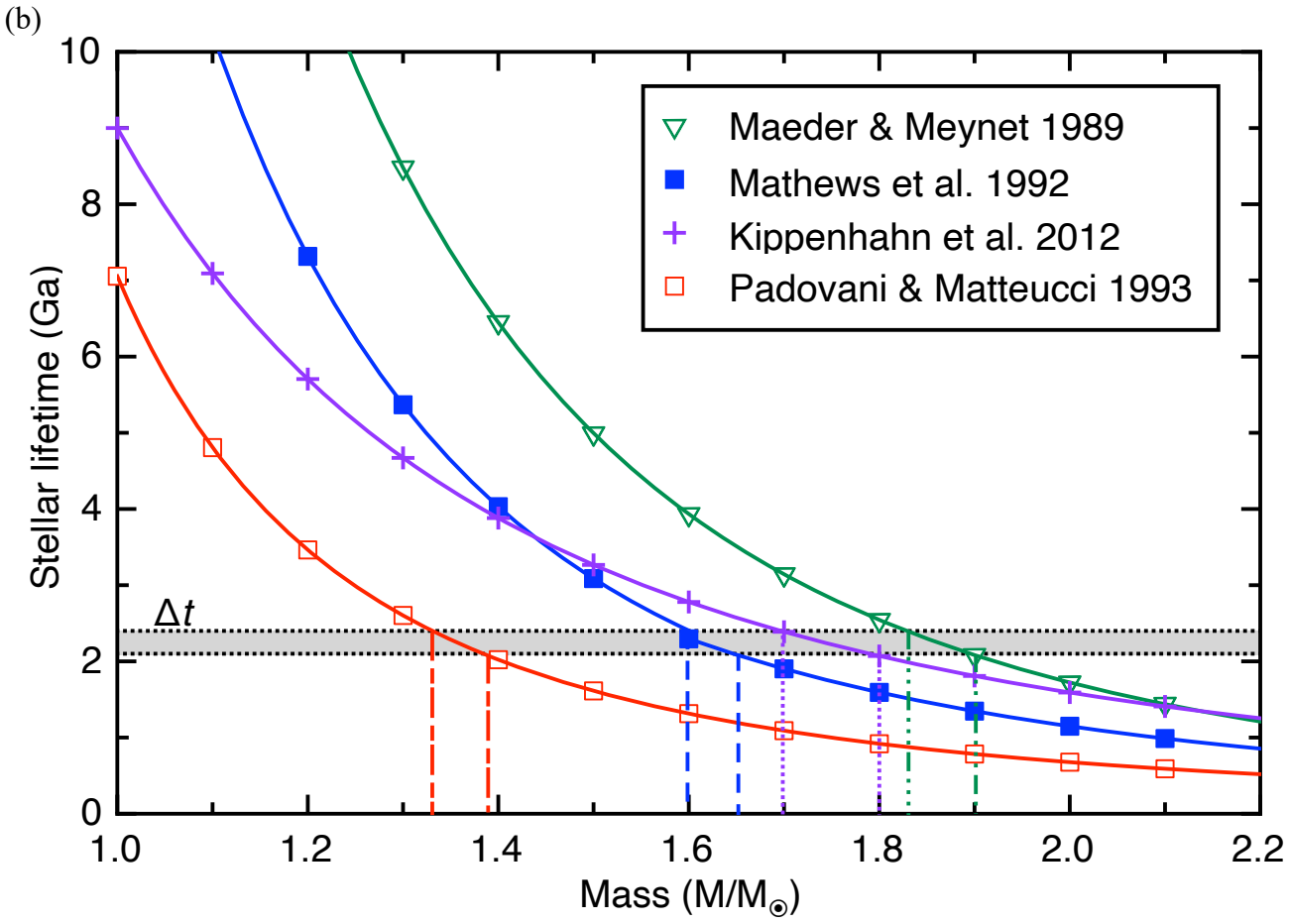

Figure S5. (b) Calculated stellar main sequence lifetimes with different power law indices (see supplementary text). The zero age on the ordinate represents star formation ~7 Ga ago. Stars become dust producing in the AGB and post-AGB star phase after the main sequence lifetime. To explain dust formation between 4.6 and 4.9 Ga ago the parent stars need to have main sequence lifetimes between ~2.1 Ga to ~2.4 Ga (~7 Ga – 4.9 Ga and ~7 Ga – 4.6 Ga, respectively). The figure shows as a grey shaded area Δt the 300 Ma presolar time interval when 60% of the analyzed SiC grains formed. Where the Δt intersects the lifetime curves we can read off the stellar masses of the grains parent stars.

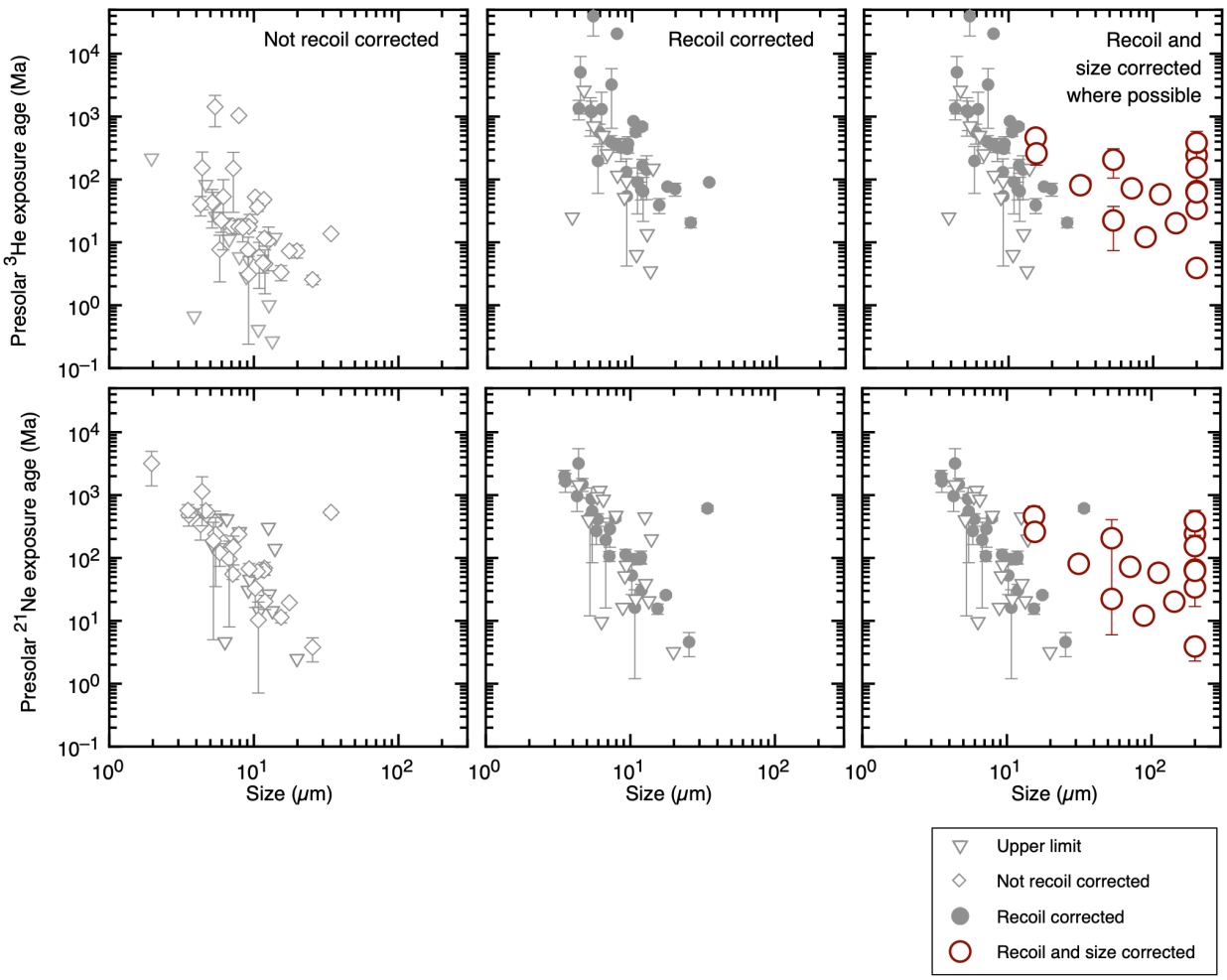

Figure S6. Size-age diagrams. Size is given as the geometric mean of the diameter of the grains. Size-corrected data are for aggregates during irradiation in the ISM. Aggregates >200 µm are shown at 200 µm as our recoil correction is limited to this grain size. See main text for explanation.

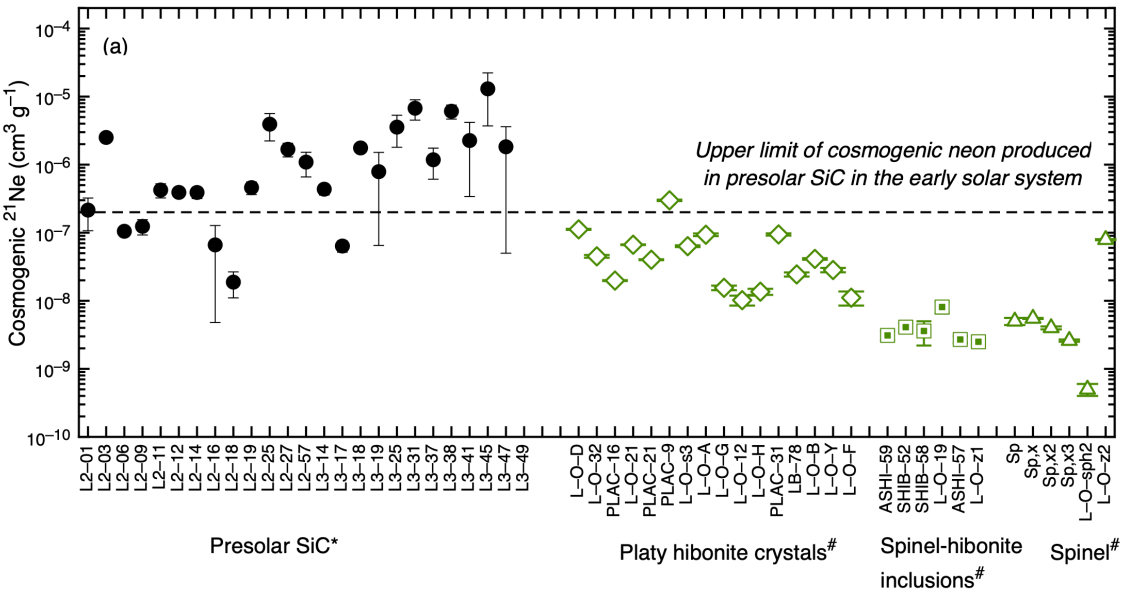

Figure S7. Early solar system cosmogenic neon. Comparison of determined cosmogenic ^{21}Ne concentrations for large presolar SiC from Murchison (*this study) with early solar system condensates from $^{\#}$Kööp et al. (15): platy hibonite crystals (PLACs); spinel-hibonite inclusions (SHIBs) and spinels. The production rate ratios of cosmogenic ^{21}Ne $P_{21\_SiC}/P_{21\_Hibonite}$ is about 0.7. Therefore, the dashed line is slightly below the data point of the highest cosmogenic ^{21}Ne concentration in a platy hibonite crystal.

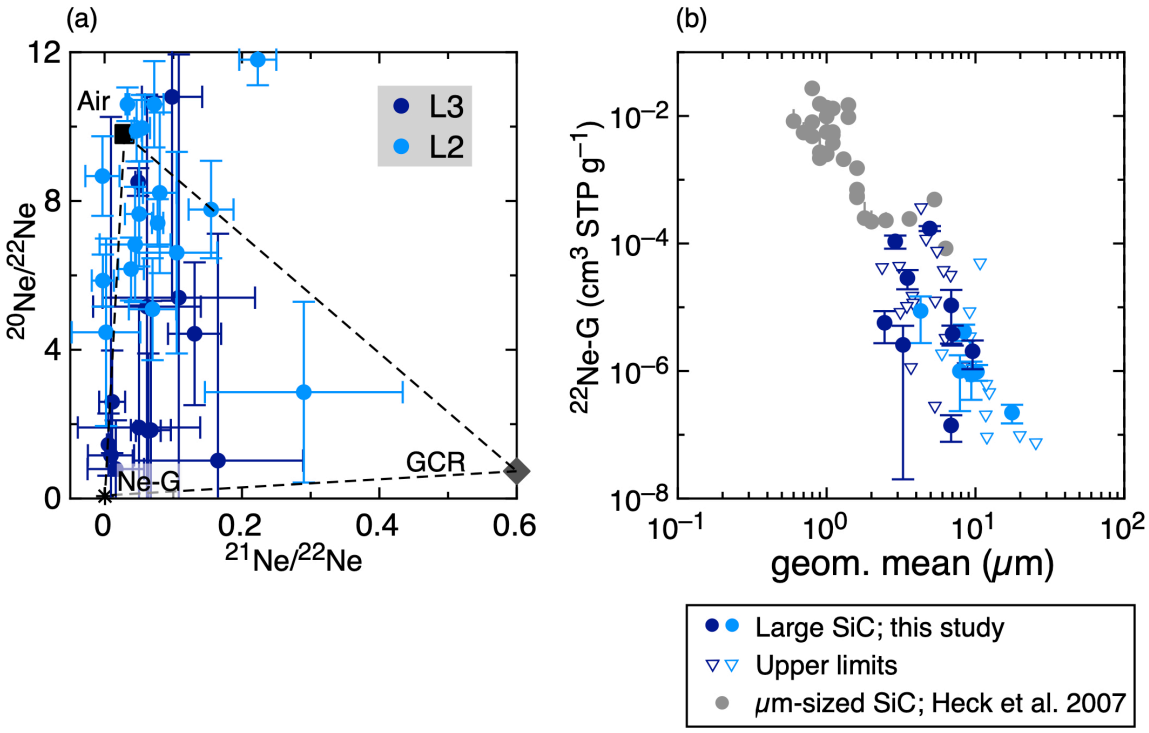

Figure S8. Neon components. (a) Neon three-isotope diagram. Distribution of presolar SiC neon data with the three main neon components: terrestrial atmospheric ("Air"), cosmogenic ("GCR") and AGB star He-shell ("Ne-G). (b) Nucleosynthetic neon. Neon produced by α-capture in the He-shell of AGB stars (Ne-G) is predominantly ^{22}Ne and gets implanted by the hot stellar wind into circumstellar SiC grains. This results in a surface-correlated concentration effect, leading larger grains to have smaller overall concentrations (6). This trend is observed for SiC grains of different sizes from Murchison and Murray meteorites that were analyzed in different analytical sessions.

Table S1. Helium and neon isotopes and components. Concentrations at Standard Temperature and Pressure (STP). Size is the geometric mean of the diameter before noble gas analysis.

ID	Size (µm)	^{3}He (10^{-8} cm^3/g)	^{4}He (10^{-3} cm^3/g)	^{20}Ne (10^{-6} cm^3/g)	^{21}Ne (10^{-6} cm^3/g)	^{22}Ne (10^{-6} cm^3/g)	^{21}Ne$_{cos}$ (10^{-6} cm^3/g)	^{22}Ne-G (10^{-6} cm^3/g)
L3-01	9.6	< 3.19	903 ± 229	< 4.62	< 0.13	2.26 ± 1.01	< 0.109	2.04 ± 0.97
L3-03	6.8	33.2 ± 22.1	1786 ± 609	< 11.6	0.515 ± 0.193	< 2.79	0.483 ± 0.184	< 32.0
L3-05	2.4	169 ± 145		42.9 ± 38.2		< 55.6	< 2.01	< 42.2
L3-06	3.3	< 17.0		< 30.0	< 0.125	2.92 ± 0.84	< 0.100	2.57 ± 2.55
L3-13	5.3	< 9.05	< 0.350	1.62 ± 1.26		0.315 ± 0.247	< 0.0300	< 0.283
L3-14	2.4	24.3 ± 16.8	1.952 ± 1.638	< 41.9	0.535 ± 0.195	7.95 ± 1.85	0.492 ± 0.194	5.71 ± 2.98
L3-17	3.1	58.2 ± 14.8	0.000582 ± 0.000148	3.09 ± 2.19	0.234 ± 0.041	< 0.70	0.226 ± 0.040	< 8.36
L3-18	6.9	10.6 ± 2.86	0.389 ± 0.190	1.73 ± 0.64	0.0514 ± ###	0.391 ± 0.090	0.0464 ± 0.0087	0.140 ± 0.063
L3-19	7.0	3302 ± 60	1339987 ± 4946	345 ± 11	1.98 ± 0.15	40.5 ± 1.2	0.961 ± 0.095	3.83 ± 1.32
L3-20	8.3	< 37.7	< 502	40.5 ± 10.8	< 0.224	2.56 ± 0.81	< 0.224	< 1.18
L3-21	3.7	18.8 ± 12.9	< 0.348	13.1 ± 5.5	< 0.058	0.760 ± 0.431	< 0.0579	< 1.14
L3-24	6.9	< 18.6			< 0.441	6.30 ± 1.34	< 0.441	10.7 ± 8.0
L3-25	6.3	< 35.6	< 37.9	< 48.3	0.461 ± 0.411	4.25 ± 2.15	0.394 ± 0.361	< 3.28
L3-30	4.7		< 1133	< 75.2	< 1.65	13.2 ± 10.8	< 1.21	< 118
L3-31	5.5	4543 ± 2351	163809 ± 1258	< 30.6	1.44 ± 0.60	< 4.02	1.36 ± 0.57	< 76.3
L3-36	3.1	< 2.13	< 9356	< 413		19.8 ± 16.4		< 44.2
L3-37	3.8		< 5015		1.63 ± 0.41		1.63 ± 0.41	< 15.0
L3-38	6.9	476 ± 380	< 990	< 26.7	0.621 ± 0.293	3.76 ± 2.18	0.611 ± 0.296	< 10.4
L3-41	3.5	< 263	5234 ± 3855	< 153	2.51 ± 0.53	39.5 ± 7.5	2.30 ± 0.54	28.7 ± 9.6
L3-45	3.8	< 82.2	12014 ± 1225	124 ± 56	1.32 ± 1.06		0.969 ± 0.822	< 11.7
L3-46	2.9	486 ± 380		383 ± 192	< 4.38	147 ± 25	< 2.12	108 ± 25

ID	Size (µm)	^{3}He (10^{-8} cm^3/g)	^{4}He (10^{-3} cm^3/g)	^{20}Ne (10^{-6} cm^3/g)	^{21}Ne (10^{-6} cm^3/g)	^{22}Ne (10^{-6} cm^3/g)	^{21}Ne$_{cos}$ (10^{-6} cm^3/g)	^{22}Ne-G (10^{-6} cm^3/g)
L3-47	4.3		< 11780	570 ± 124	6.31 ± 4.31	15.6 ± 10.4	4.65 ± 3.33	< 367
L3-48	6.1		< 181		0.522 ± 0.360	1.66 ± 0.80	0.522 ± 0.360	< 24.8
L3-49	5.2	133 ± 65		< 15.2	0.669 ± 0.474	< 1.51	0.669 ± 0.474	< 25521
L3-50	3.5		5547 ± 4948	379 ± 117	3.44 ± 0.67	35.1 ± 14.1	2.33 ± 0.55	< 10.4
L3-52	5.4	< 66.2		< 127		6.28 ± 2.71		< 12.6
L3-59	4.9	137 ± 83	247292 ± 3274	290 ± 168	1.13 ± 0.45	200 ± 4	< 0.678	172 ± 15
L2-01	10.2	167 ± 9	2.09 ± 0.03	12.5 ± 3.1	0.171 ± 0.083	2.45 ± 0.24	0.134 ± 0.068	0.972 ± 0.270
L2-02	12.4		0.0364 ± 0.0128	5.81 ± 2.06	< #####	0.52 ± 0.19	< 0.0108	< 0.461
L2-03	34.1	43.5 ± 1.8	0.383 ± 0.060	135 ± 4	2.56 ± 0.28	11.5 ± 0.6	2.17 ± 0.24	
L2-04	13.4	< 0.85	0.206 ± 0.012	146 ± 3	0.458 ± 0.035	13.8 ± 0.5	< 0.0587	
L2-05	9.1	23.6 ± 14.7	0.103 ± 0.036	30.4 ± 6.1		< 2.59		< 8.55
L2-06	17.6	23.1 ± 1.6	0.038 ± 0.003	10.6 ± 0.4	0.110 ± 0.008	1.43 ± 0.11	0.0793 ± 0.0060	0.223 ± 0.072
L2-07	9.2	9.82 ± 9.05	0.140 ± 0.034	12.2 ± 2.1	< 0.143	2.74 ± 1.46	< 9.27	< 3.46
L2-08	19.9	23.2 ± 5.4	0.026 ± 0.003	2.35 ± 0.13	< #####	0.132 ± 0.077	< 0.0102	< 0.098
L2-09	11.9	14.4 ± 9.6	0.067 ± 0.018	32.5 ± 1.4	0.178 ± #####	3.26 ± 0.25	0.0828 ± 0.0209	< 0.0925
L2-10	9.4	68.0 ± 19.9	0.163 ± 0.018	22.5 ± 2.3	< 0.314	3.30 ± 0.67	< 0.186	0.879 ± 0.526
L2-11	11.8	36.9 ± 9.2	0.133 ± 0.017	2.85 ± 2.07	0.289 ± 0.068	1.00 ± 0.44	0.281 ± 0.066	< 0.621
L2-12	11.7	152 ± 16	0.117 ± 0.010	15.2 ± 0.9	0.302 ± 0.042	1.95 ± 0.31	0.258 ± 0.037	< 0.206
L2-13	7.9	56.2 ± 13.4	0.223 ± 0.048	53.3 ± 5.3	< 0.134	6.14 ± 0.45	< 30.8	1.00 ± 0.76
L2-14	10.6	115 ± 17	8.90 ± 0.02	63.7 ± 3.4	0.435 ± 0.070	6.02 ± 0.57	0.247 ± 0.046	
L2-15	8.4	53.7 ± 21.4	0.0775 ± 0.0490	55.4 ± 5.3	< 0.128	9.46 ± 0.67	< 21.0	4.15 ± 1.18
L2-16	10.7	< 1.30	0.0498 ± 0.0077	14.4 ± 2.4	0.0839 ± #####	< 0.187	0.0422 ± 0.0391	< 49.9

ID	Size (µm)	^{3}He (10^{-8} cm^3/g)	^{4}He (10^{-3} cm^3/g)	^{20}Ne (10^{-6} cm^3/g)	^{21}Ne (10^{-6} cm^3/g)	^{22}Ne (10^{-6} cm^3/g)	^{21}Ne$_{cos}$ (10^{-6} cm^3/g)	^{22}Ne-G (10^{-6} cm^3/g)
L2-17	11.6	15.0 ± 4.7	0.0432 ± 0.0071	6.08 ± 3.11		0.270 ± 0.210		
L2-18	25.4	8.11 ± 1.40	0.0778 ± 0.0016	1.20 ± 0.14	0.0190 ± ###	0.181 ± 0.071	0.0155 ± 0.0064	< 0.0755
L2-19	9.3	56.0 ± 7.7	0.101 ± 0.024	40.2 ± 4.8	0.392 ± 0.077	4.89 ± 1.14	0.274 ± 0.058	< 1.22
L2-25	4.3	127 ± 44	0.924 ± 0.237	381 ± 19	2.50 ± 0.93	49.8 ± 8.8	1.38 ± 0.59	8.76 ± 6.02
L2-27	2.0	< 692	10.5 ± 2.8	3951 ± 342	24.7 ± 11.6	641 ± 68	13.0 ± 7.3	
L2-57	6.0	70.5 ± 24.6	0.613 ± 0.105	436 ± 19	2.06 ± 0.29	44.1 ± 3.2	0.771 ± 0.175	< 1.87

Table S2. C, N, and Si isotopes. Isotopic data analyzed with NanoSIMS.

Lab Code	$^{12}C/^{13}C$			$^{14}N/^{15}N$			$\delta^{29}Si/^{28}Si$ (‰)			$\delta^{30}Si/^{28}Si$ (‰)		
L3-01	57.5	±	0.4	433.8	±	24.4	98.6	±	5.4	73.5	±	9.7
L3-03	48.3	±	0.3	461.5	±	36.4	38.4	±	4.7	51.4	±	9.1
L3-05	84.2	±	0.6		±		9.0	±	4.6	31.9	±	9.0
L3-06	61.5	±	0.5	568.2	±	22.4	34.8	±	5.0	28.9	±	9.2
L3-13	48.7	±	0.3	340.8	±	23.3	32.9	±	4.7	46.6	±	9.1
L3-14	81.8	±	0.6	377.3	±	23.0	37.0	±	4.8	50.8	±	9.2
L3-17	52.2	±	0.4	413.5	±	22.7	110.3	±	5.0	101.2	±	9.6
L3-18	49.7	±	0.3	309.5	±	7.0	38.7	±	4.7	43.7	±	9.1
L3-19	57.6	±	0.4	296.5	±	5.2	63.6	±	5.0	44.9	±	9.2
L3-20	90.9	±	0.6	288.7	±	20.7	3.5	±	4.5	4.7	±	8.7
L3-21	50.0	±	0.4	400.4	±	17.0	32.3	±	4.8	29.3	±	9.1
L3-24	90.4	±	0.7	339.9	±	30.2	-15.7	±	4.5	0.4	±	8.7
L3-25	71.0	±	0.5	802.8	±	38.5	35.0	±	4.8	41.8	±	9.1
L3-30	92.3	±	0.7	1010.6	±	42.9	83.0	±	5.0	96.7	±	9.6
L3-31	42.1	±	0.3	674.8	±	40.5	170.9	±	5.3	141.8	±	9.9
L3-36	76.9	±	0.6	658.1	±	22.0	55.0	±	4.8	55.3	±	9.2
L3-37	51.2	±	0.4	388.6	±	10.6	76.5	±	5.2	86.1	±	9.7
L3-38	62.3	±	0.5	1287.0	±	59.7	35.9	±	5.2	35.7	±	9.4
L3-41	74.0	±	0.5	410.7	±	18.2	44.6	±	4.8	54.0	±	9.2
L3-45	37.8	±	0.3	1067.2	±	92.8	23.7	±	5.3	37.4	±	9.5
L3-46	88.6	±	0.9	470.8	±	16.3	9.3	±	6.1	23.7	±	10.1
L3-47												
L3-48	90.6	±	0.7	325.7	±	26.6	2.7	±	4.8	0.1	±	8.9
L3-49	74.3	±	0.6	558.2	±	21.8	23.3	±	5.5	27.9	±	9.6

Lab Code	$^{12}C/^{13}C$			$^{14}N/^{15}N$			$\delta^{29}Si/^{28}Si$ (‰)			$\delta^{30}Si/^{28}Si$ (‰)		
L3-50	93.9	±	0.8	651.2	±	30.2	-9.4	±	5.2	16.8	±	9.4
L3-52	76.0	±	0.7	661.3	±	37.7	35.1	±	5.7	38.4	±	9.8
L3-59	60.6	±	0.5	603.0	±	36.0	27.4	±	6.1	19.0	±	10.0
L2-01	42.3	±	0.2				156.0	±	5.0	116.0	±	7.0
L2-02	93.2	±	0.6				-14.0	±	5.0	-10.0	±	6.0
L2-03	48.5	±	0.2				39.0	±	5.0	57.0	±	6.0
L2-04	91.1	±	0.5				-5.0	±	4.0	17.0	±	6.0
L2-05	92.1	±	0.5				-24.0	±	5.0	-11.0	±	6.0
L2-06	51.4	±	0.2				91.0	±	5.0	82.0	±	6.0
L2-07	90.3	±	0.5				9.0	±	4.0	10.0	±	6.0
L2-08	48.7	±	0.2				24.0	±	5.0	55.0	±	6.0
L2-09	48.3	±	0.2				40.0	±	5.0	58.0	±	6.0
L2-10	58.1	±	0.3				-48.0	±	5.0	6.0	±	7.0
L2-11	56.7	±	0.3				108.0	±	5.0	77.0	±	7.0
L2-12	3.6	±	0.0				-35.0	±	5.0	-7.0	±	7.0
L2-13	65.3	±	0.4				27.0	±	5.0	32.0	±	7.0
L2-14	48.9	±	0.3				12.0	±	5.0	28.0	±	7.0
L2-15	48.0	±	0.2				53.0	±	5.0	66.0	±	6.0
L2-16	93.0	±	0.6				-19.0	±	5.0	-21.0	±	6.0
L2-17	89.8	±	0.4				10.0	±	4.0	16.0	±	6.0
L2-18	48.3	±	0.2				51.0	±	5.0	53.0	±	6.0
L2-19	49.9	±	0.3				68.0	±	5.0	69.0	±	7.0
L2-25	11.9	±	0.1				51.0	±	5.0	46.0	±	7.0
L2-27	6.8	±	0.0				38.0	±	5.0	50.0	±	7.0
L2-57	3.2	±	0.0				58.0	±	5.0	41.0	±	7.0

Table S3. Nuclear recoil correction (retention) and presolar ^{3}He (T_3) and ^{21}Ne (T_{21}) cosmic ray exposure ages in Ma.
[1]Geometric mean diameter before noble gas analysis. [2]Geometric mean diameter of grain before pressing into gold substrate.
[3]Estimated mean diameter of object in ISM. [4]As determined for initial estimated size if applicable. N.a.=not available.

ID	Analyzed size[1] (µm)	Pre-press size[2] (µm)	Estimated initial size[3] (µm)	Morphology	^{3}He retention[4]	T_3 not recoil corrected	T_3 recoil corrected[3]	^{21}Ne retention[4]	T_{21} not recoil corrected	T_{21} recoil corrected[3]
L3-01	9.6	12.7	–	Euhedral	7%	≤ 1.0	≤ 17	68%	≤ 27	≤ 44
L3-03	6.8	12.6	–	Euhedral	7%	10 ± 7	236 ± 157	68%	118 ± 45	236 ± 90
L3-05	2.4	6.2	–	Euhedral	4%	53 ± 46	3259 ± 2798	47%	≤ 492	≤ 2934
L3-06	3.3	9.2	–	Euhedral	6%	≤ 5.4	≤ 235	59%	≤ 24.5	≤ 93
L3-13	5.3	8.9	–	Euhedral	6%	≤ 2.9	≤ 79	58%	≤ 7.35	≤ 17
L3-14	2.4	5.8	–	Euhedral	4%	7.7 ± 5.3	449 ± 311	45%	121 ± 47	677 ± 266
L3-17	3.1	7.1	112	Euhedral	32%	18.3 ± 4.7	58 ± 15	95%	55 ± 10	58 ± 10
L3-18	6.9	15.4	89	Fragment	28%	3.3 ± 0.9	12 ± 3	94%	11 ± 2	12 ± 2
L3-19	7.0	7.9	>200	Euhedral	>42%	1042 ± 19	243 ± 4	>97%	236 ± 23	243 ± 24
L3-20	8.3	14.0	–	Fragment	8%	≤ 12	≤ 226	71%	≤ 55	≤ 97
L3-21	3.7	10.9	–	Fragment	7%	5.9 ± 4.1	230 ± 158	64%	≤ 14	≤ 47
L3-24	6.9	7.9	–	Fragment	5%	≤ 5.9	≤ 131	55%	≤ 108	≤ 214
L3-25	6.3	6.7	–	Euhedral	4%	≤ 11	≤ 271	50%	96 ± 89	203 ± 186
L3-30	4.7	5.9	–	Euhedral	4%			46%	≤ 296	≤ 783
L3-31	5.5	5.4	>200	Euhedral	>42%	1433 ± 742	383 ± 198	>97%	333 ± 140	383 ± 189
L3-36	3.1	3.9	–	Euhedral	3%	≤ 0.67	≤ 31	32%	≤ 372	≤ 1515
L3-37	3.8	3.5	–	Euhedral	2%			29%	400 ± 101	1296 ± 328
L3-38	6.9	7.2	>200	Euhedral	>42%	150 ± 120	154 ± 123	>97%	150 ± 73	154 ± 75
L3-41	3.5	4.7	–	Euhedral	3%	≤ 83	≤ 3408	38%	564 ± 131	1980 ± 462

ID	Analyzed size[1] (µm)	Pre-press size[2] (µm)	Estimated initial size[3] (µm)	Morphology	^{3}He retention[4]	T_3 not recoil corrected	T_3 recoil corrected[3]	^{21}Ne retention[4]	T_{21} not recoil corrected	T_{21} recoil corrected[3]
L3-45	3.8	5.4	–	Euhedral	4%	≤ 26	≤ 979	43%	237 ± 202	759 ± 645
L3-46	2.9	4.4	–	Euhedral	3%	153 ± 120	7561 ± 5911	36%	≤ 519	≤ 2287
L3-47	4.3	4.4	–	Euhedral	3%			36%	1141 ± 815	3236 ± 2312
L3-48	6.1	6.5	—	Fragment	4%			49%	128 ± 88	274 ± 189
L3-49	5.2	5.3	53	Euhedral	20%	42 ± 21	206 ± 101	91%	164 ± 116	206 ± 200
L3-50	3.5	3.5	–	Euhedral	2%			29%	571 ± 134	2025 ± 477
L3-52	5.4	6.3	–	Euhedral	4%	≤ 21	≤ 576	48%		
L3-59	4.9	5.2	–	Euhedral	3%	43 ± 26	1286 ± 782	41%	≤ 166	≤ 419
L2-01	10.2	n.a.	>200	Euhedral	>42%	53 ± 3	34 ± 2	>97%	32.9 ± 16.6	34 ± 17
L2-02	12.4	n.a.	–	Euhedral	7%			68%		
L2-03	34.1	n.a.	–	Fragment?	15%	14 ± 1	90 ± 4	86%	531 ± 59	615 ± 68
L2-04	13.4	n.a.	–	Fragment	8%	≤ 0.27	≤ 3.5	70%	≤ 14	≤ 21
L2-05	9.1	n.a.	–	Fragment	6%	7.4 ± 4.6	131 ± 81	59%		
L2-06	17.6	n.a.	144	Fragment	36%	7.3 ± 0.5	20 ± 1	96%	19 ± 1	20 ± 2
L2-07	9.2	n.a.	–	Fragment	6%	3.1 ± 2.9	54 ± 50	59%		
L2-08	19.9	n.a.	–	Fragment?	10%	7.3 ± 1.7	71 ± 16	78%	≤ 2.5	≤ 3.2
L2-09	11.9	n.a.	53	Fragment	20%	4.5 ± 3.0	22 ± 15	91%	20 ± 5	22 ± 6
L2-10	9.4	n.a.	–	Euhedral	6%	21 ± 6	370 ± 108	60%	≤ 46	≤ 76
L2-11	11.8	n.a.	31	Euhedral	14%	12 ± 3	81 ± 20	85%	69 ± 16	81 ± 19
L2-12	11.7	n.a.	>200	Euhedral	>42%	48 ± 5	65 ± 7	>97%	63 ± 9	65 ± 9
L2-13	7.9	n.a.	–	Euhedral	5%	18 ± 4	353 ± 84	55%		
L2-14	10.6	n.a.	>200	Fragment?	>42%	36 ± 5	63 ± 9	>97%	61 ± 11	63 ± 12
L2-15	8.4	n.a.	–	Fragment	5%	17 ± 7	321 ± 128	57%		

ID	Analyzed size[1] (µm)	Pre-press size[2] (µm)	Estimated initial size[3] (µm)	Morphology	^{3}He retention[4]	T_3 not recoil corrected	T_3 recoil corrected[3]	^{21}Ne retention[4]	T_{21} not recoil corrected	T_{21} recoil corrected[3]
L2-16	10.7	n.a.	–	Fragment	6%	≤ 0.41	≤ 6.4	64%	10 ± 10	16 ± 15
L2-17	11.6	n.a.	–	Fragment	7%	4.7 ± 1.5	69 ± 22	66%		
L2-18	25.4	n.a.	>200	Fragment	>42%	2.6 ± 0.4	3.9 ± 0.7	>97%	3.8 ± 1.6	3.9 ± 1.6
L2-19	9.3	n.a.	71	Euhedral	24%	18 ± 2	72 ± 10	93%	67 ± 14	72 ± 15
L2-25	4.3	n.a.	15	Euhedral?	9%	40 ± 14	463 ± 159	73%	338 ± 146	463 ± 200
L2-27	2.0	n.a.	–	Euhedral	1%	≤ 218		12%	3178 ± 1781	
L2-57	6.0	n.a.	16	Euhedral	9%	22 ± 8	260 ± 91	73%	189 ± 43	260 ± 59

Table S4. Li data. Data from grains with multiple spots are displayed sequentially in the same background color. *The Li age T_6 is the nominal exposure age based on cosmogenic Li and is not recoil corrected. δ^6Li is the excess of ^{6}Li relative to meteoritic Li and δ^6Li σ is the relative excess. See supplementary text for more information.

Lab Code	^{7}Li/^{6}Li	1σ err	δ^6Li	1σ err	δ^6Li σ	Li/Si	Li ppm	$^6Li_{cos}$ fraction	^{6}Li/C	^{6}Li/kg of C	T_6 (Ma)	1σ err
L3-05_spot_2	11.1	0.2	84.7	24.3	3.5	5.32E-06	0.92	8.68E-02	4.4E-07	2.20E+19	4.31E+03	2.64E+03
L3-06_spot_2	10.6	0.5	142.6	48.8	2.9	2.07E-07	0.04	1.39E-01	1.8E-08	8.99E+17	2.81E+02	1.72E+02
L3-08_spot_3	11.4	0.3	61.4	24.9	2.5	3.38E-07	0.06	6.43E-02	2.7E-08	1.37E+18	1.99E+02	1.22E+02
L3-08_spot_4	11.6	0.1	35.8	9.9	3.6	5.91E-06	1.02	3.84E-02	4.7E-07	2.34E+19	2.03E+03	1.24E+03
L3-13_spot_1	11.2	0.4	78.4	34.1	2.3	6.84E-07	0.12	8.07E-02	5.6E-08	2.82E+18	5.13E+02	3.14E+02
L3-14_spot_2	11.5	0.2	51.9	19.4	2.7	4.45E-06	0.77	5.48E-02	3.6E-07	1.79E+19	2.21E+03	1.36E+03
L3-17_spot_1	9.9	0.4	214.9	43.7	4.9	7.13E-08	0.01	1.96E-01	6.5E-09	3.27E+17	1.45E+02	8.90E+01
L3-17_spot_2	9.8	0.4	232.4	51.7	4.5	8.91E-08	0.02	2.09E-01	8.3E-09	4.14E+17	1.96E+02	1.20E+02
L3-18_spot_1	11.4	0.3	53.6	27.5	2.0	1.68E-07	0.03	5.65E-02	1.3E-08	6.75E+17	8.61E+01	5.28E+01
L3-19_spot_1	11.4	0.2	53.6	15.4	3.5	7.77E-07	0.13	5.65E-02	6.2E-08	3.13E+18	4.00E+02	2.45E+02
L3-19_spot_2	10.9	0.2	105.2	18.4	5.7	5.75E-07	0.10	1.06E-01	4.8E-08	2.42E+18	5.77E+02	3.54E+02
L3-21_spot_2	11.3	0.3	71.2	23.8	3.0	9.96E-07	0.17	7.38E-02	8.1E-08	4.08E+18	6.79E+02	4.16E+02
L3-47_spot_1	11.5	0.1	45.9	10.1	4.5	5.66E-06	0.98	4.88E-02	4.5E-07	2.27E+19	2.49E+03	1.53E+03

Lab Code	$^{7}Li/^{6}Li$	1σ err	$\delta^{6}Li$	1σ err	$\delta^{6}Li$ σ	Li/Si	Li ppm	$^{6}Li_{cos}$ fraction	$^{6}Li/C$	^{6}Li/kg of C	T_6 (Ma)	1σ err
L3-01_spot_1	11.3	0.8	62.6	71.9	0.9	1.03E-07	0.02	6.54E-02	8.4E-09	4.20E+17	6.19E+01	3.81E+01
L3-01_spot_2	11.9	1.1	13.1	97.3	0.1	1.11E-07	0.02	1.44E-02	8.6E-09	4.32E+17	1.40E+01	8.69E+00
L3-03_spot_1	12.1	0.2	0.5	19.2	0.0	5.05E-07	0.09	5.59E-04	3.9E-08	1.94E+18	2.45E+00	1.50E+00
L3-03_spot_2	11.8	0.3	20.4	24.3	0.8	3.27E-07	0.06	2.22E-02	2.6E-08	1.28E+18	6.40E+01	3.92E+01
L3-04_spot_2	12.7	0.4	-48.4	30.0	1.6	4.52E-07	0.08	-5.65E-02	3.3E-08	1.66E+18	-2.11E+02	1.29E+02
L3-05_spot_1	12.1	0.3	-5.1	25.2	0.2	1.20E-06	0.21	-5.67E-03	9.2E-08	4.60E+18	-5.88E+01	3.61E+01
L3-09_spot_1	11.6	0.2	35.8	21.6	1.7	5.97E-07	0.10	3.84E-02	4.7E-08	2.37E+18	2.05E+02	1.26E+02
L3-10_spot_1	13.0	0.6	-70.6	42.1	1.7	5.94E-08	0.01	-8.43E-02	4.2E-09	2.13E+17	-4.05E+01	2.49E+01
L3-10_spot_2	12.3	0.2	-18.0	19.4	0.9	1.87E-06	0.32	-2.04E-02	1.4E-07	7.06E+18	-3.24E+02	1.99E+02
L3-12_spot_1	11.6	0.3	40.8	23.6	1.7	8.16E-07	0.14	4.36E-02	6.5E-08	3.25E+18	3.20E+02	1.96E+02
L3-12_spot_2	10.9	1.2	108.1	120.6	0.9	8.16E-09	0.00	1.08E-01	6.9E-10	3.44E+16	8.42E+00	5.24E+00
L3-14_spot_1	11.8	0.2	24.2	18.6	1.3	8.88E-07	0.15	2.63E-02	7.0E-08	3.49E+18	2.07E+02	1.27E+02
L3-18_spot_2	11.7	0.2	27.5	16.4	1.7	1.61E-06	0.28	2.98E-02	1.3E-07	6.36E+18	4.27E+02	2.61E+02
L3-21_spot_1	12.0	0.3	3.4	21.2	0.2	5.67E-07	0.10	3.84E-03	4.4E-08	2.19E+18	1.89E+01	1.16E+01
L3-24_spot_1	11.8	0.4	17.7	30.3	0.6	3.59E-07	0.06	1.94E-02	2.8E-08	1.40E+18	6.14E+01	3.76E+01

Table S5. He and Ne blanks and detection limits. Mean blank amounts, detections limits (see text and (2) for definition) and mean, blank-corrected sample amounts with standard errors (SE). Rounded amounts are given in cm^3 at Standard Temperature and Pressure (STP). Taking into account that mean blanks may be slightly different from zero, we define the detection limit to be 2SD of all blanks of a run above the mean blank value. n. m. = not measured.

in cm^3 STP	**^{3}He 10^{-17}**	**^{4}He 10^{-10}**	**^{20}Ne 10^{-15}**	**^{21}Ne 10^{-17}**	**^{22}Ne 10^{-16}**
Mean blanks ± SE; 2SD					
Mount L2 (n=35)	2 ± 2; 8	0.005 ± 0.002; 0.009	1 ± 1; 43	-0.7 ± 2; 8	1 ±3; 11
Mount L3 (n=27)	-9 ± 5; 27	6 ± 4; 23	1 ± 4; 19	4 ± 5; 28	17 ± 4; 20
Detection limits					
Mount L2	19	0.02	10	16	24
Mount L3	44	51	40	59	57

Additional data S1 (appears at the end of this file)

Scanning electron microscope images with size information of the grains.

SI References

1. Amari S, Lewis RS, Anders E (1994) Interstellar grains in meteorites: I. Isolation of SiC, graphite and diamond; size distributions of SiC and graphite. *Geochim Cosmochim Acta* 58:459–470.
2. Heck PR, et al. (2018) Neon isotopes in individual presolar low-density graphite grains from the Orgueil meteorite. *Meteorit Planet Sci* 53:2327–2342.
3. Baur H (1999) A noble-gas mass spectrometer compressor source with two orders of magnitude improvement in sensitivity. *EOS Trans AGU* 46:#F1118.
4. Heck PR, et al. (2007) Presolar He and Ne isotopes in single circumstellar SiC grains. *Astrophys J* 656:1208–1222.
5. Heber VS, et al. (2009) Noble gas composition of the solar wind as collected by the Genesis mission. *Geochim Cosmochim Acta* 73:7414–7432.
6. Heck PR, et al. (2009) Interstellar residence times of presolar SiC dust grains from the Murchison carbonaceous meteorite. *Astrophys J* 698:1158–1164.
7. Trappitsch R, Leya I (2016) Production and recoil loss of cosmogenic nuclides in presolar grains. *Astrophys J* 823:#12 (11 pp).
8. Stone EC, Cummings AC, McDonald FB, Heikkila BC, Webber WR (2013) Voyager 1 observes low-energy galactic cosmic rays in a region depleted of heliospheric ions. *Science* 341:150–153.
9. Ott U, et al. (2009) He and Ne ages of large presolar silicon carbide grains : solving the recoil problem. *Publ Astron Soc Aust* 26:297–302.
10. Gyngard F, Amari S, Zinner E, Ott U (2009) Interstellar exposure ages of large presolar sic grains from the murchison meteorite. *Astrophys J* 700:359–366.
11. Ammon K, Masarik J, Leya I (2008) Noble gases in Grant and Carbo and the influence of S-and P-rich mineral inclusions on the ^{41}K-^{40}K dating system. *Meteorit Planet Sci* 43:685–699.
12. Eberhardt P, Eugster O, Marti K (1965) A redetermination of the isotopic composition of atmospheric neon. *Z Naturforsch A* 20:623–624.
13. Reedy RC (1989) Cosmogenic-nuclide production rates in interstellar grains. *Lunar Planet Sci* 20:888–889.
14. Roth ASG, Baur H, Heber VS, Reusser E, Wieler R (2011) Cosmogenic helium and neon in individual chondrules from Allende and Murchison: Implications for the precompaction exposure history of chondrules. *Meteorit Planet Sci* 46:989–1006.
15. Kööp L, et al. (2018) High early solar activity inferred from helium and neon excesses in the oldest meteorite inclusions. *Nat Astron* 2:709–713.
16. Trappitsch R, Ciesla FJ (2015) Solar cosmic-ray interaction with protoplanetary disks: Production of short-lived radionuclides and amorphization of crystalline material. *Astrophys J* 805:#5 (11 pp).
17. Wieler R (2013) Noble gas mass spectrometry. In: *Meteorites and Cosmochemical*

Processes (Ed. Davis AM), Vol. 1 *Treatise on Geochemistry, 2nd Ed* (Exec. Eds. Holland HD and Turekian KK)*,* Elsevier, Oxford, pp 355–373.
18. Ott U (2014) Planetary and pre-solar noble gases in meteorites. *Geochemistry* 74:519–544.
19. Gallino R, Busso M, Picchio G, Raiteri CM (1990) On the astrophysical interpretation of isotope anomalies in meteoritic SiC grains. *Nature* 348:298–302.
20. Hoppe P, Amari S, Zinner E, Ireland T, Lewis RS (1994) Carbon, nitrogen, magnesium, silicon, and titanium isotopic compositions of single interstellar silicon carbide grains from the Murchison carbonaceous chondrite. *Astrophys J* 430:870–890.
21. Hoppe P, Strebel R, Eberhardt P, Amari S, Lewis RS (1996) Small SiC grains and a nitride grain of circumstellar origin from the Murchison meteorite: Implications for stellar evolution and nucleosynthesis. *Geochim Cosmochim Acta* 60:883–907.
22. Liu N, et al. (2017) J-type carbon stars: A dominant source of ^{14}N-rich presolar SiC grains of type AB. *Astrophys J Lett* 844:#L12 (7 pp).
23. Liu N, Nittler LR, Pignatari M, Alexander CMO, Wang J (2017) Stellar origin of ^{15}N-rich presolar SiC grains of type AB: supernovae with explosive hydrogen burning. *Astrophys J Lett* 842:#L1 (8 pp).
24. Heck PR, et al. (2009) Ne isotopes in individual presolar graphite grains from the Murchison meteorite together with He, C, O, Mg-Al isotopic analyses as tracers of their origins. *Astrophys J* 701:1415–1425.
25. Ott U, et al. (2005) Spallation recoil II: xenon evidence for young SiC grains. *Meteorit Planet Sci* 40:1635–1652.
26. Seitz H-M, et al. (2007) Lithium isotope composition of ordinary and carbonaceous chondrites, and differentiated planetary bodies: bulk solar system and solar reservoirs. *Earth Planet Sci Lett* 260:582–596.
27. Vermeesch P (2012) On the visualisation of detrital age distributions. *Chem Geol* 312–313:190–194.
28. Noguchi M (2018) The formation of solar-neighbourhood stars in two generations separated by 5 billion years. *Nature* 559:585–588.
29. Rocha-Pinto HJ, Scalo J, Maciel WJ, Flynn C (2000) Chemical enrichment and star formation in the Milky Way disk; II. Star formation history. *Astron Astrophys* 358:869–885.
30. Rowell N (2013) The star formation history of the solar neighbourhood from the white dwarf luminosity function. *Mon Not R Astron Soc* 434:1549–1564.
31. Romano D et al. (2005) Quantifying the uncertainties of chemical evolution studies. *Astron Astrophys* 430:491–505.
32. Kippenhahn R, Weigert A, Weiss A (2012) *Stellar Structure and Evolution* (Springer, Berlin, Heidelberg). 2nd Edition, 606 pp.
33. Ryan SG, Norton AJ (2010) *Stellar Evolution and Nucleosynthesis.* (Cambridge University Press) 236 pp.
34. Heck PR et al. (2007) Presolar He and Ne isotopes in single circumstellar SiC grains. *Astrophys J* 656:1208–1222.
35. Matthews GJ, Bazan G, Cowan JJ (1992) Evolution of heavy-element abundances as a constraint on sites for neutron-capture nucleosynthesis. *Astrophys J* 391:719–735.

36. Padovani P, Matteucci F (1993) Stellar mass loss in elliptical galaxies and the fueiling of active galactic nuclei. *Astrophys J* 416:26–35.
37. Maeder A., Meynet G (1989) Grids of evolutionary models from 0.85 to 120$M_{\odot}$: observational tests and the mass limits. *Astron Astrophys* 210:155–173.
38. Zhukovska S, Gail H-P, Trieloff (2008) Evolution of interstellar dust and stardust in the solar neighbourhood. *Astron Astrophys* 479:453–480.
39. Zhukovska S, Dobbs C., Jenkins EB, Klessen RS (2016) Modeling dust ecolution in galaxies with a multiphase, inhomogeneous ISM. *Astrophys J* 831:147 (15 pp).

36. Padovani P, Matteucci F (1993) Stellar mass loss in elliptical galaxies and the fueiling of active galactic nuclei. *Astrophys J* 416:26–35.
37. Maeder A., Meynet G (1989) Grids of evolutionary models from 0.85 to 120$M_{\odot}$: observational tests and the mass limits. *Astron Astrophys* 210:155–173.
38. Zhukovska S, Gail H-P, Trieloff (2008) Evolution of interstellar dust and stardust in the solar neighbourhood. *Astron Astrophys* 479:453–480.
39. Zhukovska S, Dobbs C., Jenkins EB, Klessen RS (2016) Modeling dust ecolution in galaxies with a multiphase, inhomogeneous ISM. *Astrophys J* 831:147 (15 pp).

PNAS
www.pnas.org

Supplementary Information for

Lifetimes of interstellar dust from presolar silicon carbide cosmic-ray exposure ages

Philipp R. Heck, Jennika Greer, Levke Kööp, Reto Trappitsch, Frank Gyngard, Henner Busemann, Colin Maden, Janaína N. Ávila, Andrew M. Davis, Rainer Wieler

Philipp R. Heck
Email: prheck@fieldmuseum.org

Dataset S1 (SEM images of samples with geometric measurements)

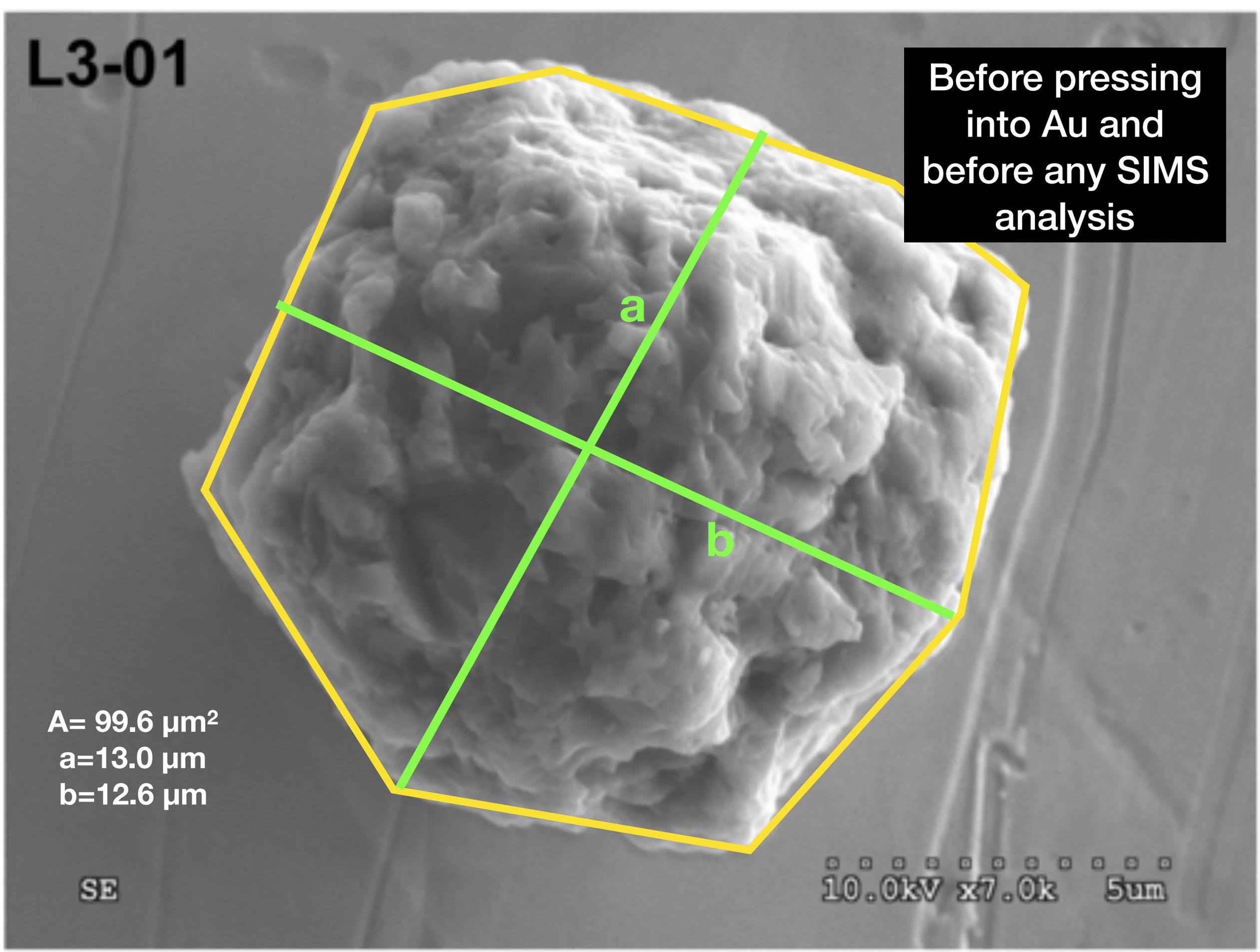
L3-01
Before pressing into Au and before any SIMS analysis
a
b
A= 99.6 µm²
a=13.0 µm
b=12.6 µm
SE
10.0kV x7.0k 5um

L3_1

Before SHRIMP, after NanoSIMS

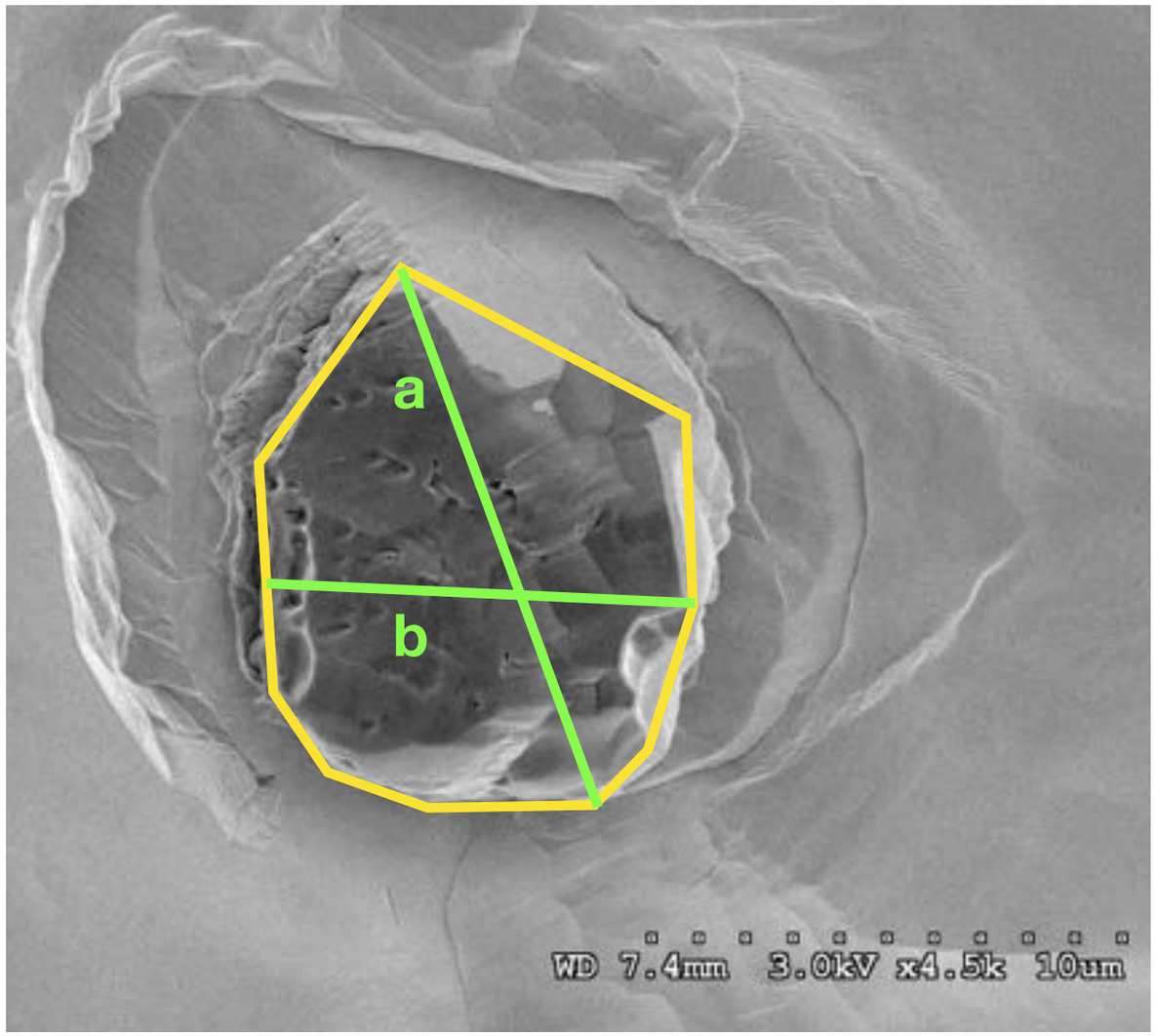

A =69.0 μm^2
a=11.6 μm
b=8.8 μm
geometric mean diameter=9.6 μm
V=A×b=665.5 μm^3

ρ=~3.2 g cm^{-3}; (LS+LU fraction)
M=V×ρ=2.1E-9 g

Before laser, after SIMS

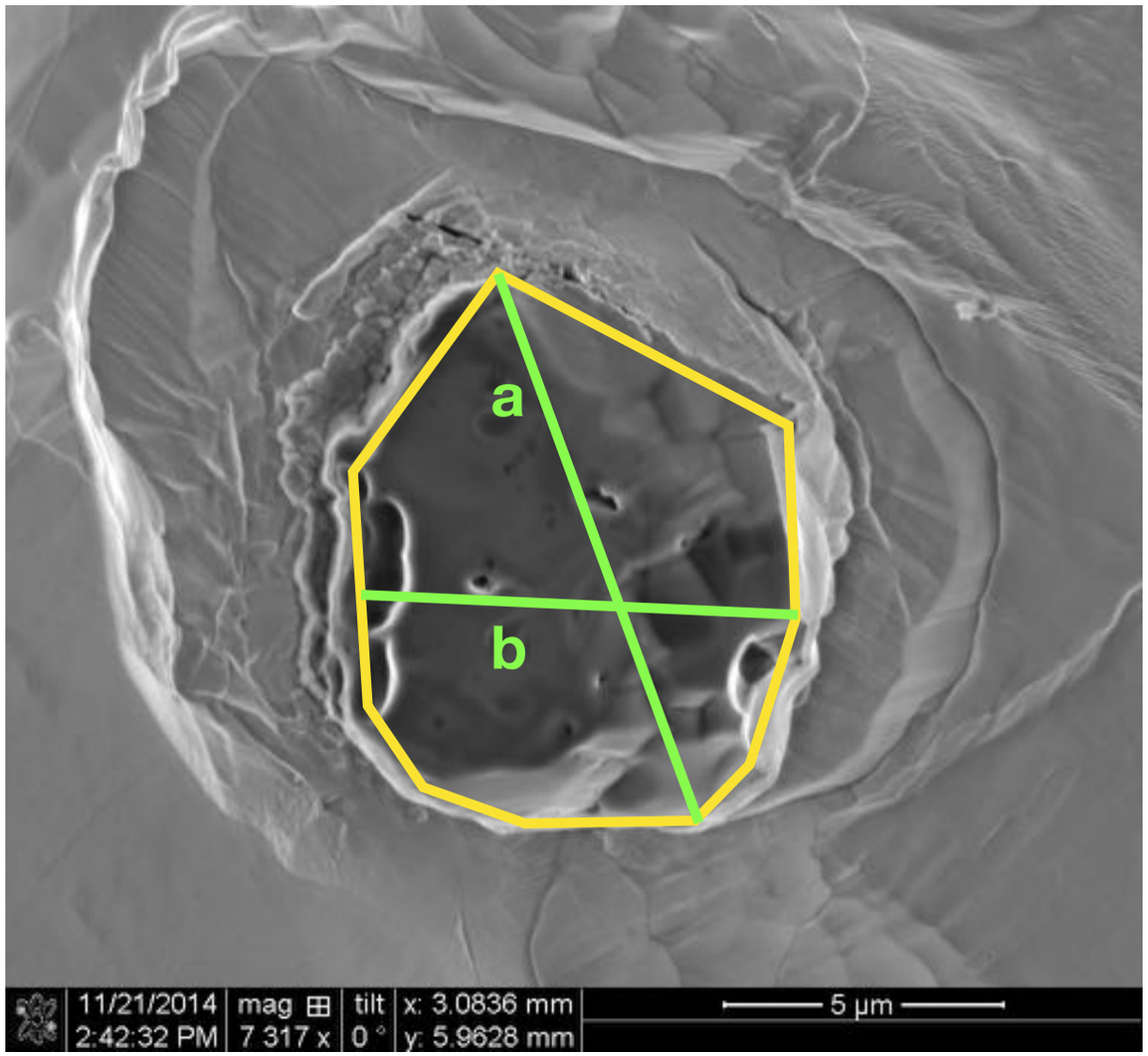

A =64.0 μm^2
a=10.8 μm
b=8.4 μm
geometric mean diameter=9.1 μm
V=A×b=617.4 μm^3

ρ=~3.2 g cm^{-3}; (LS+LU fraction)
M=V×ρ=2.0E-9 g

L3-03

Before pressing into Au and before any SIMS analysis

a

b

A=144.3 μm²
a=16.0 μm
b=11.2 μm

SE

10.0kV x5.0k 10um

L3_3

Before SHRIMP, after NanoSIMS

A = 80.1 μm²
a=12.2 μm
b=5.9 μm
geometric mean diameter=7.5 μm
V=A×b=472.6 μm³

ρ=~3.2 g cm⁻³; (LS+LU fraction)
M=V×ρ=1.9E-9 g

Before laser, after SIMS

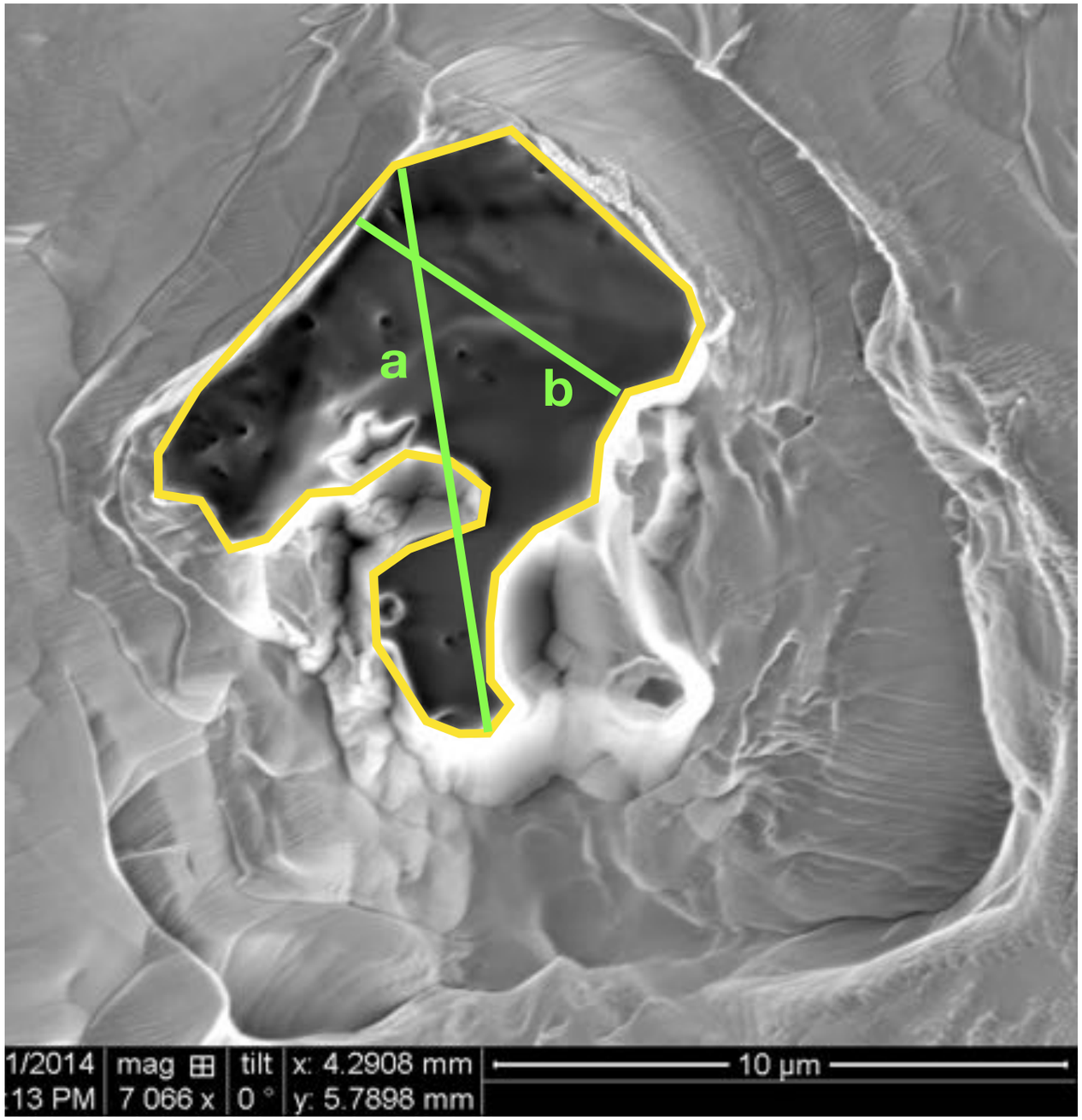

A = 45.7 μm²
a=9.8 μm; b=5.6 μm
geometric mean diameter=6.7 μm
V=A×b=343.5 μm³

ρ=~3.2 g cm⁻³; (LS+LU fraction)
M=V×ρ=1.1E-9 g

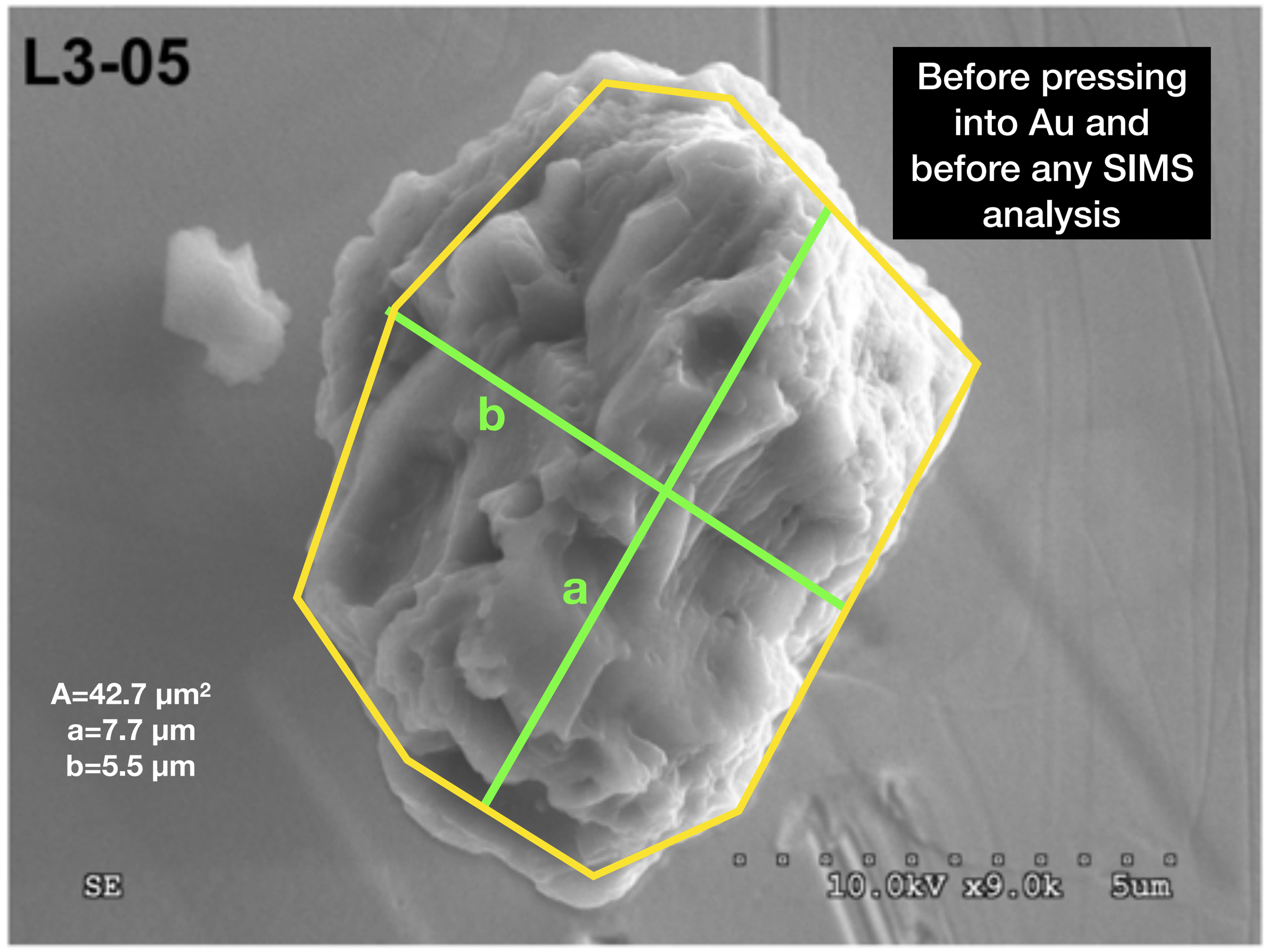
L3-05
Before pressing into Au and before any SIMS analysis
b
a
A=42.7 μm²
a=7.7 μm
b=5.5 μm
SE
10.0kV x9.0k 5um

L3_5

Before SHRIMP, after NanoSIMS

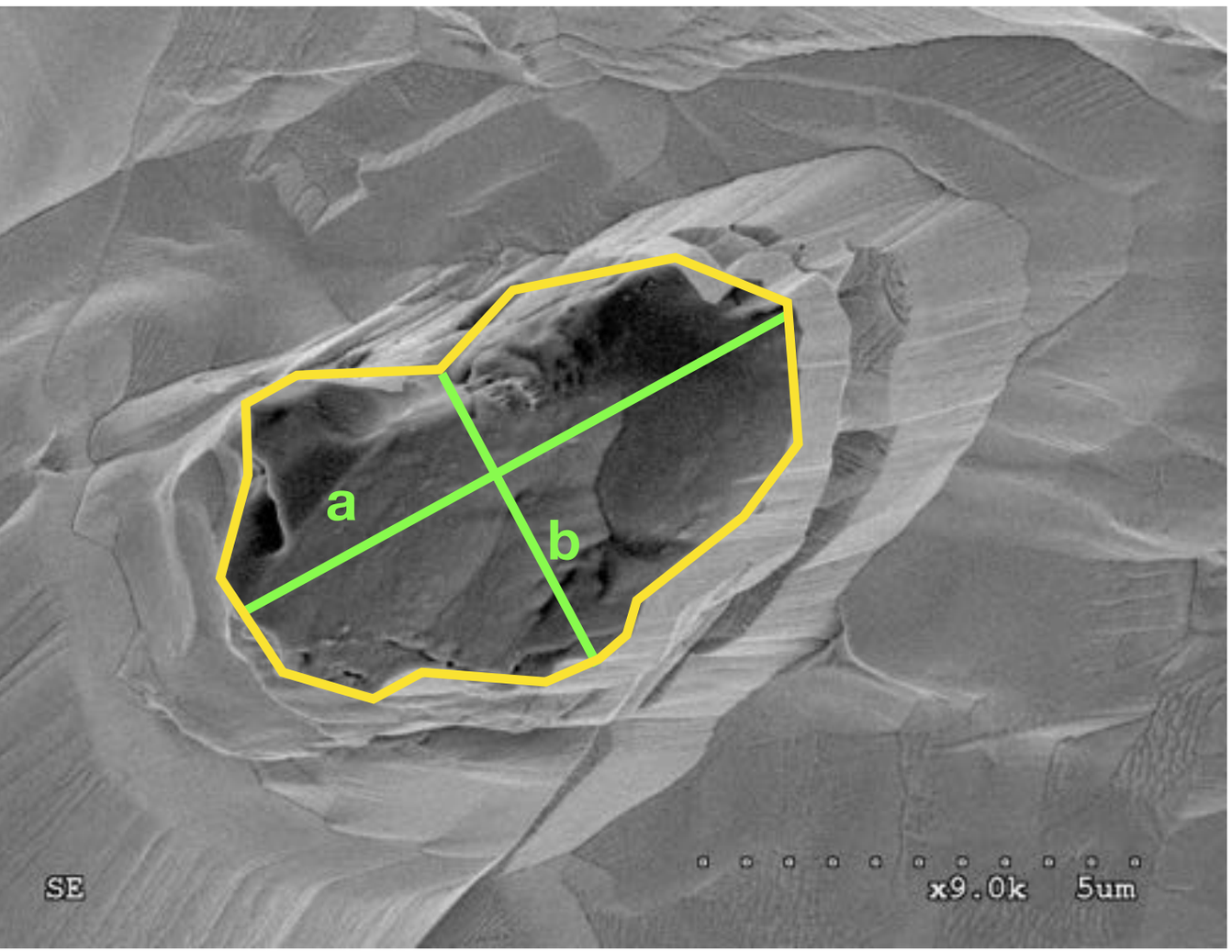

A = 22.6 μm²
a=7.1 μm
b=3.7 μm
geometric mean diameter=4.3 μm
V=A×b=83.6 μm³

ρ=~3.2 g cm⁻³; (LS+LU fraction)
M=V×ρ=2.7E-10 g

Before laser, after SIMS

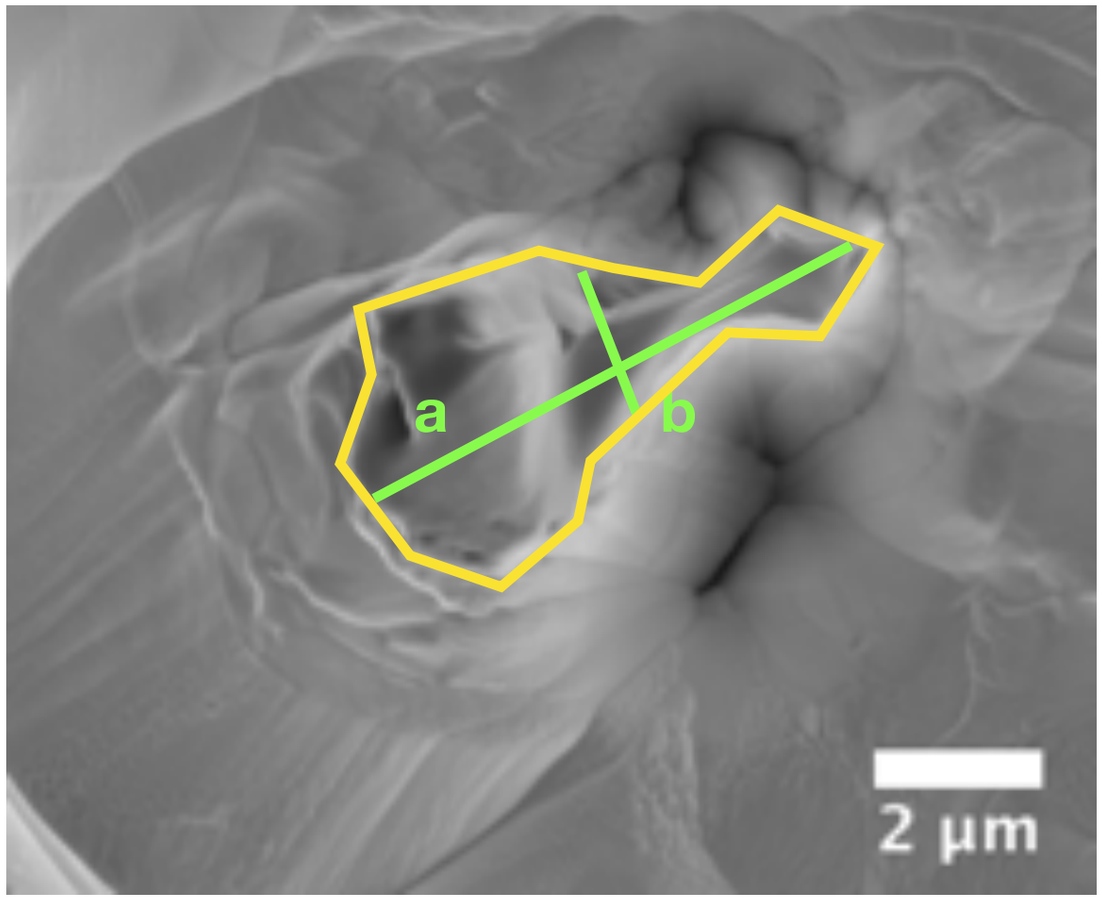

A = 12.8 μm²
a=6.7 μm; b=2.2 μm
geometric mean diameter=3.2 μm
V=A×b=28.2 μm³

ρ=~3.2 g cm⁻³; (LS+LU fraction)
M=V×ρ=9.0E-11 g

L3-06

Before pressing into Au and before any SIMS analysis

b

a

A=46.0 μm²
a=9.7 μm
b=8.9 μm

SE

10.0kV x7.0k 5um

L3_6

Before SHRIMP, after NanoSIMS

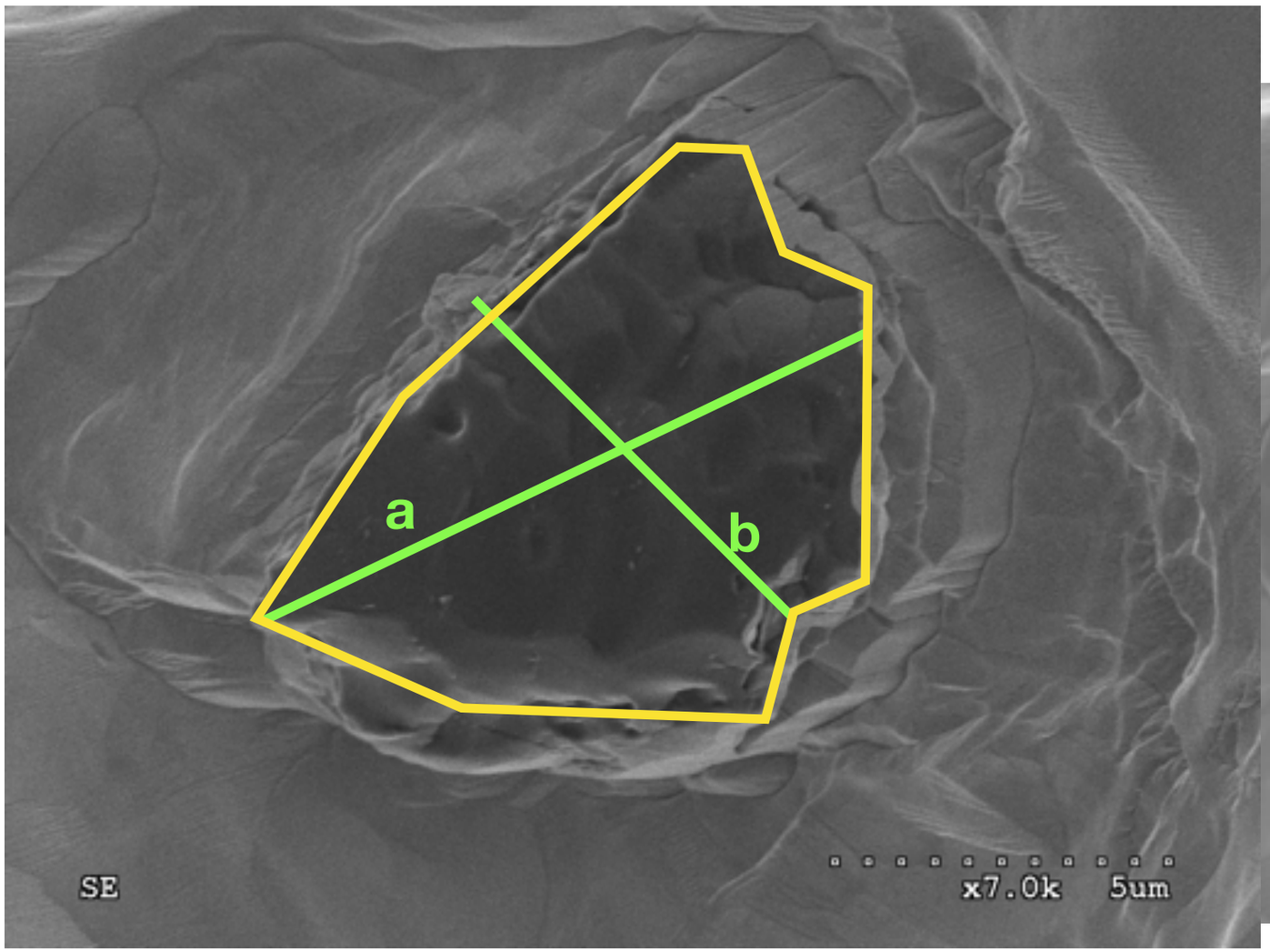

A = 51.6 μm²
a=9.7 μm
b=6.0 μm
geometric mean diameter=7.0 μm
V=A×b=361.2 μm³

ρ=~3.2 g cm⁻³; (LS+LU fraction)
M=V×ρ=1.2E-9 g

Before laser, after SIMS

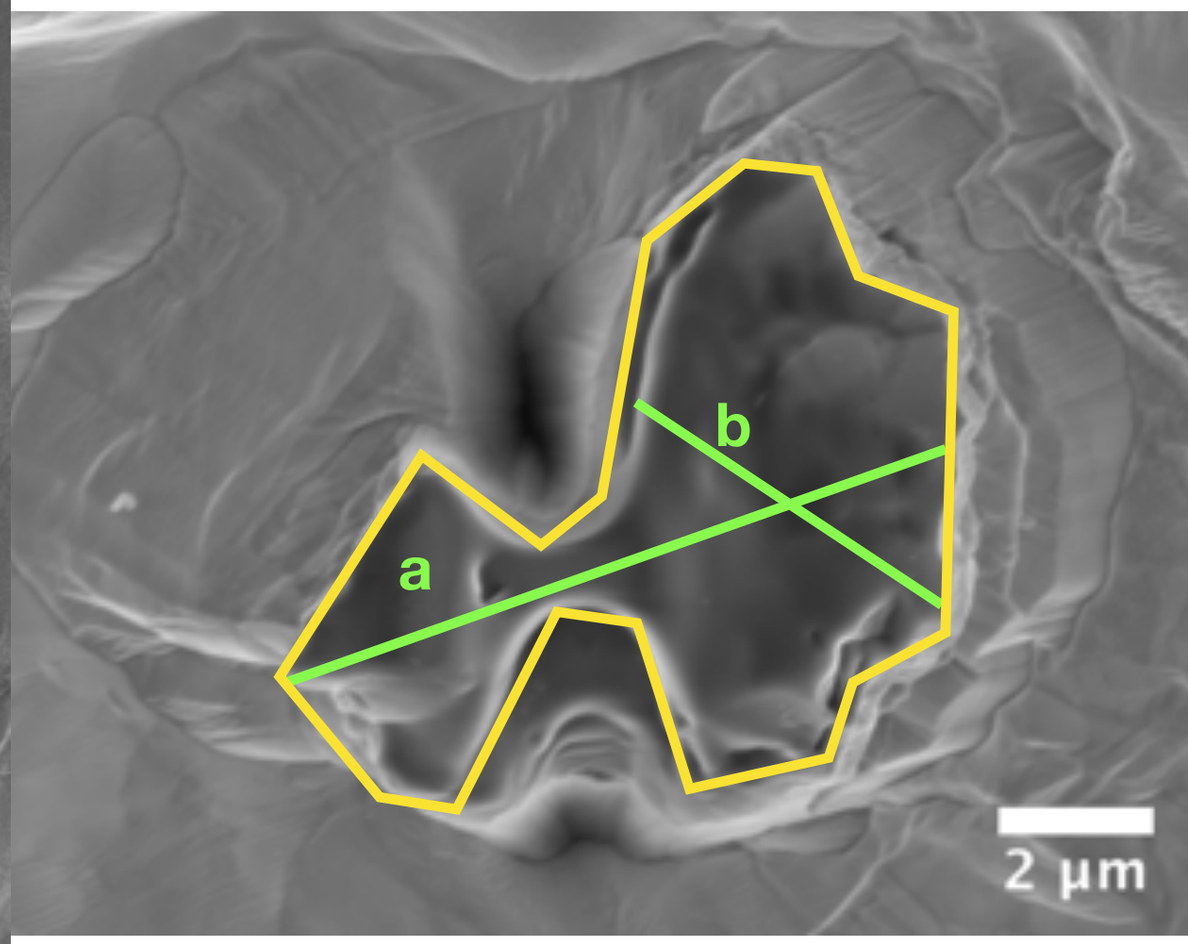

A = 38.3 μm²
a=8.9 μm; b=5.1 μm
geometric mean diameter=6.1 μm
V=A×b=269.7 μm³

ρ=~3.2 g cm⁻³; (LS+LU fraction)
M=V×ρ=8.6E-10 g

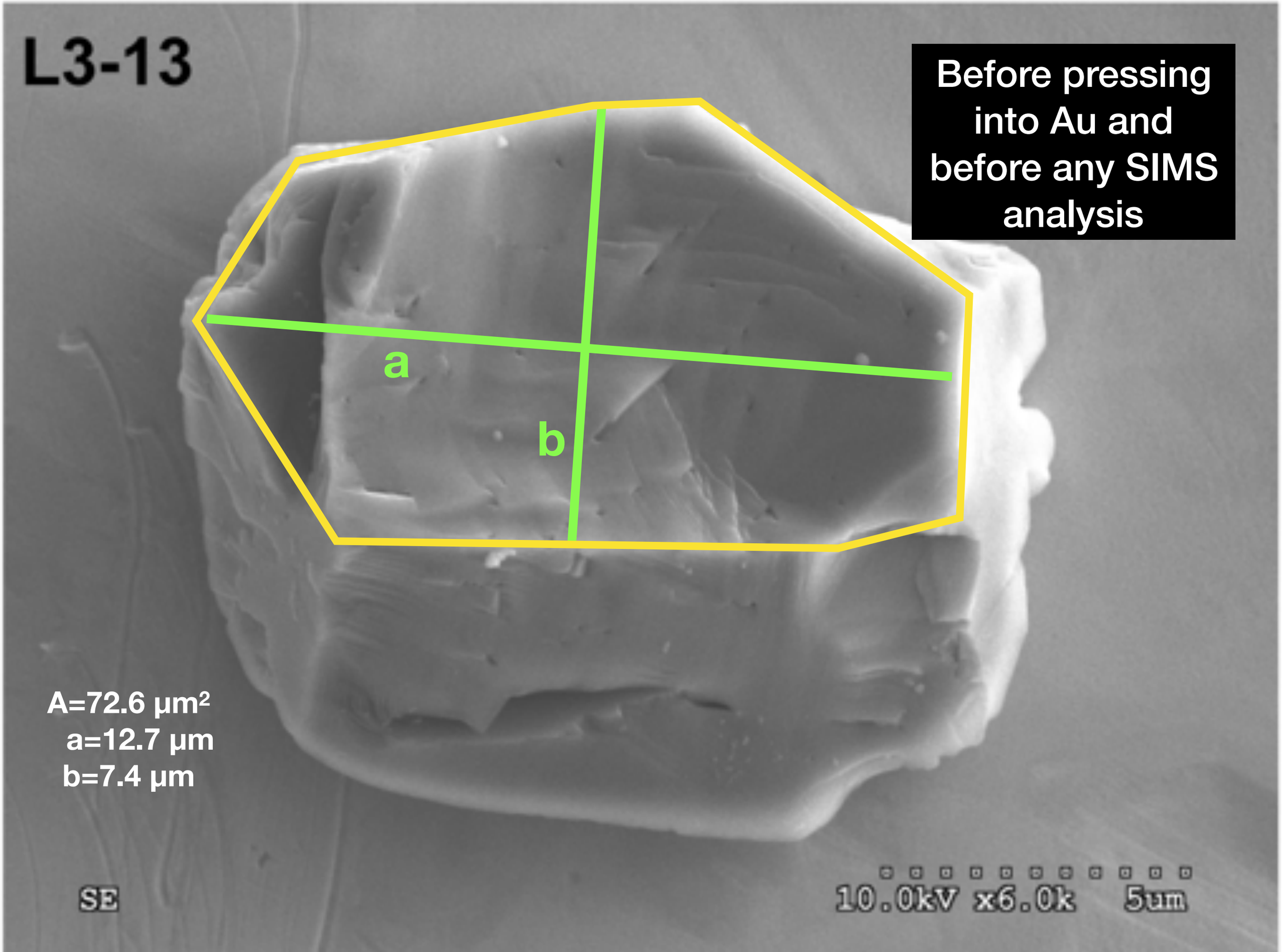
L3-13
Before pressing into Au and before any SIMS analysis
a
b
A=72.6 µm²
a=12.7 µm
b=7.4 µm
SE
10.0kV x6.0k 5um

L3_13

Before SHRIMP, after NanoSIMS

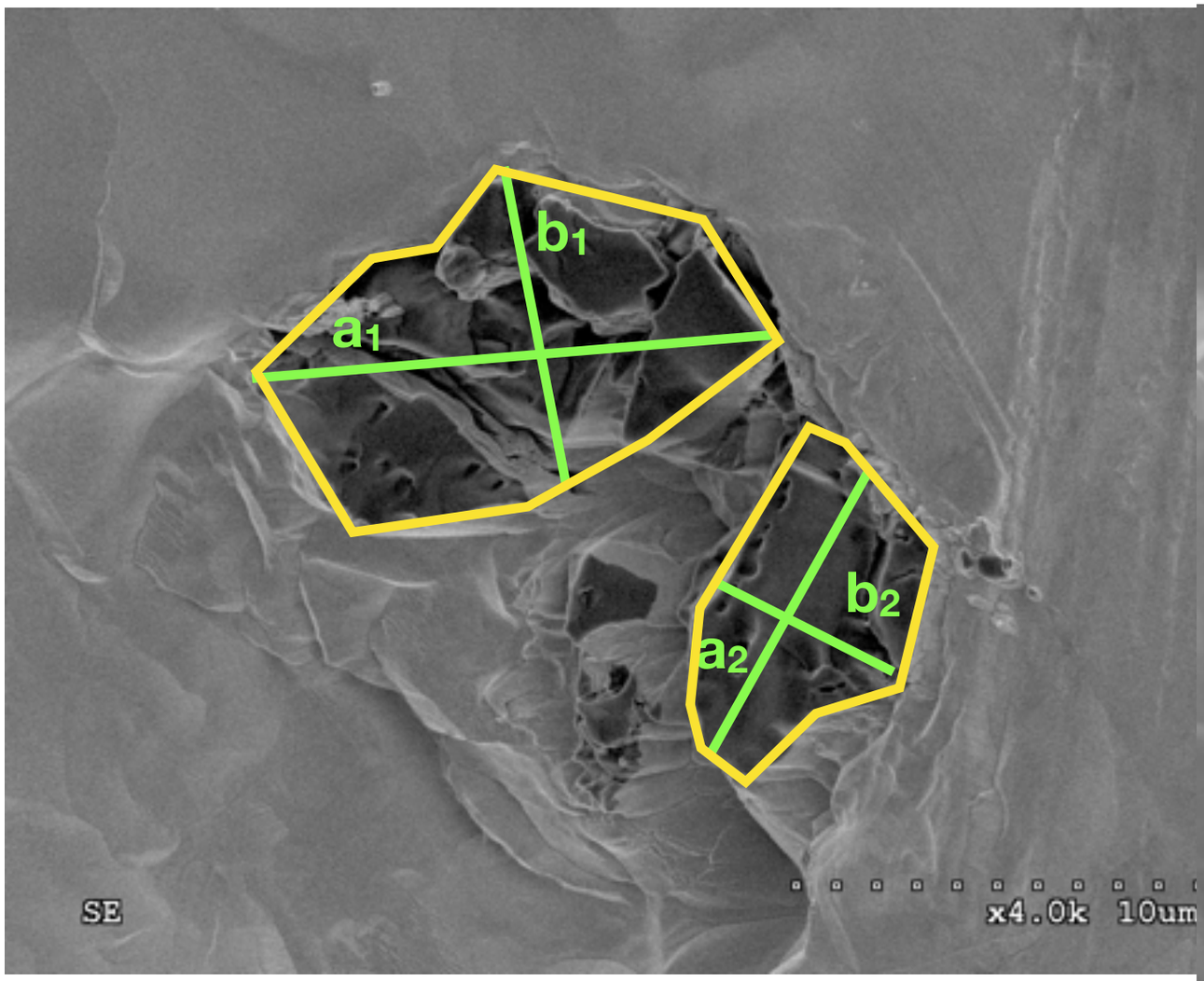

A_1 =72.0 μm²
a_1=12.9 μm
b_1=8.2 μm
$V_1=A_1\times b_1$=590.4 μm³

A_2 = 33.6 μm²
a_2=9.0 μm
b_2=4.7 μm
$V_2=A_2\times b_2$=157.9 μm³

$A=A_1+A_2$ 105.6 μm²
geometric mean diameter=8.2 μm
$V=V_1+V_2$=748.3 μm³

ρ=~3.2 g cm⁻³; (LS+LU fraction)
$M=V\times\rho$=2.39E-9 g

Before laser, after SIMS

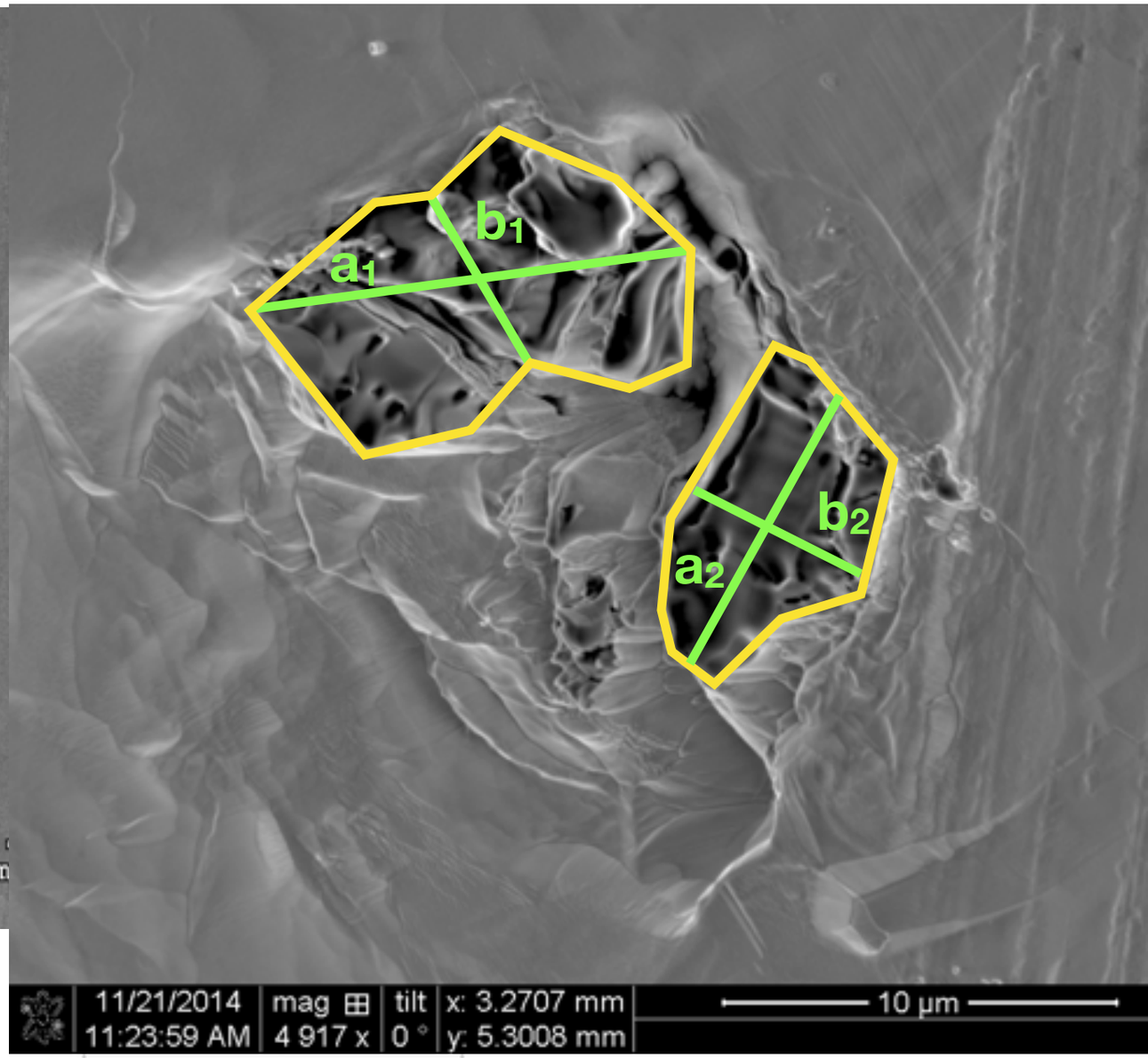

A_1 =56.1 μm²
a_1=11.1 μm
b_1=5.5 μm
$V_1=A_1\times b_1$= 308.6 μm³

A_2 = 32.5 μm²
a_2=8.0 μm
b_2=4.7 μm
$V_2=A_2\times b_2$=152.8 μm³

$A=A_1+A_2$ 105.6 μm²
geometric mean diameter=7.0 μm
$V=V_1+V_2$=461 μm³

ρ=~3.2 g cm⁻³; (LS+LU fraction)
$M=V\times\rho$=1.48E-9 g

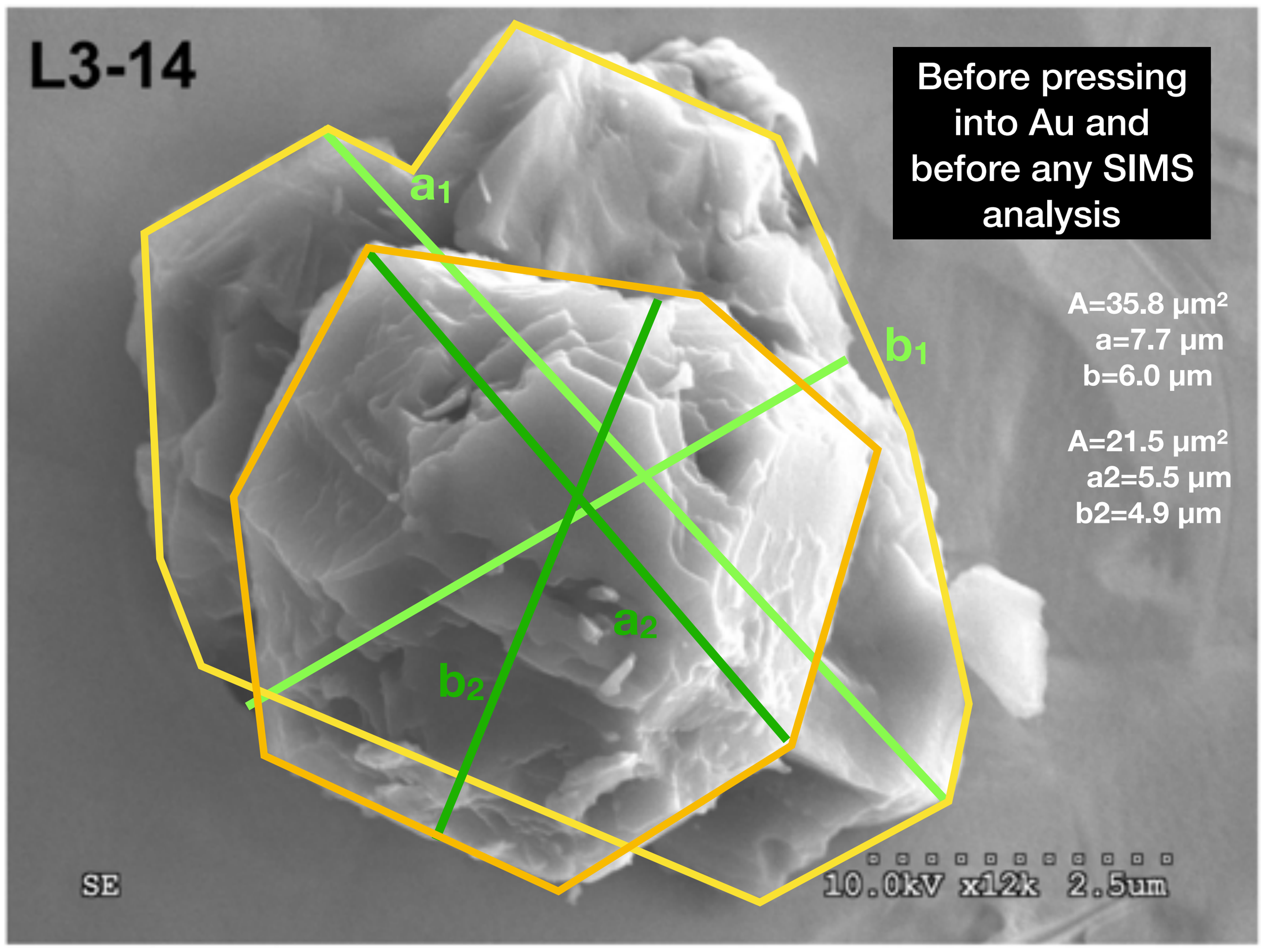
L3-14
Before pressing into Au and before any SIMS analysis
a1
b1
a2
b2
A=35.8 µm²
a=7.7 µm
b=6.0 µm
A=21.5 µm²
a2=5.5 µm
b2=4.9 µm
SE
10.0kV x12k 2.5um

L3_14

Before SHRIMP, after NanoSIMS

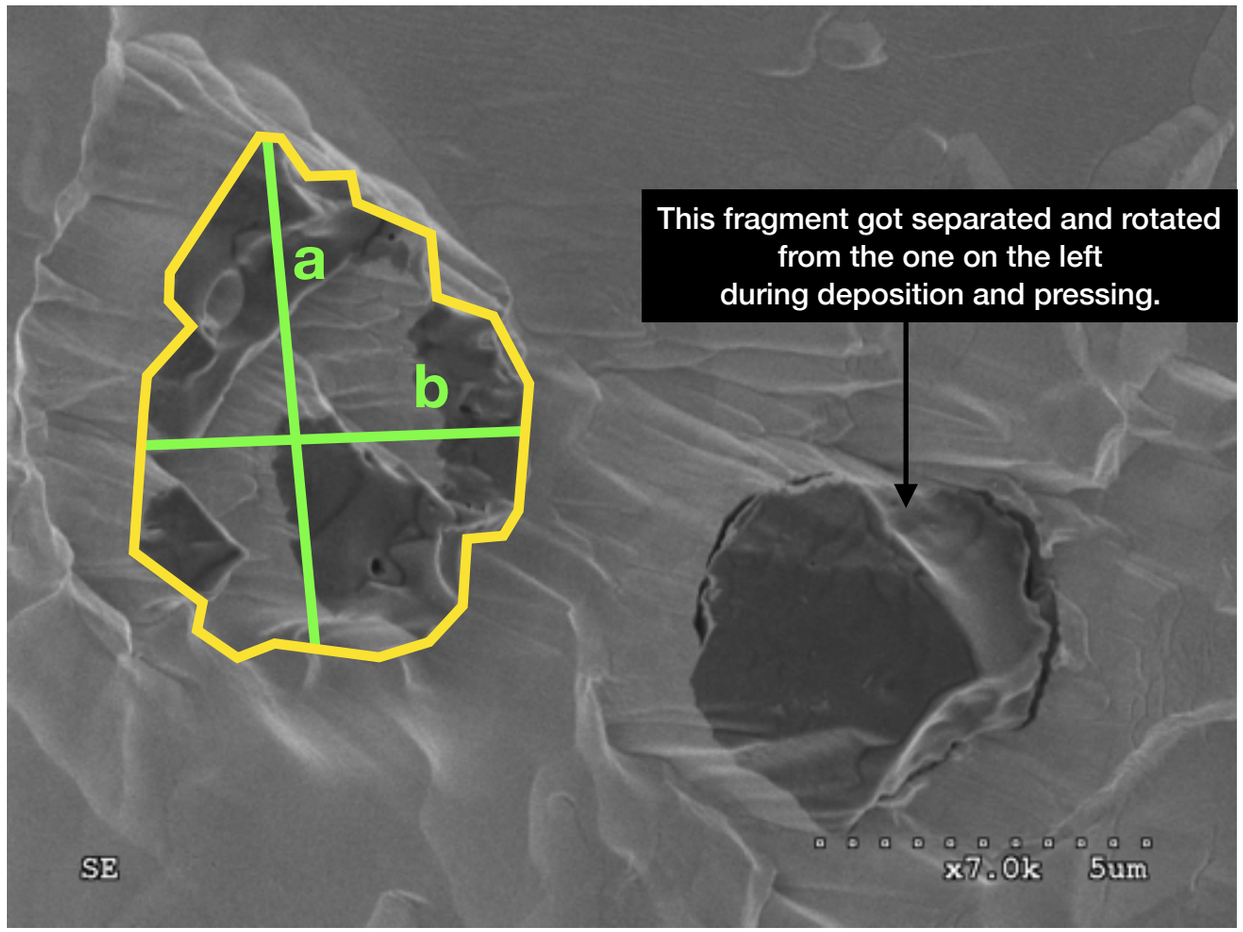

A = 29.1 μm²
a=9.7 μm
b=6.0 μm
geometric mean diameter=7.0 μm
V=A×b=204.9 μm³

ρ=~3.2 g cm⁻³; (LS+LU fraction)
M=V×ρ=6.6E-10 g

Before laser, after SIMS

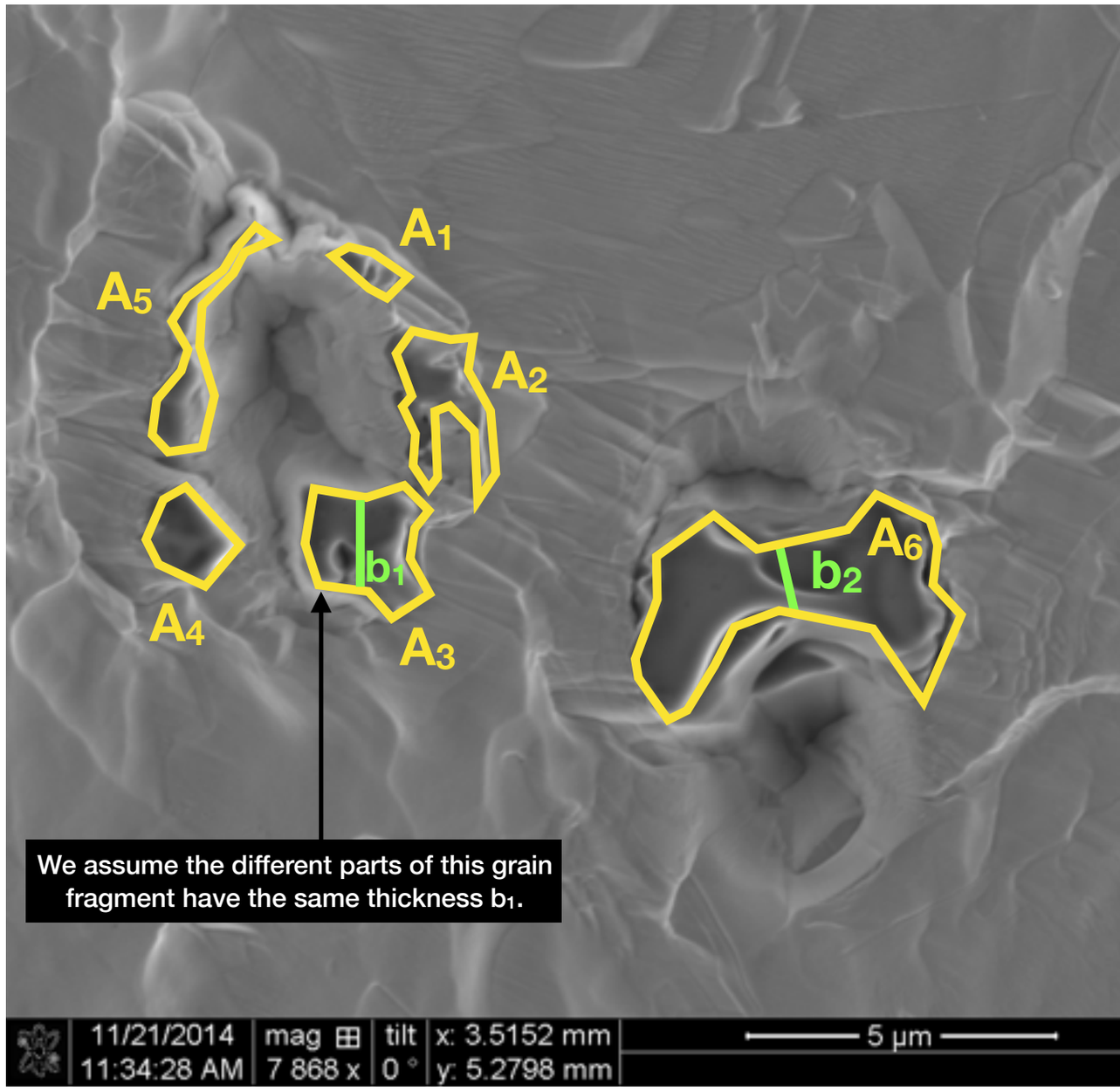

A_1 =0.4 μm²
A_2 =2.1 μm²
A_3 =3.0 μm²
A_4 =1.4 μm²
A_5 =1.7 μm²
b_1=1.4 μm
$V_1=b_1\times\sum A_i$=11.8 μm³

A_6 =9.0 μm²
b_2= 1.2 μm
$V_2=A_2\times b_2$=10.8 μm³

geometric mean diameter= μm
$V=V_1+V_2$=22.6 μm³

ρ=~3.2 g cm⁻³; (LS+LU fraction)
M=V×ρ=7.2E-11 g

L3-17

Before SIMS analysis

a

b

A=41.8 µm²
a=7.9 µm
b=6.8 µm

SE

10.0kV x9.0k 5um

L3_17

Before SHRIMP, after NanoSIMS

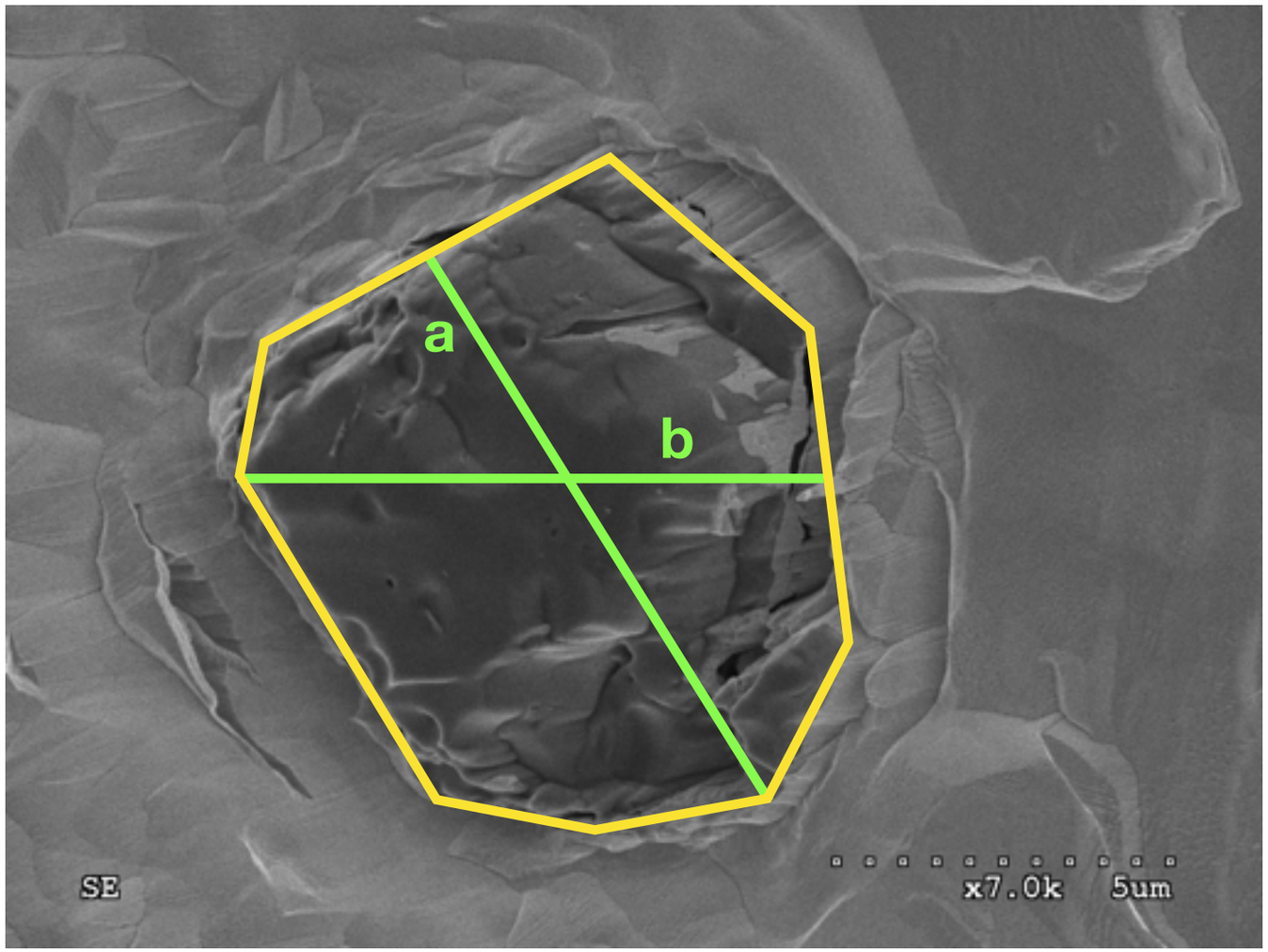

A = 60.6 μm^2
a=9.2 μm
b=8.6 μm
geometric mean diameter=8.8 μm
V=A×b=533.3 μm^3

ρ=~3.2 g cm^{-3}; (LS+LU fraction)
M=V×ρ=1.7E-9 g

Before laser, after SIMS

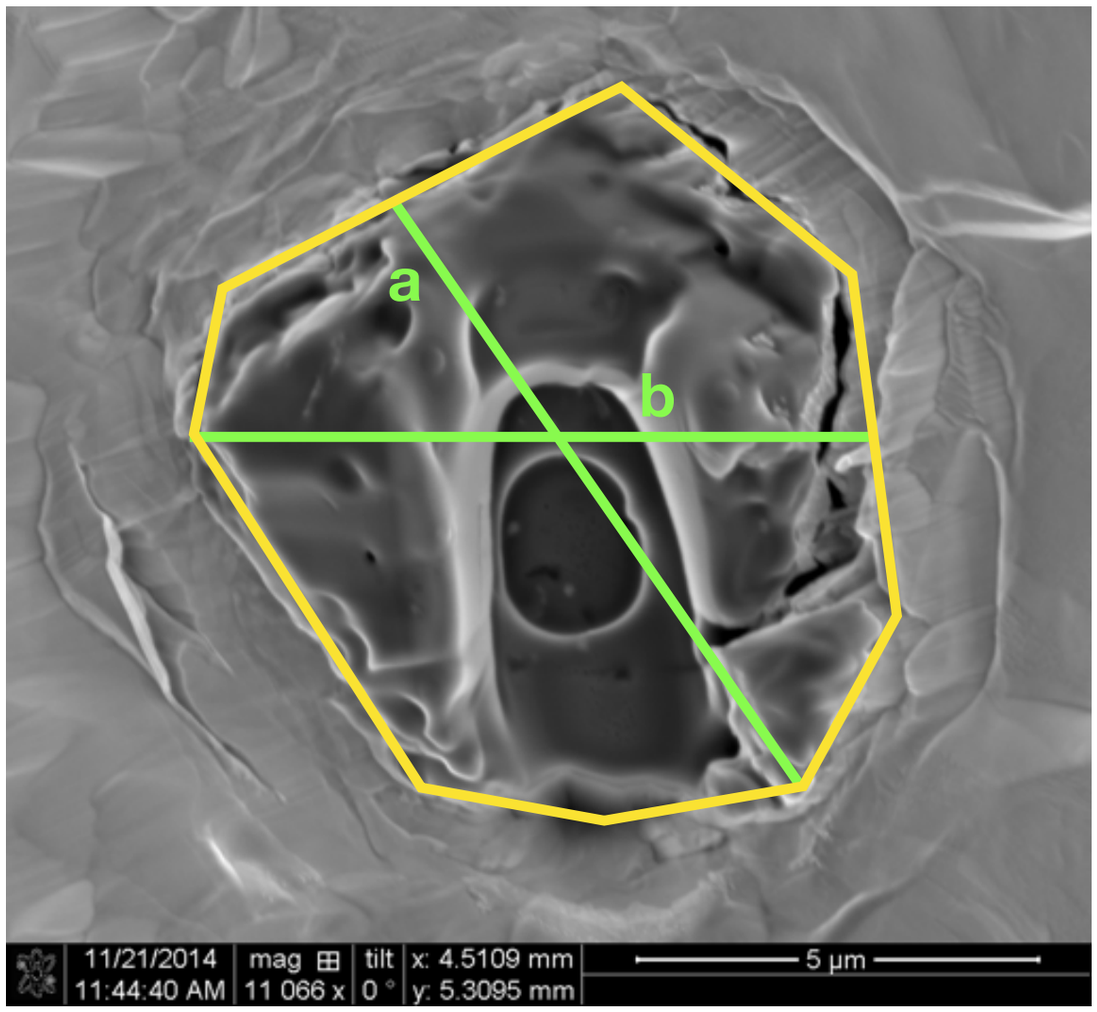

A = 56.8 μm^2
a=9.2 μm; b=8.5 μm
geometric mean diameter=8.7 μm
V=A×b=500.3 μm^3

ρ=~3.2 g cm^{-3}; (LS+LU fraction)
M=V×ρ=1.6E-9 g

L3-18

Before SIMS analysis

a

b

A=239.2 μm²
a=19.2 μm
b=13.8 μm

SE

10.0kV x4.0k 10um

L3_18

Before SHRIMP, after NanoSIMS

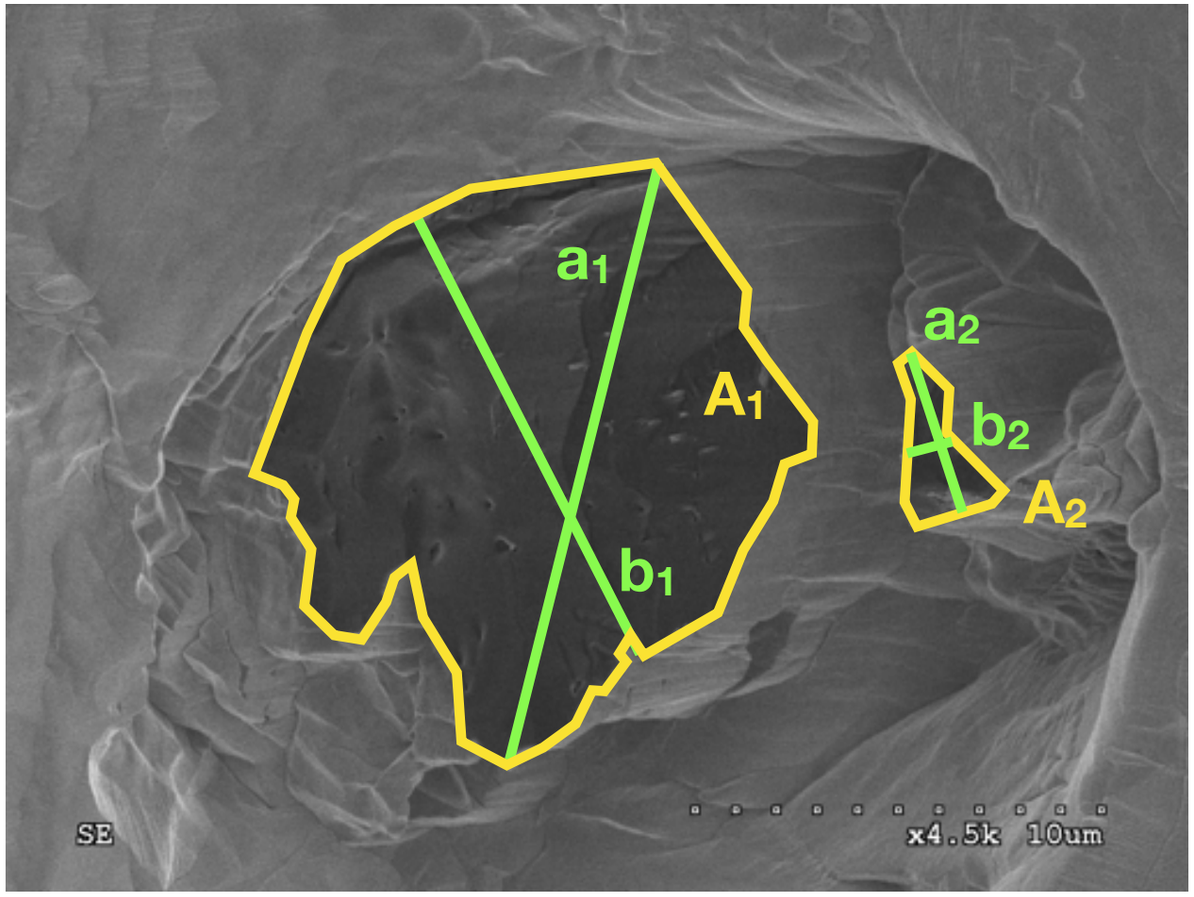

A_1 =120.5 μm²
a_1=14.8 μm
b_1=11.7 μm
$V_1=A_1\times b_1$=1408 μm³

A_2 = 5.3 μm²
a_2=3.9 μm
b_2=1.3 μm
$V_2=A_2\times b_2$=6.7 μm³

geometric mean diameter=12.7 μm
$V=V_1+V_2$=1415 μm³

ρ=~3.2 g cm⁻³; (LS+LU fraction)
$M=V\times\rho$=4.5E-9 g

Before laser, after SIMS

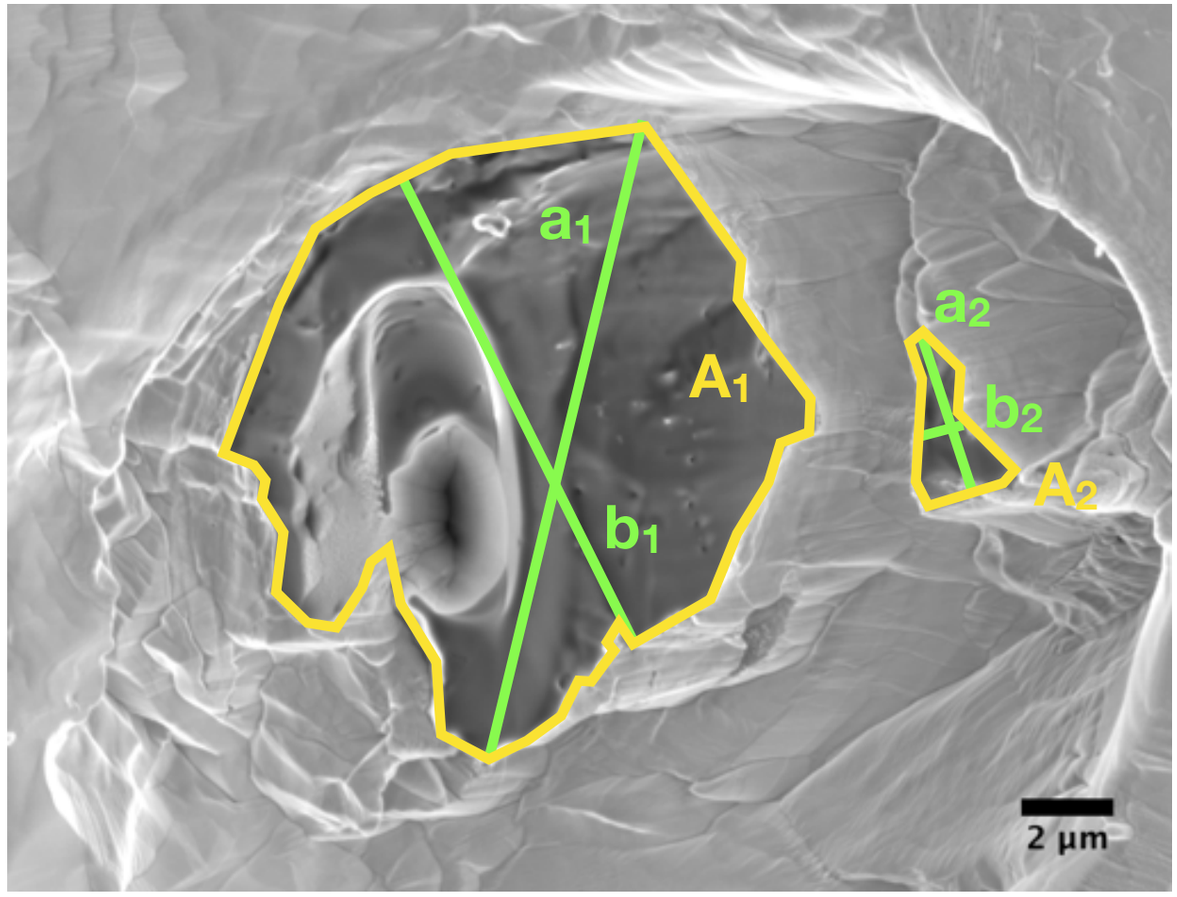

A_1 =110.4 μm²
a_1=14.0 μm
b_1=11.3 μm
$V_1=A_1\times b_1$= 1250 μm³

A_2 =4.6 μm²
a_2=3.7 μm
b_2=1.2 μm
$V_2=A_2\times b_2$=5.7 μm³

$A=A_1+A_2$ 115 μm²
geometric mean diameter=7.0 μm
$V=V_1+V_2$=1255 μm³

ρ=~3.2 g cm⁻³; (LS+LU fraction)
$M=V\times\rho$=4.0E-9 g

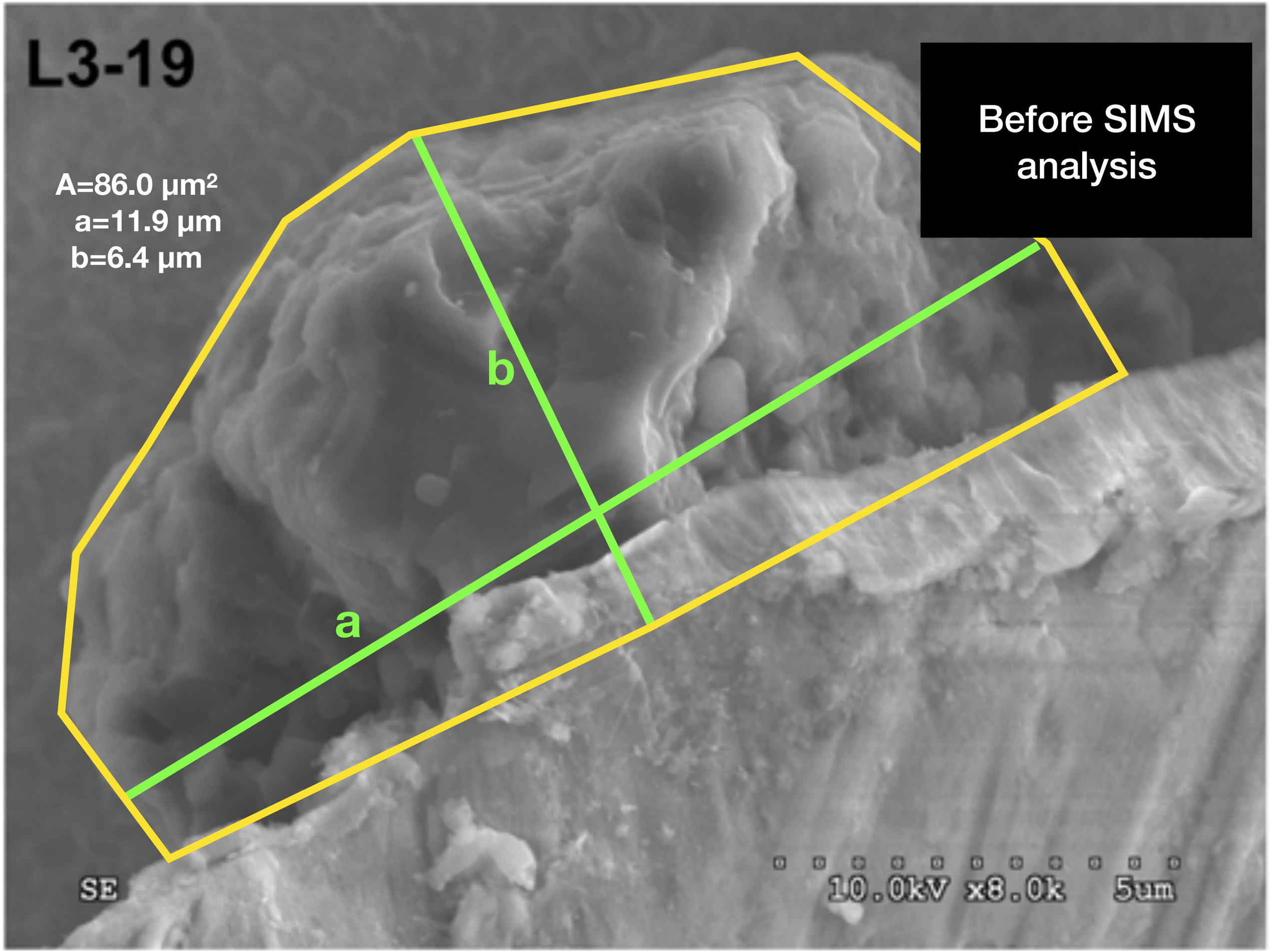
L3-19
A=86.0 µm²
a=11.9 µm
b=6.4 µm
Before SIMS analysis
b
a
SE
10.0kV x8.0k 5um

L3_19

Before SHRIMP, after NanoSIMS

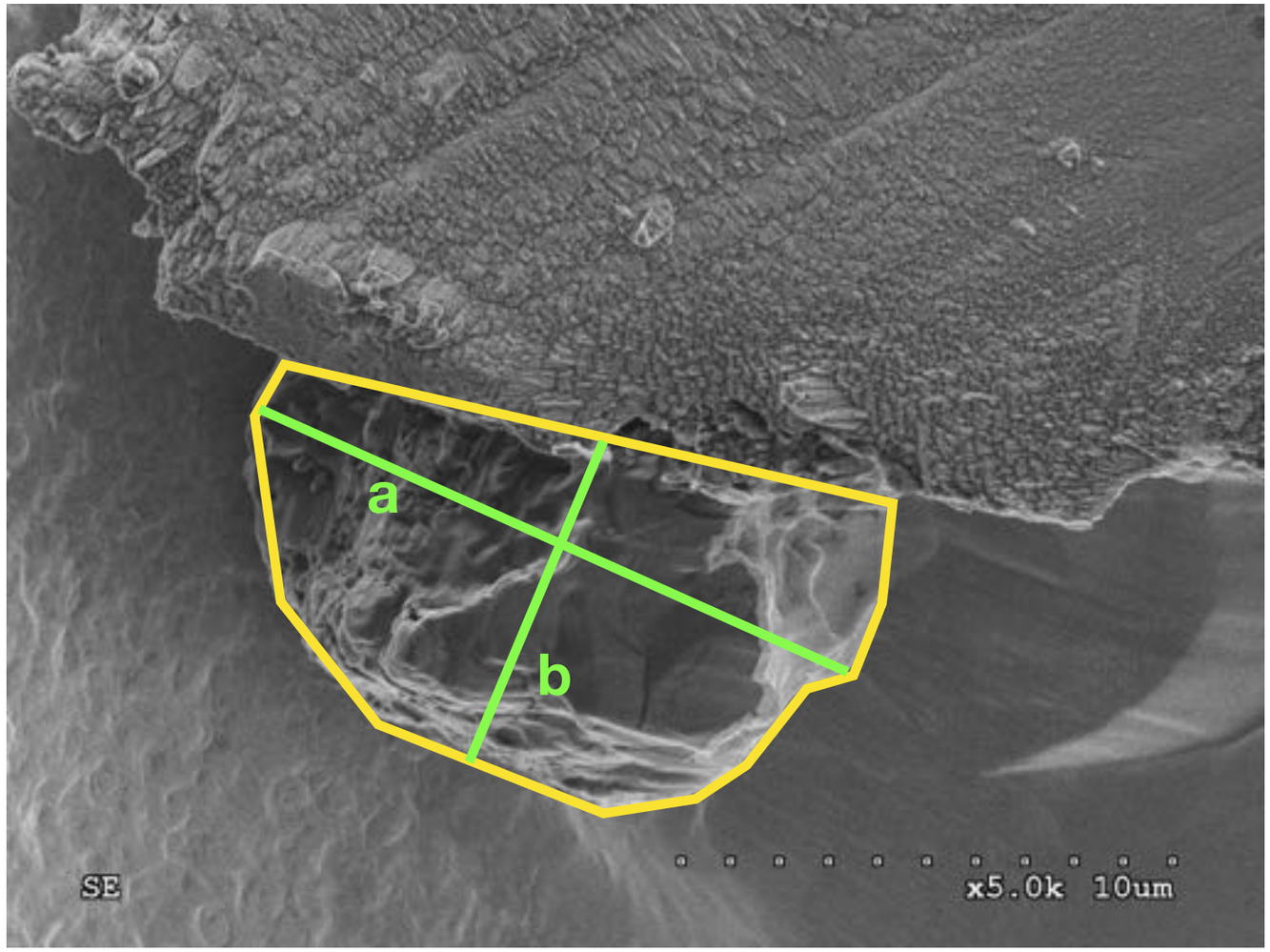

A = 78.6 μm² (lower limit)
a=13.0 μm
b=6.6 μm (lower limit)
geometric mean diameter=8.3 μm
V=A×b=634 μm³

ρ=~3.2 g cm⁻³; (LS+LU fraction)
M=V×ρ=2.0E-9 g

Before laser, after SIMS

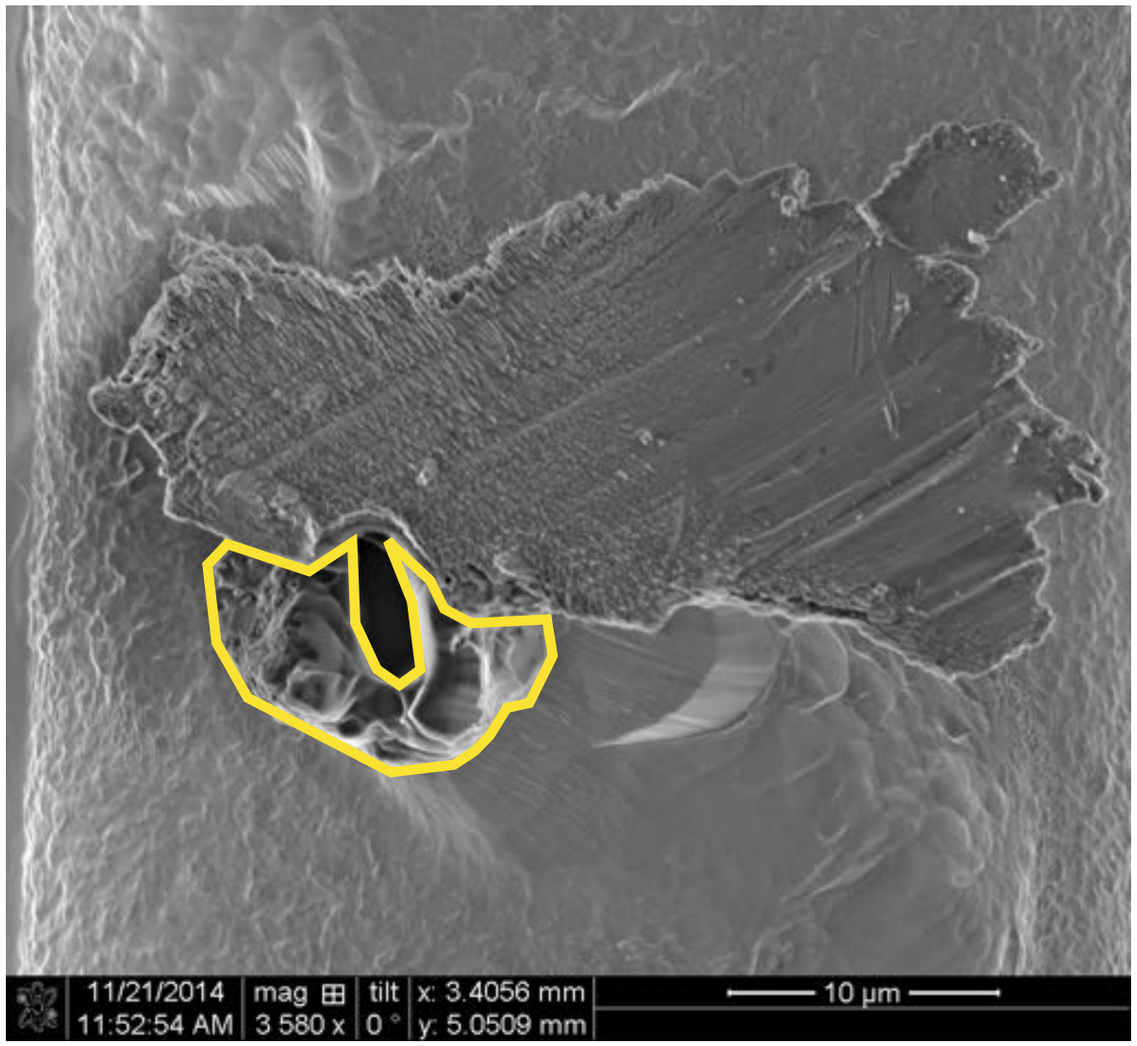

A = 60.3 μm² (lower limit)
a=12.7 μm
b=6.6 μm (lower limit)
geometric mean diameter=8.2 μm
V=A×b=499 μm³

ρ=~3.2 g cm⁻³; (LS+LU fraction)
M=V×ρ=1.6E-9 g

L3-20

Before pressing into Au and before any SIMS analysis

a

b

A=232.0 μm²
a=21.8 μm
b=11.2 μm

SE

10.0kV x3.5k 10um

L3_20

Before SHRIMP, after NanoSIMS

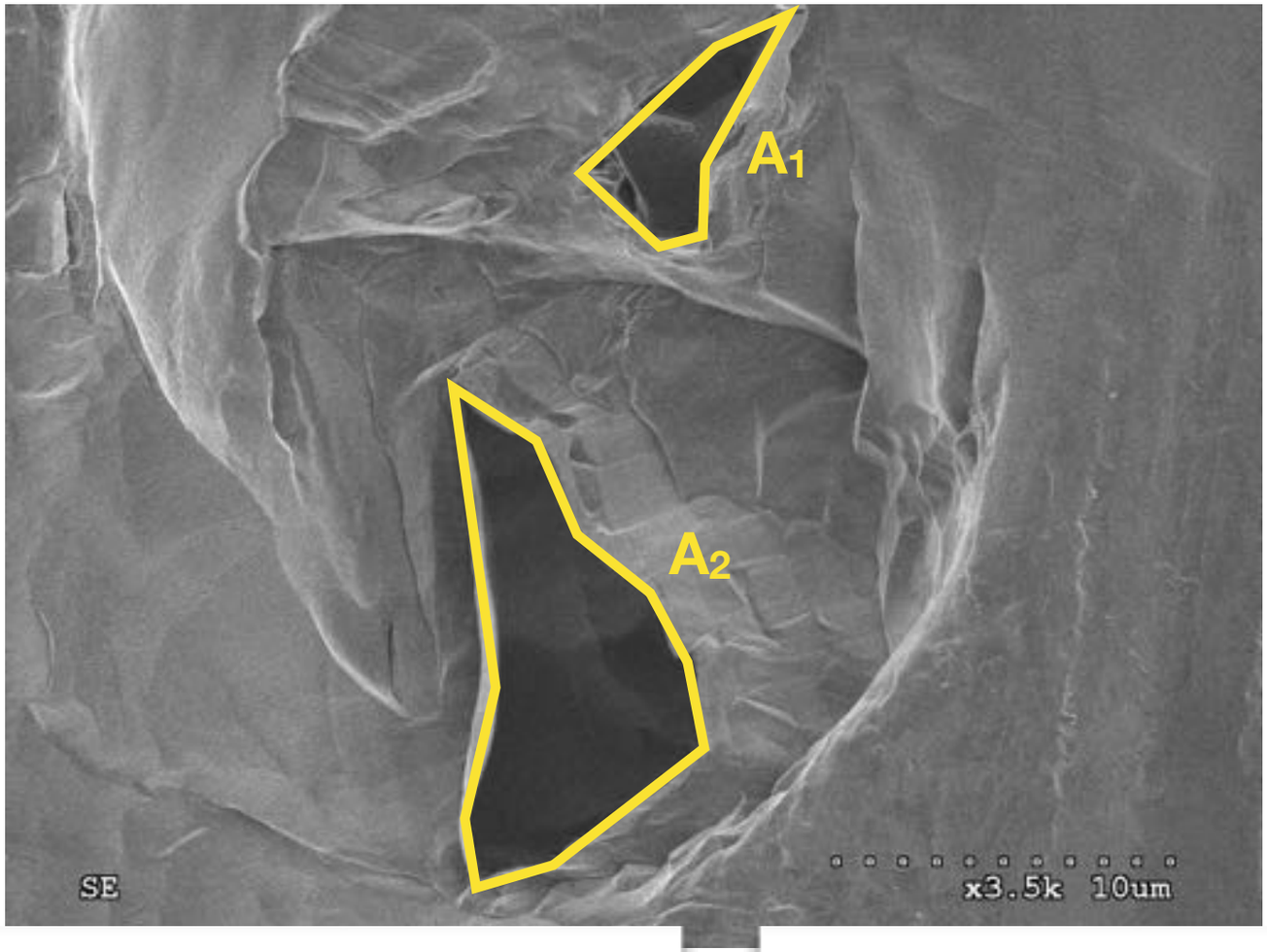

A_1 = 53.8 µm^2
a_1=13.2 µm
b_1=4.9 µm
V_1=A_1×b_1=262 µm^3

ρ=~3.2 g cm^{-3}; (LS+LU fraction)
M_1=V_1×ρ=8.4E-10 g

Before laser, after SIMS

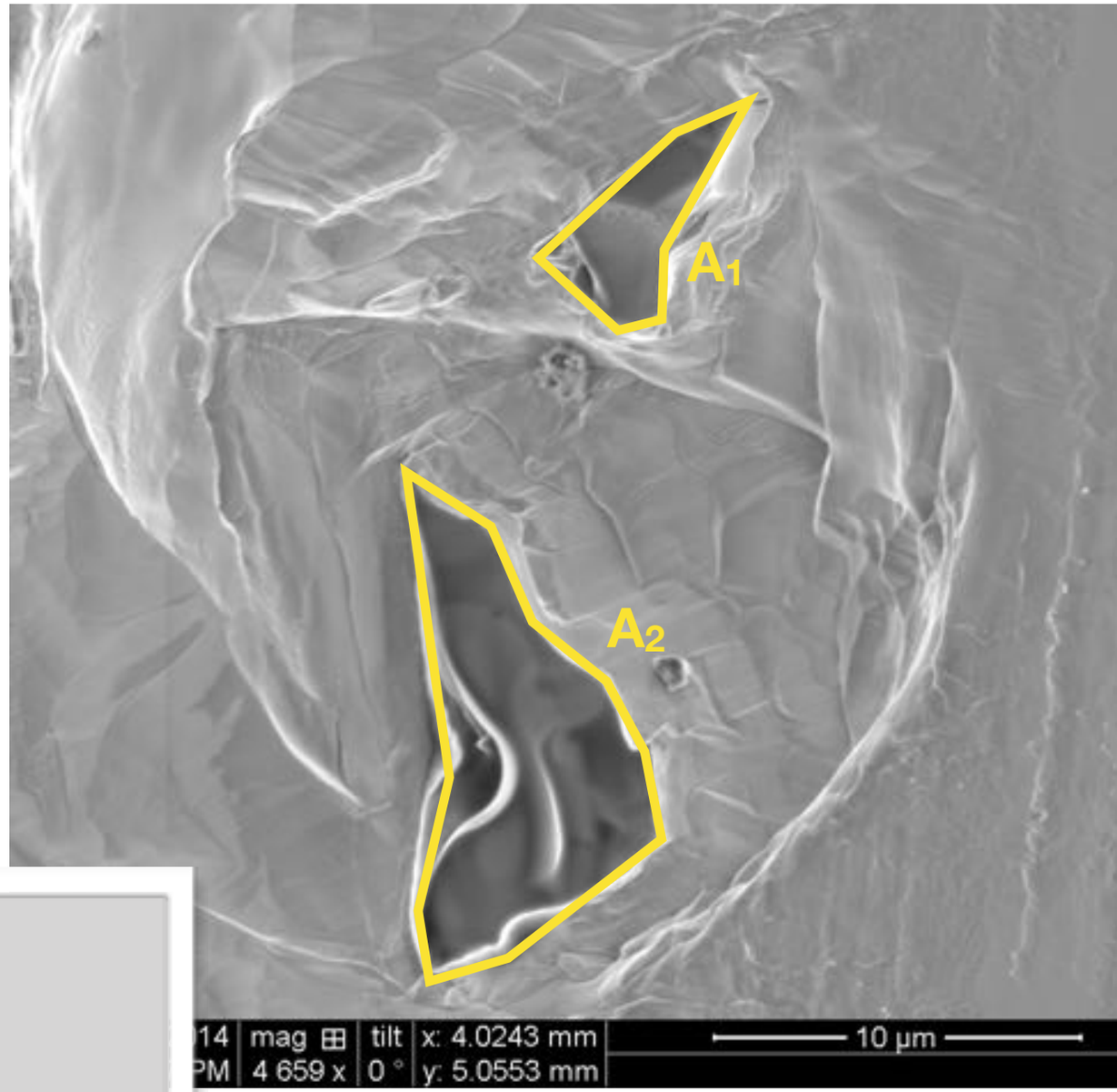

A_2 = 15.5 µm^2
a_2=6.6 µm
b_2=2.4 µm
V_2=A_2×b_2=37 µm^3

ρ=~3.2 g cm^{-3}; (LS+LU fraction)
M_2=V_2×ρ=1.2E-10 g

geometric mean diameter=5.7 µm
A_{1+2}=69.3 µm^2
V_{1+2}=300 µm^3
M_{1+2}=9.6E-10 g

L3-24

Before SIMS analysis

b

a

A=47.9 µm²
a=10.2 µm
b=7.0 µm

SE

10.0kV x6.0k 5um

L3_24

Before SHRIMP, after NanoSIMS

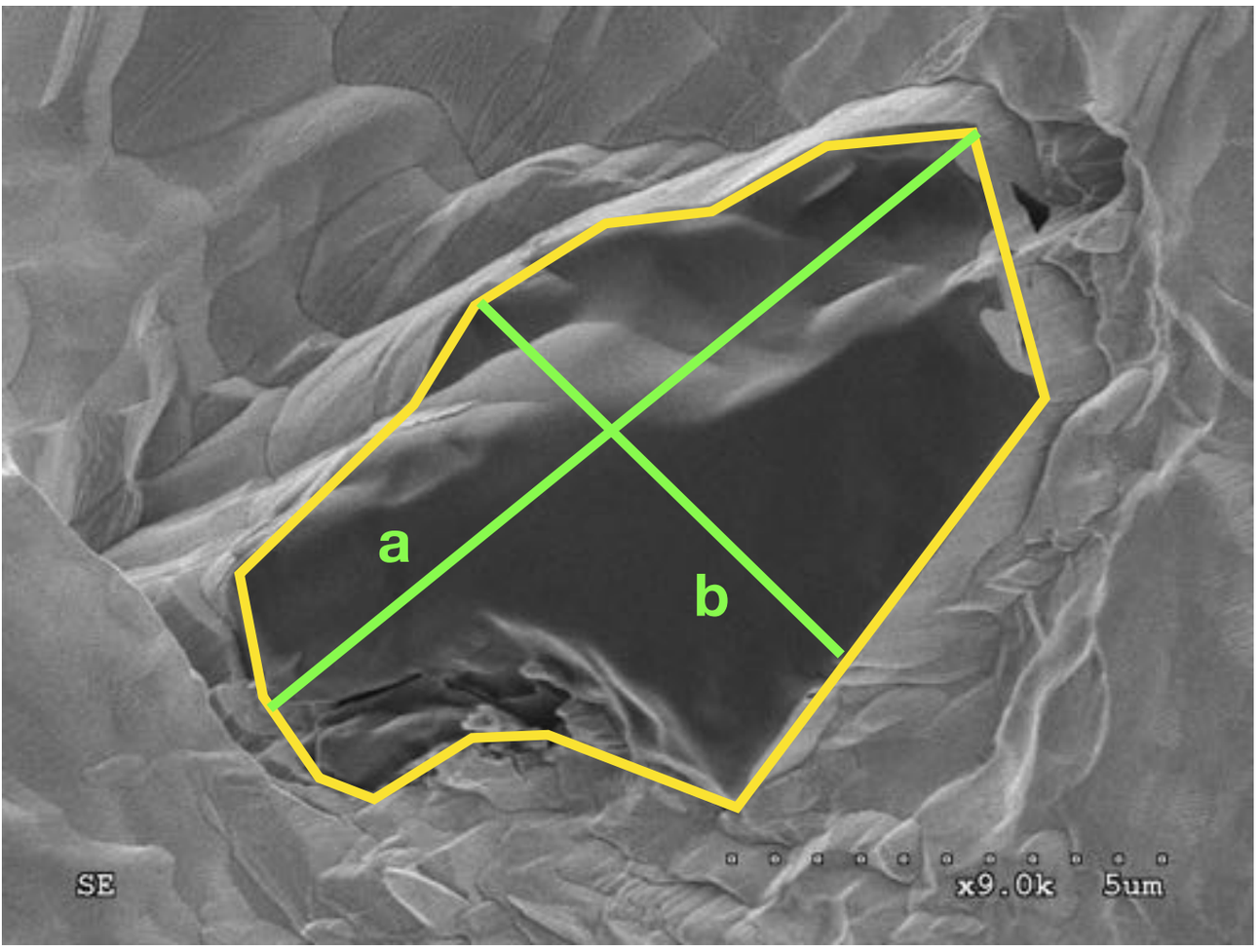

A = 43.7 μm^2
a=10.3 μm
b=6.0 μm
V=A×b=261 μm^3

ρ=~3.2 g cm^{-3}; (LS+LU fraction)
M=V×ρ=8.4E-10 g

Before laser, after SIMS

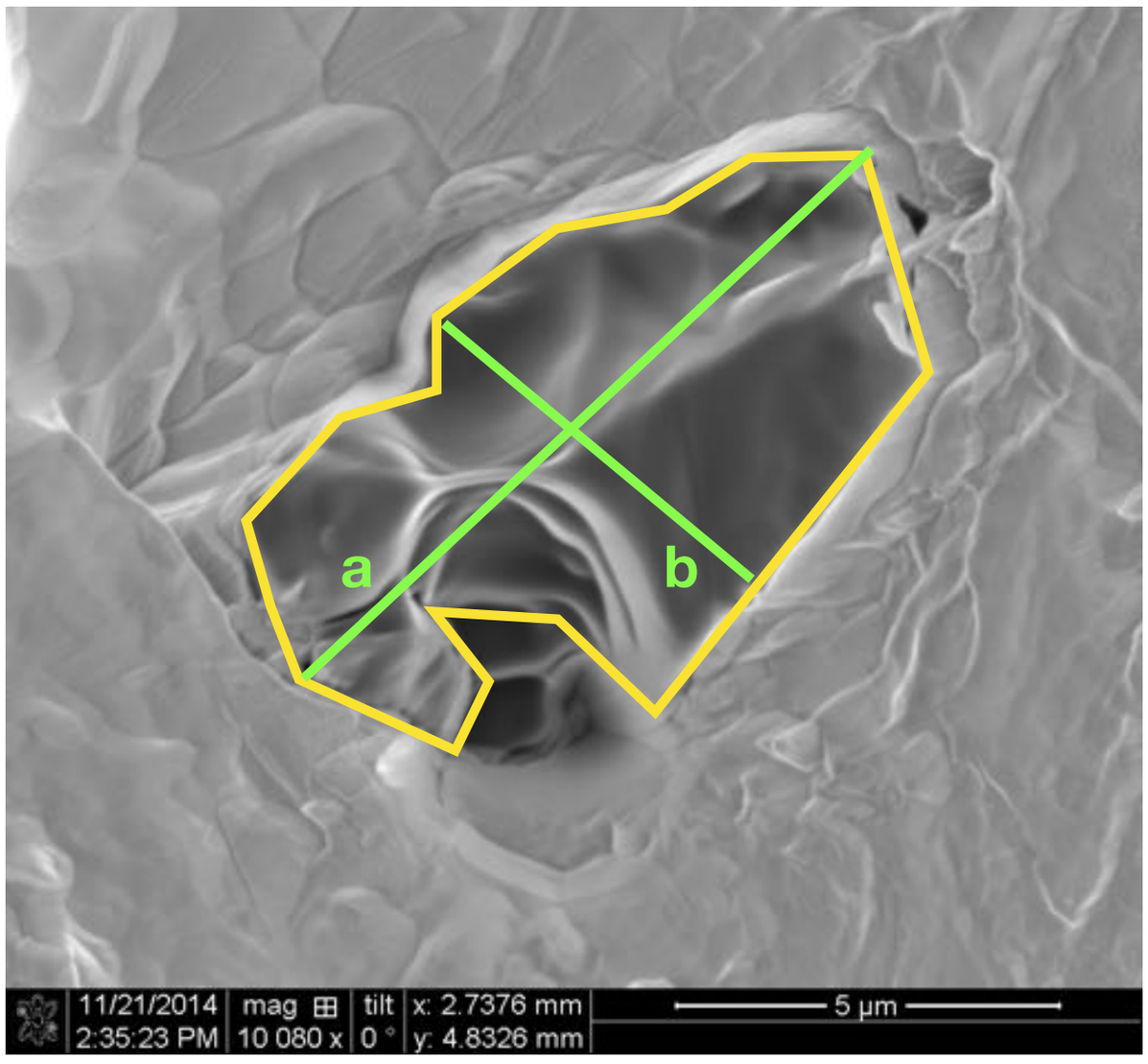

A = 40.6 μm^2
a=10.1 μm
b=5.7 μm
V=A×b=231 μm^3

ρ=~3.2 g cm^{-3}; (LS+LU fraction)
M=V×ρ=7.4E-10 g

L3-25

Before pressing into Au and before any SIMS analysis

a

b

A=41.5 μm²
a=7.5 μm
b=6.4 μm

SE

10.0kV x10k 5um

Before SHRIMP, after NanoSIMS

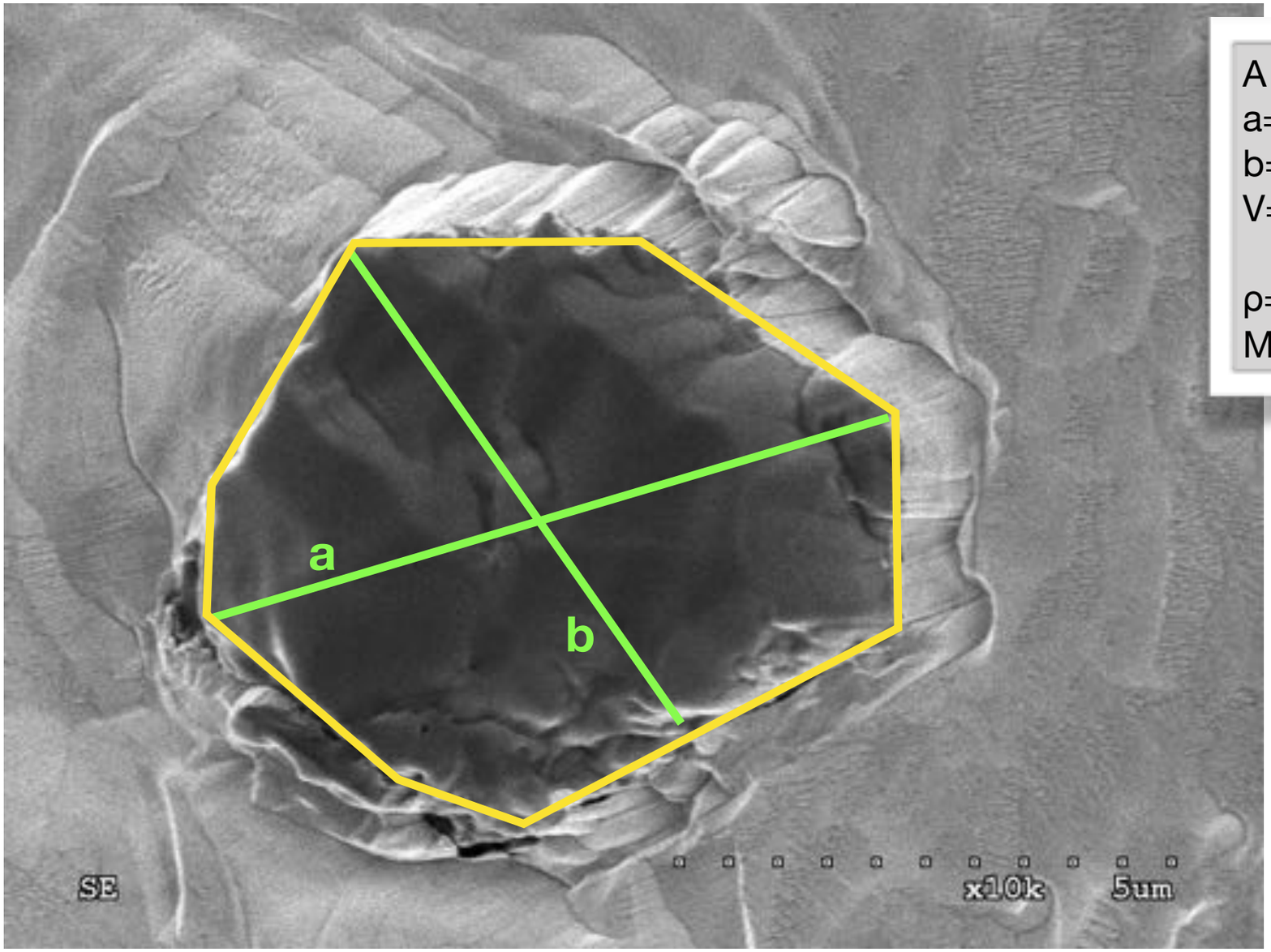

A = 30.917 μm^2
a=7.2 μm
b=5.9 μm
V=A×b=181 μm^3

ρ=~3.2 g cm^{-3}; (LS+LU fraction)
M=V×ρ=5.8E-10 g

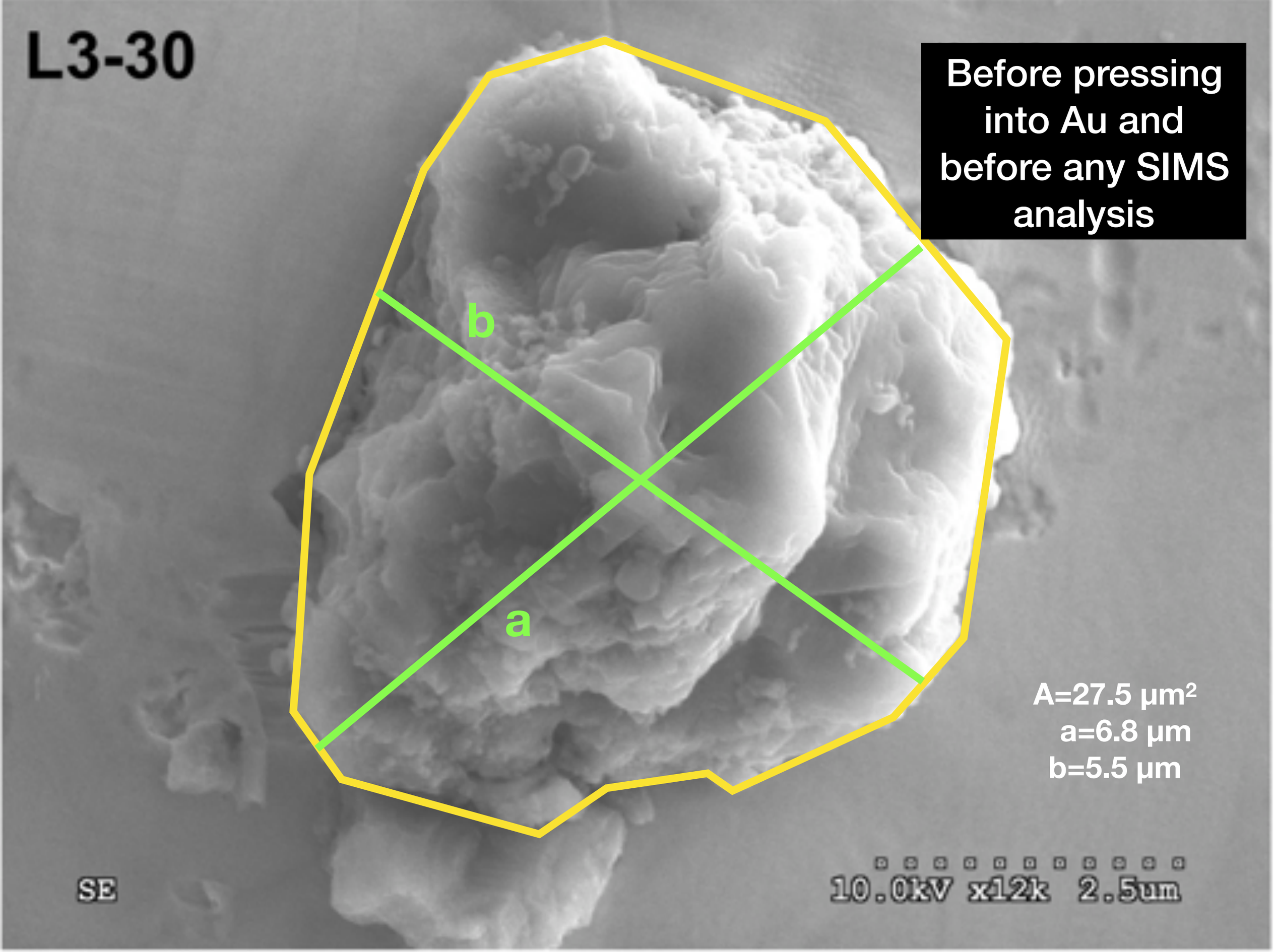
L3-30
Before pressing into Au and before any SIMS analysis
b
a
A=27.5 µm²
a=6.8 µm
b=5.5 µm
SE
10.0kV x12k 2.5um

Before SHRIMP, after NanoSIMS

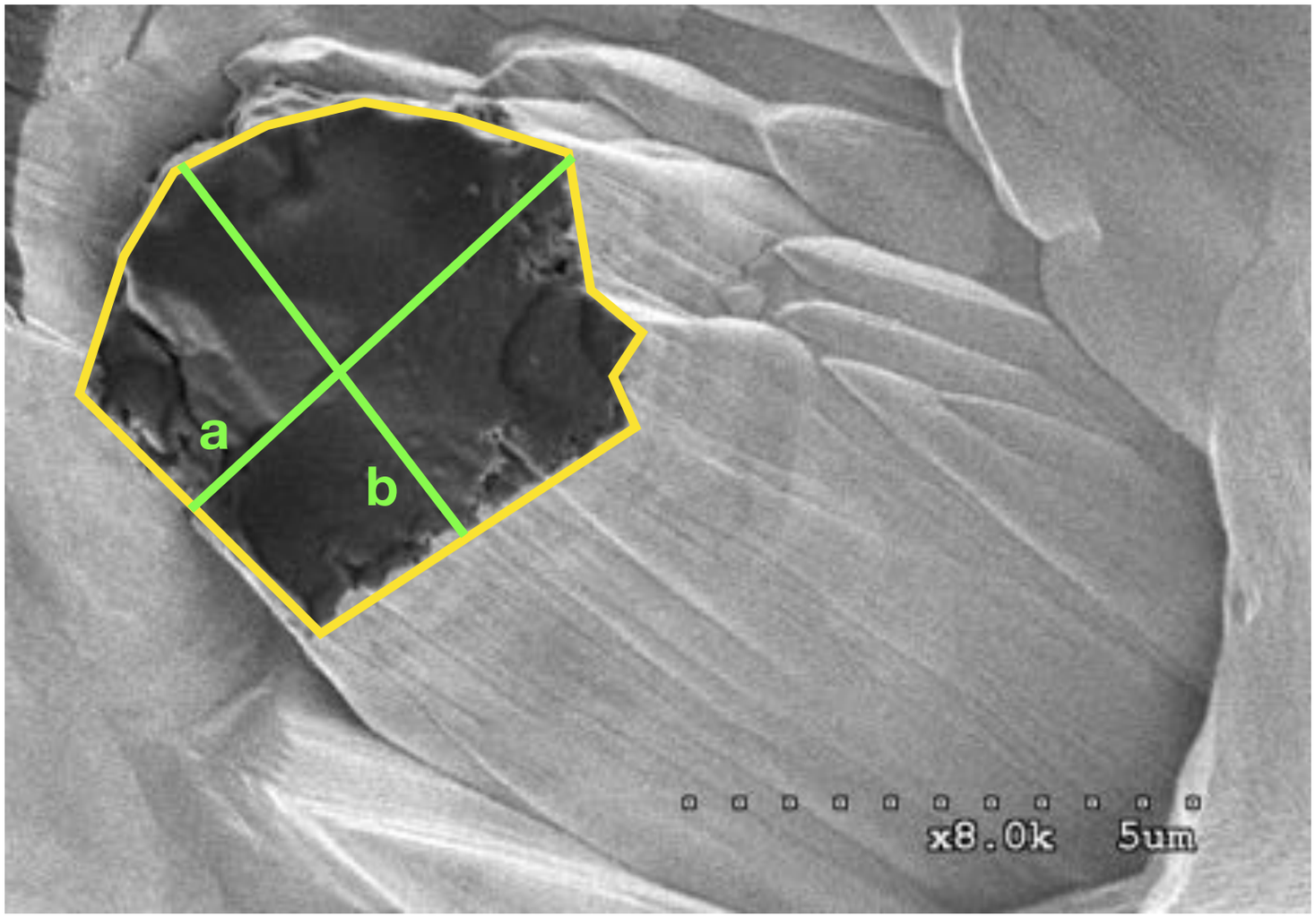

A = 22.6 μm^2
a=5.1 μm
b=4.5 μm
V=A×b=84.8 μm^3

ρ=~3.2 g cm^{-3}; (LS+LU fraction)
M=V×ρ=2.7E-10 g

L3-31

Before any SIMS analysis

$^{12}C/^{13}C = 42.1$

$^{14}N/^{15}N = 675$

$\delta^{29}Si/^{28}Si = 171$

$\delta^{30}Si/^{28}Si = 142$

a

b

A=24.5 µm²

a=5.8 µm

b=5.2 µm

SE

10.0kV x15k 2um

Before SHRIMP, after NanoSIMS

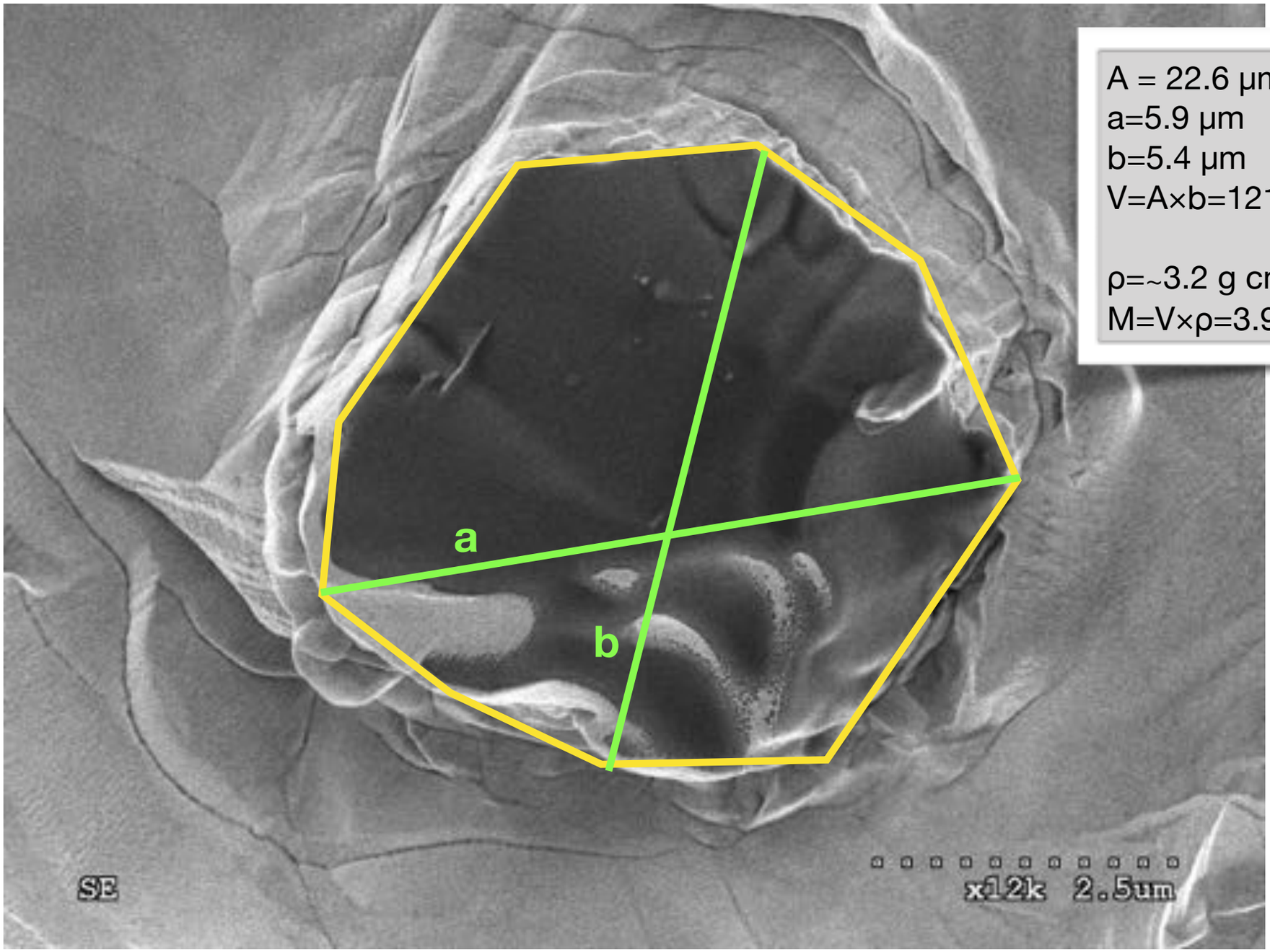

A = 22.6 μm^2
a=5.9 μm
b=5.4 μm
V=A×b=121 μm^3

ρ=~3.2 g cm^{-3}; (LS+LU fraction)
M=V×ρ=3.9E-10 g

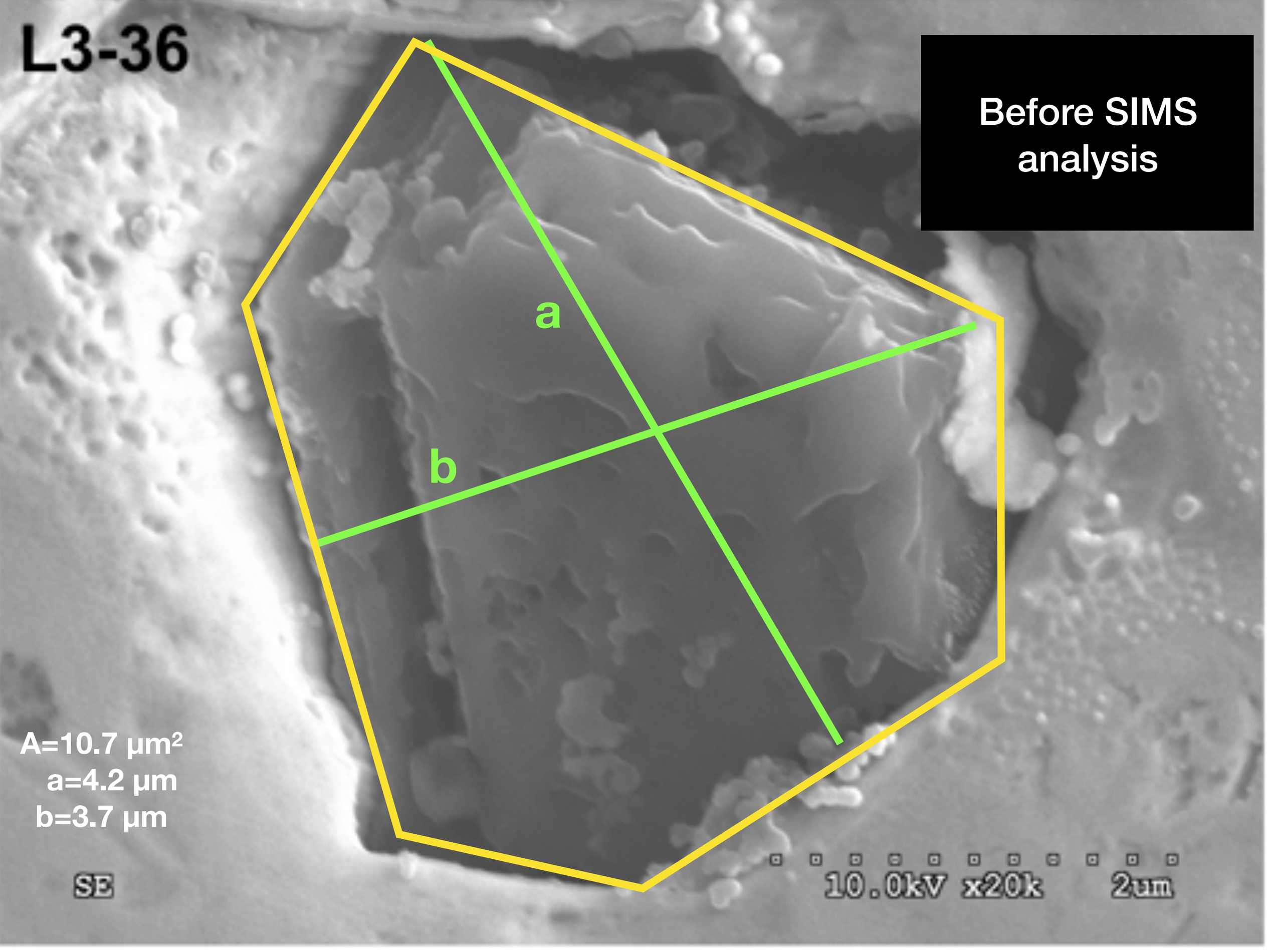
L3-36
Before SIMS analysis
a
b
A=10.7 µm²
a=4.2 µm
b=3.7 µm
SE
10.0kV x20k
2µm

Before SHRIMP, after NanoSIMS

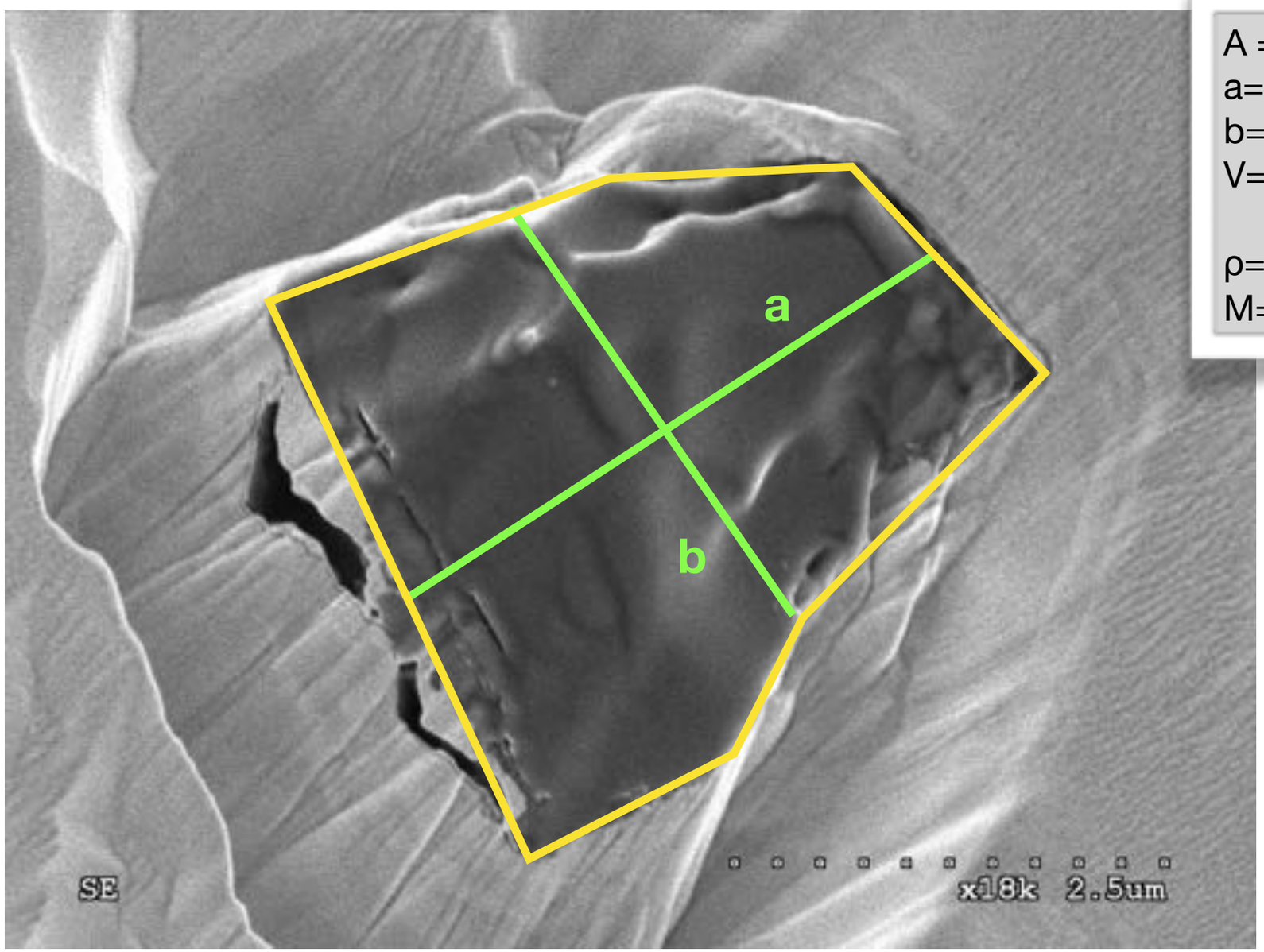

A = 9.9 μm^2
a=3.8 μm
b=2.8 μm
V=A×b=27 μm^3

ρ=~3.2 g cm^{-3}; (LS+LU fraction)
M=V×ρ=8.8E-11 g

L3-37

Before pressing into Au and before any SIMS analysis

b

a

A=10.6 μm²
a=4.1 μm
b=3.3 μm

SE

10.0kV x20k 2um

Before SHRIMP, after NanoSIMS

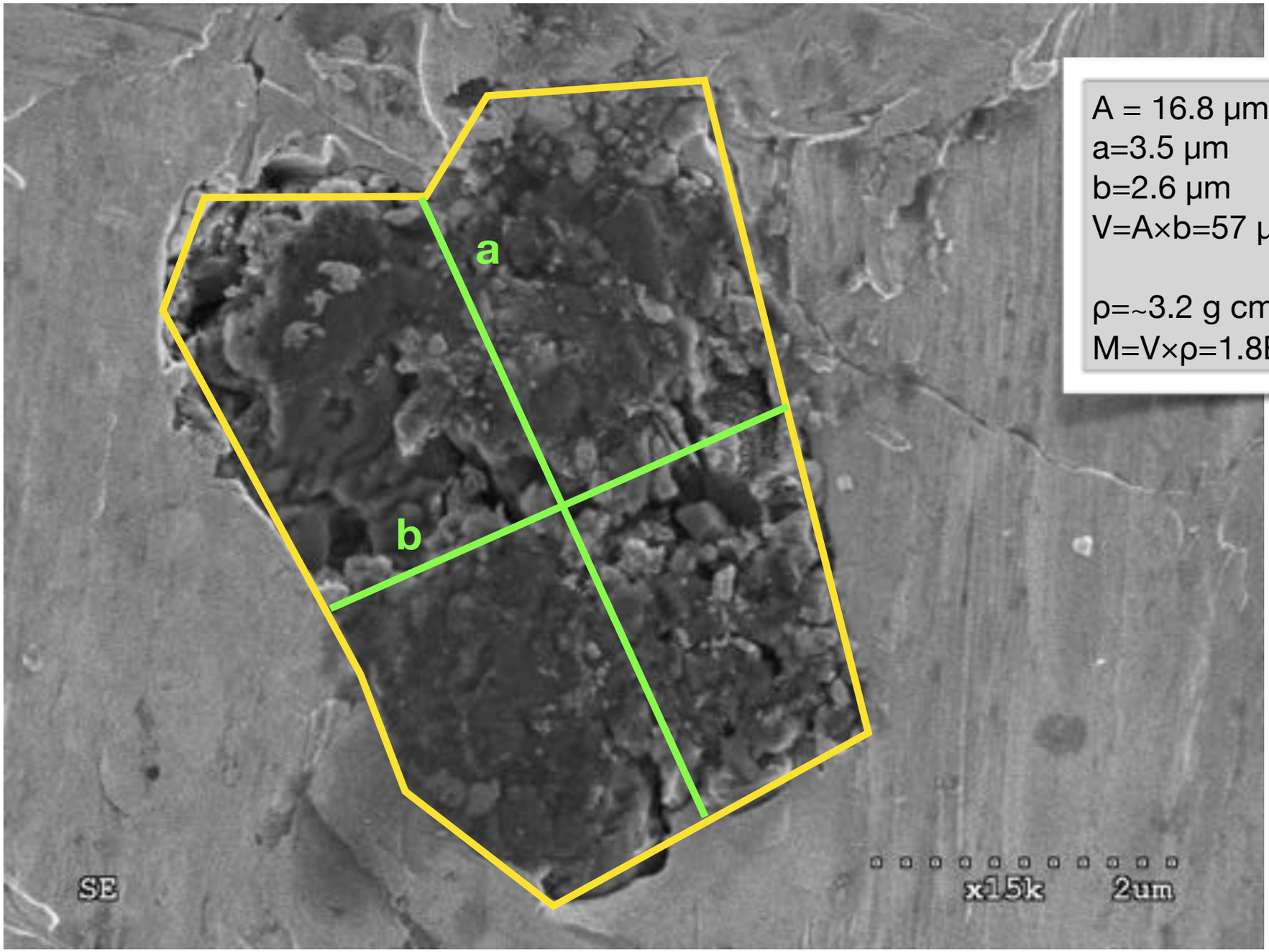

A = 16.8 μm^2
a=3.5 μm
b=2.6 μm
V=A×b=57 μm^3

ρ=~3.2 g cm^{-3}; (LS+LU fraction)
M=V×ρ=1.8E-10 g

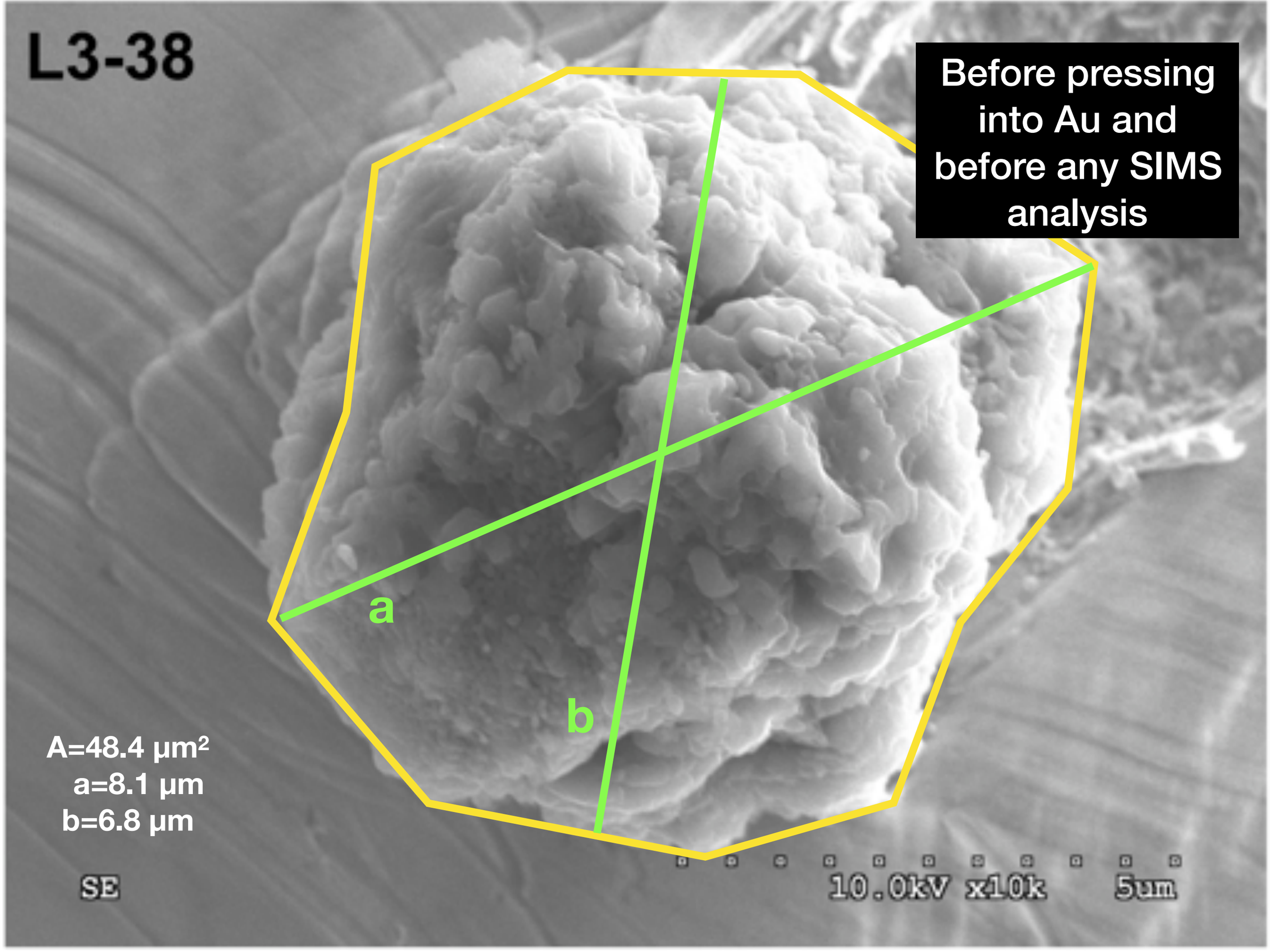
L3-38
Before pressing into Au and before any SIMS analysis
a
b
A=48.4 µm²
a=8.1 µm
b=6.8 µm
SE
10.0kV x10k
5um

Before SHRIMP, after NanoSIMS

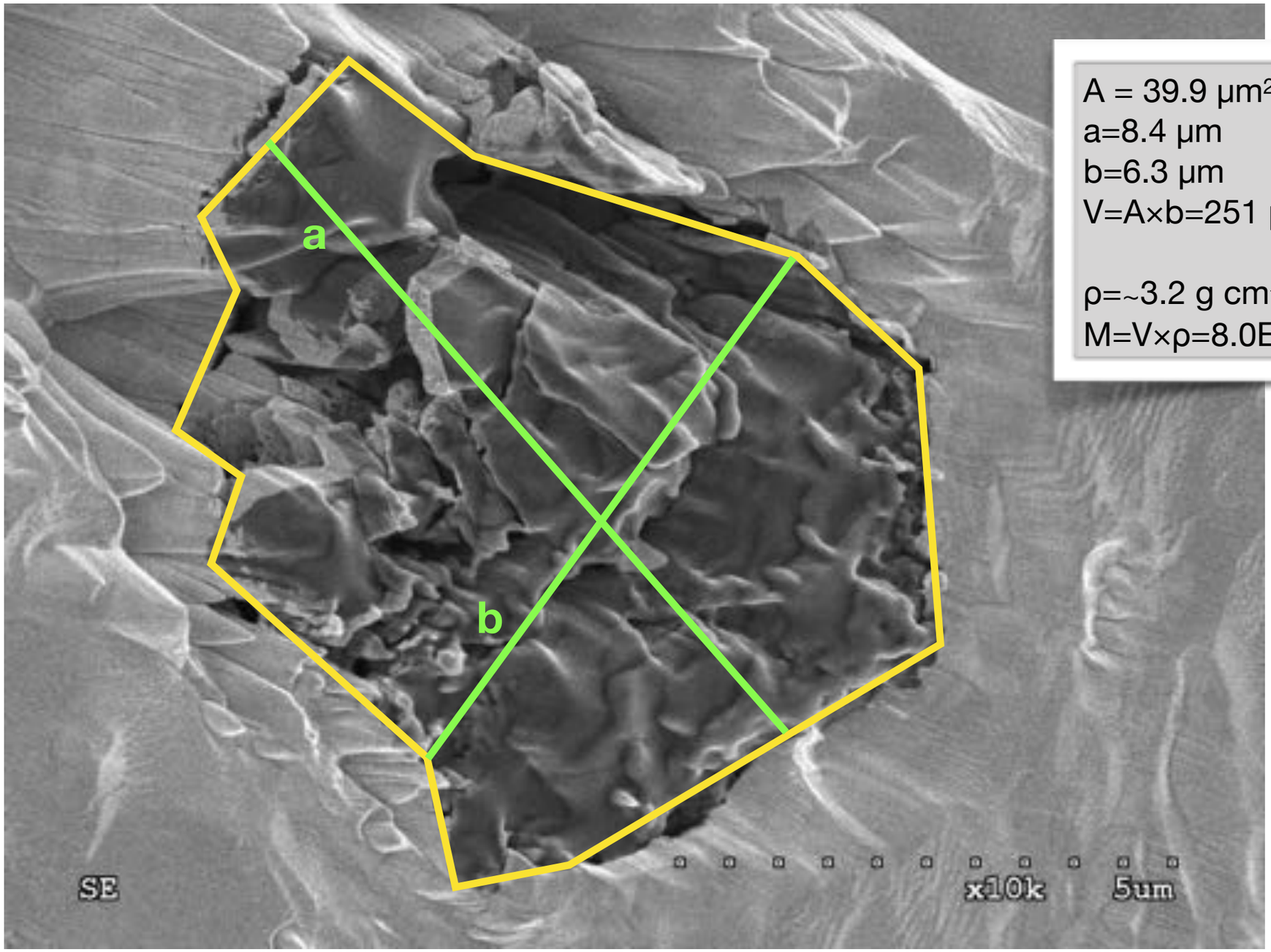

A = 39.9 μm^2
a=8.4 μm
b=6.3 μm
V=A×b=251 μm^3

ρ=~3.2 g cm^{-3}; (LS+LU fraction)
M=V×ρ=8.0E-10 g

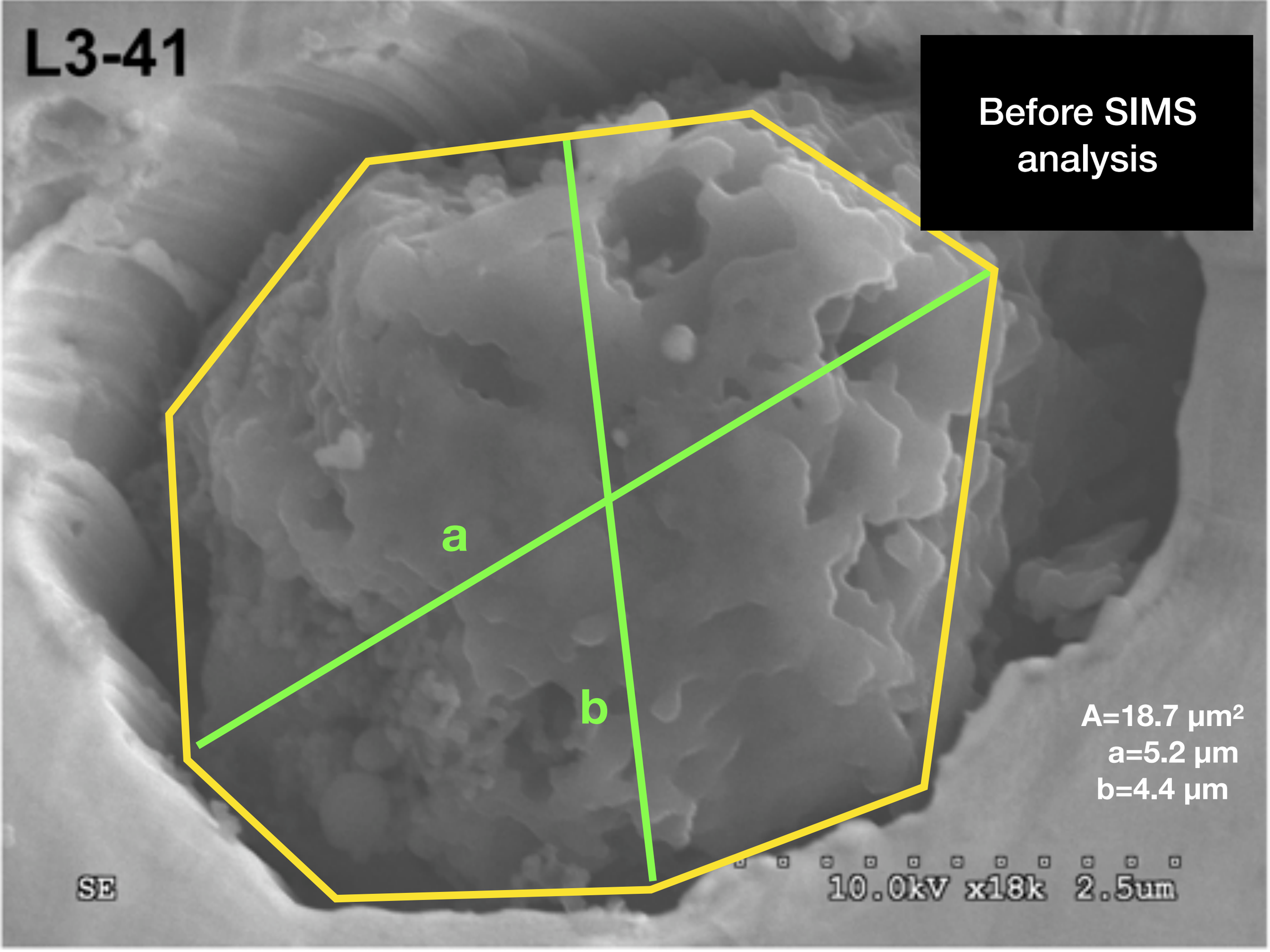
L3-41
Before SIMS analysis
a
b
A=18.7 μm²
a=5.2 μm
b=4.4 μm
SE
10.0kV x18k 2.5um

Before SHRIMP, after NanoSIMS

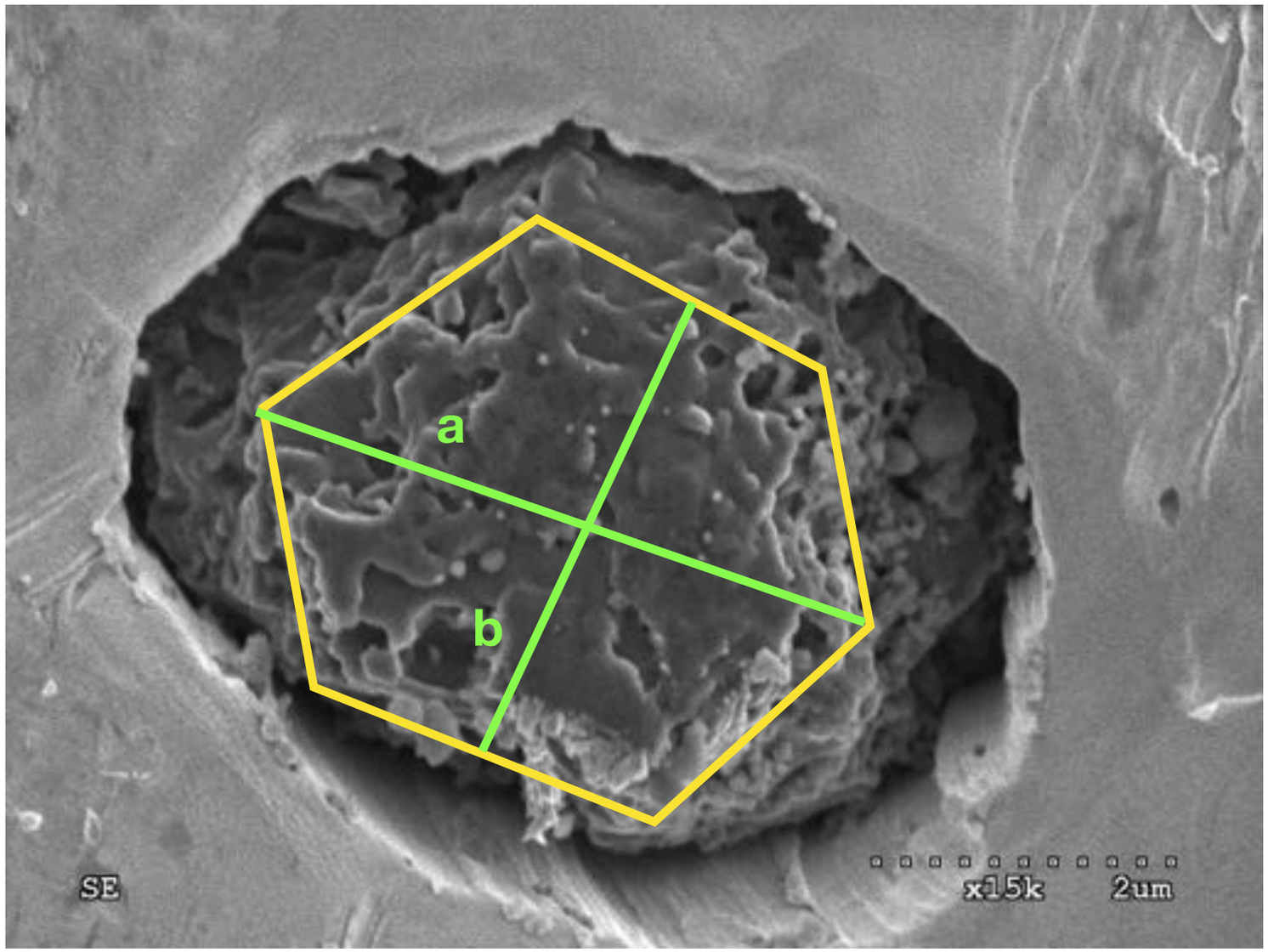

A = 11.3 μm^2
a=4.2 μm
b=3.2 μm
V=A×b=36 μm^3

ρ=~3.2 g cm^{-3}; (LS+LU fraction)
M=V×ρ=1.2E-10 g

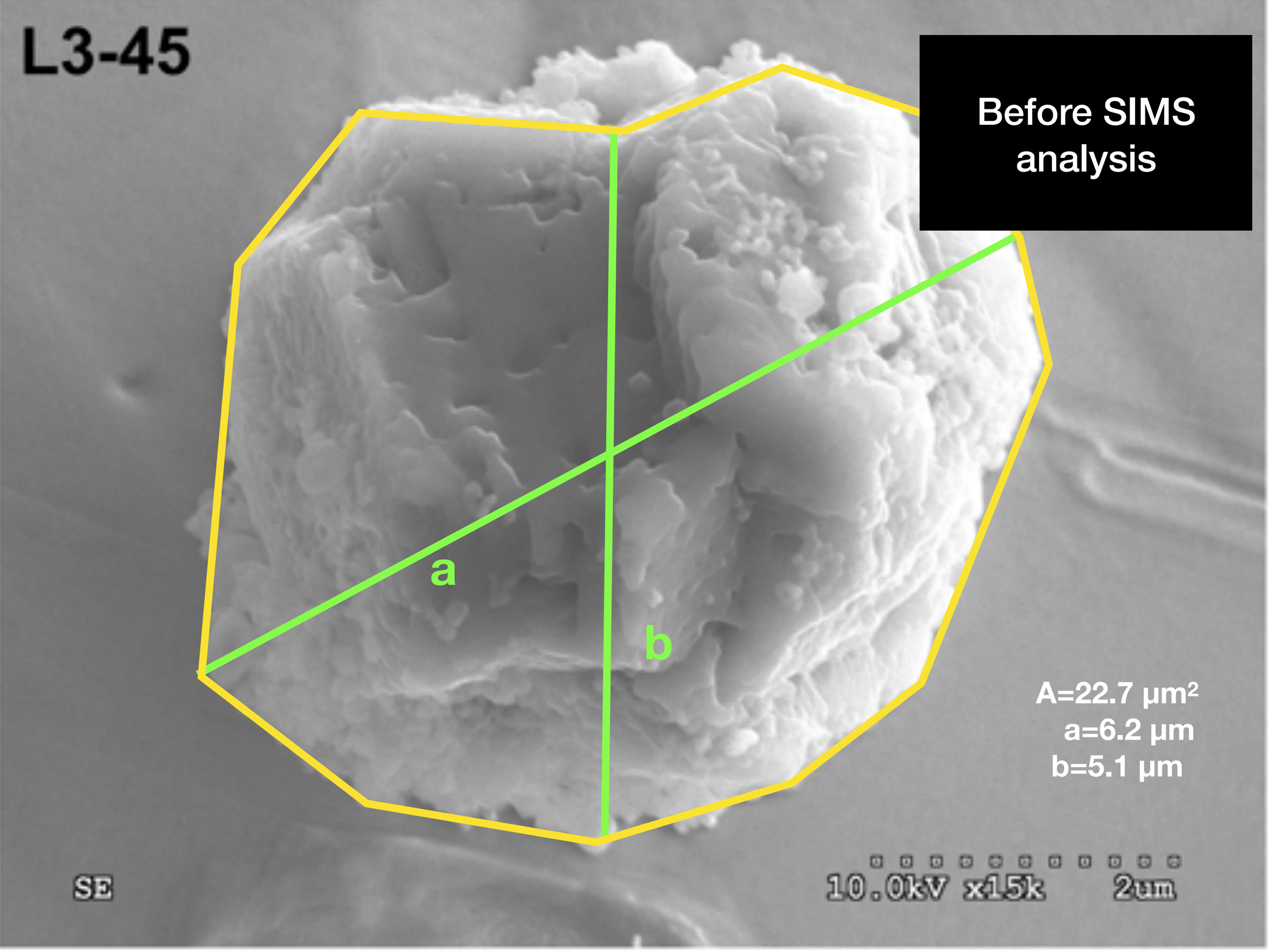
L3-45
Before SIMS analysis
a
b
A=22.7 µm²
a=6.2 µm
b=5.1 µm
SE
10.0kV x15k 2um

Before SHRIMP, after NanoSIMS

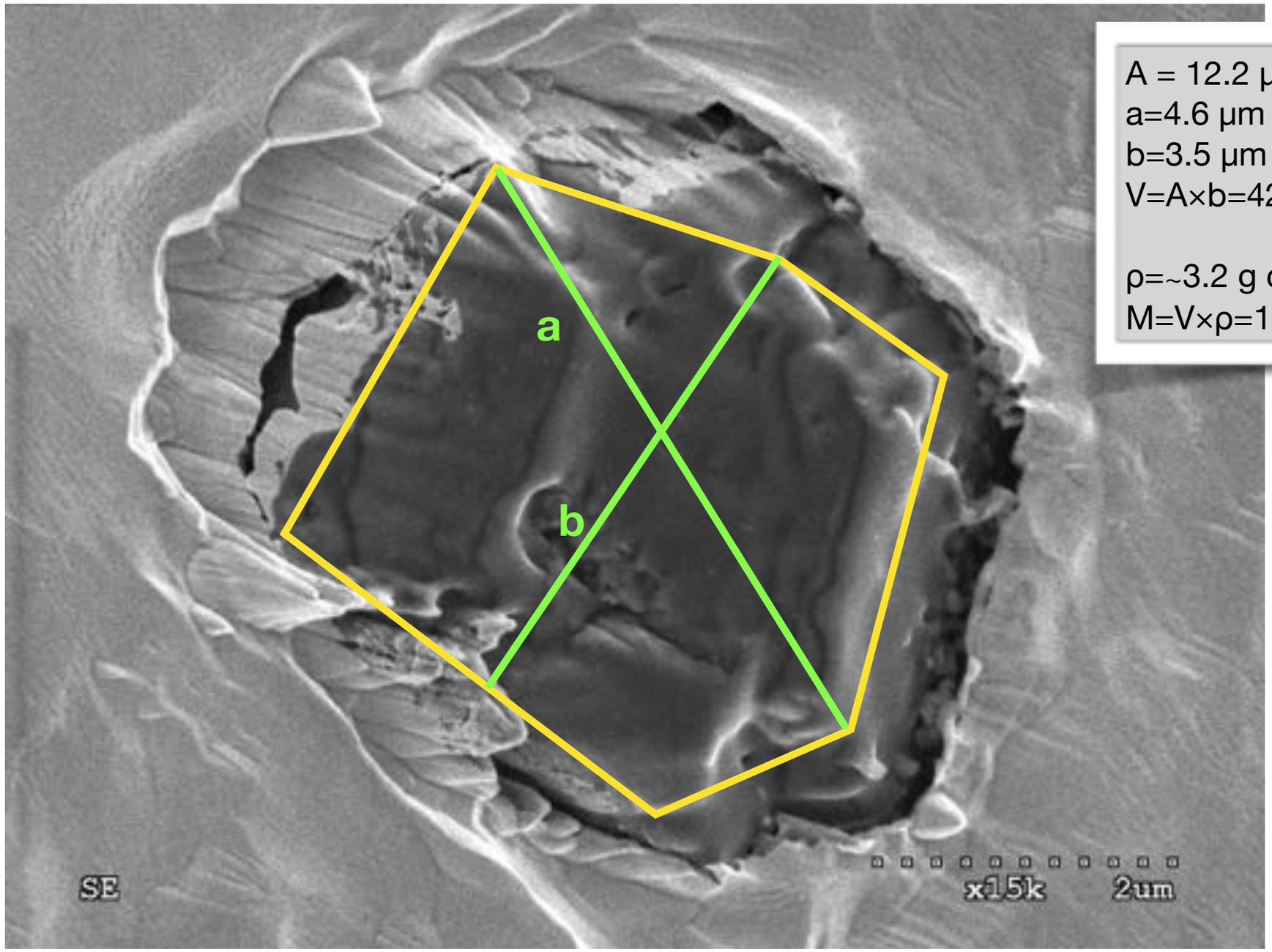

A = 12.2 μm^2
a=4.6 μm
b=3.5 μm
V=A×b=42 μm^3

ρ=~3.2 g cm^{-3}; (LS+LU fraction)
M=V×ρ=1.4E-10 g

L3-46

Before pressing into Au and before any SIMS analysis

b

a

A=13.2 μm²
a=4.8 μm
b=4.2 μm

SE

10.0kV x15k 2um

Before SHRIMP, after NanoSIMS

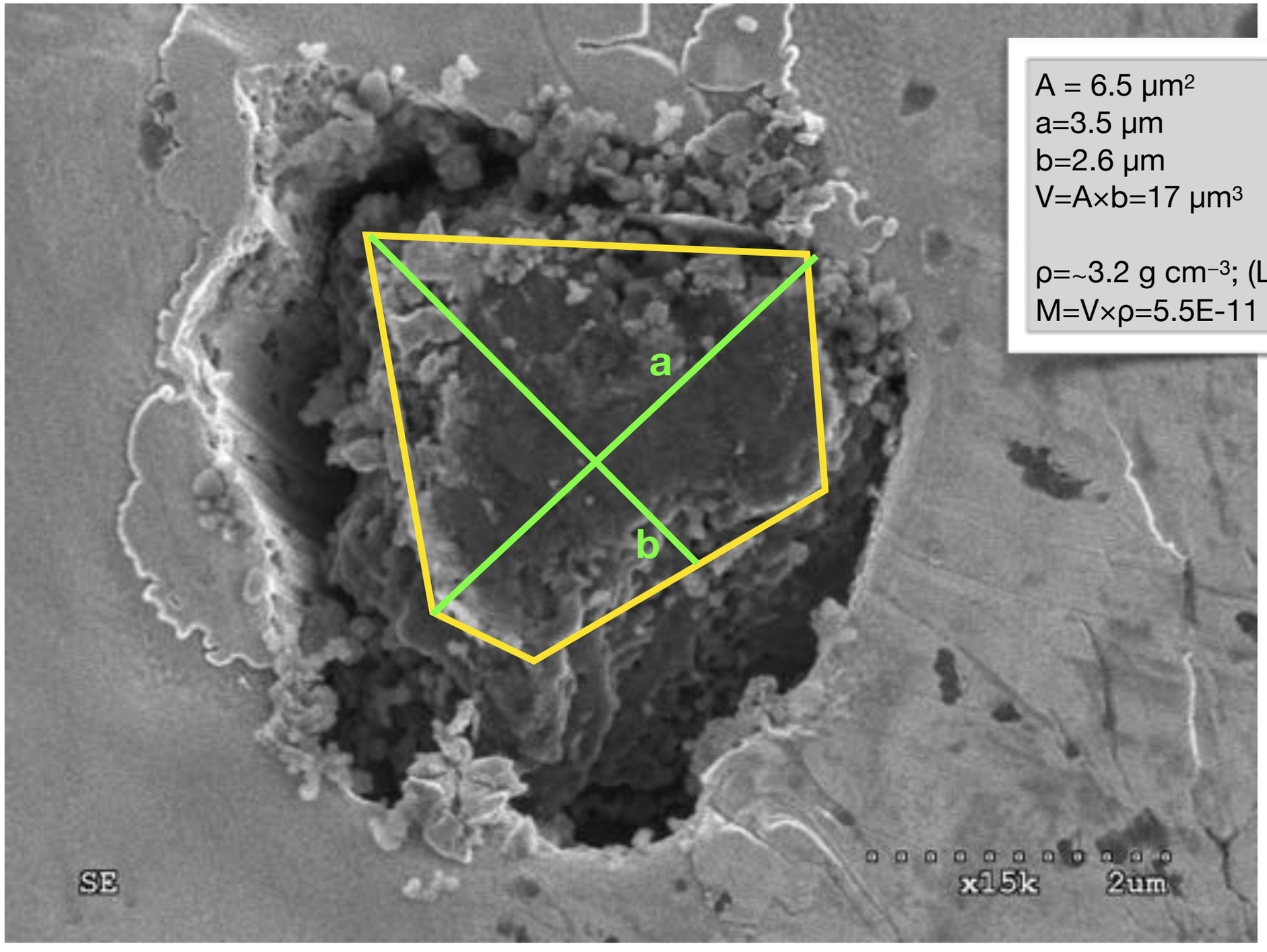

A = 6.5 μm²
a=3.5 μm
b=2.6 μm
V=A×b=17 μm³

ρ=~3.2 g cm⁻³; (LS+LU fraction)
M=V×ρ=5.5E-11 g

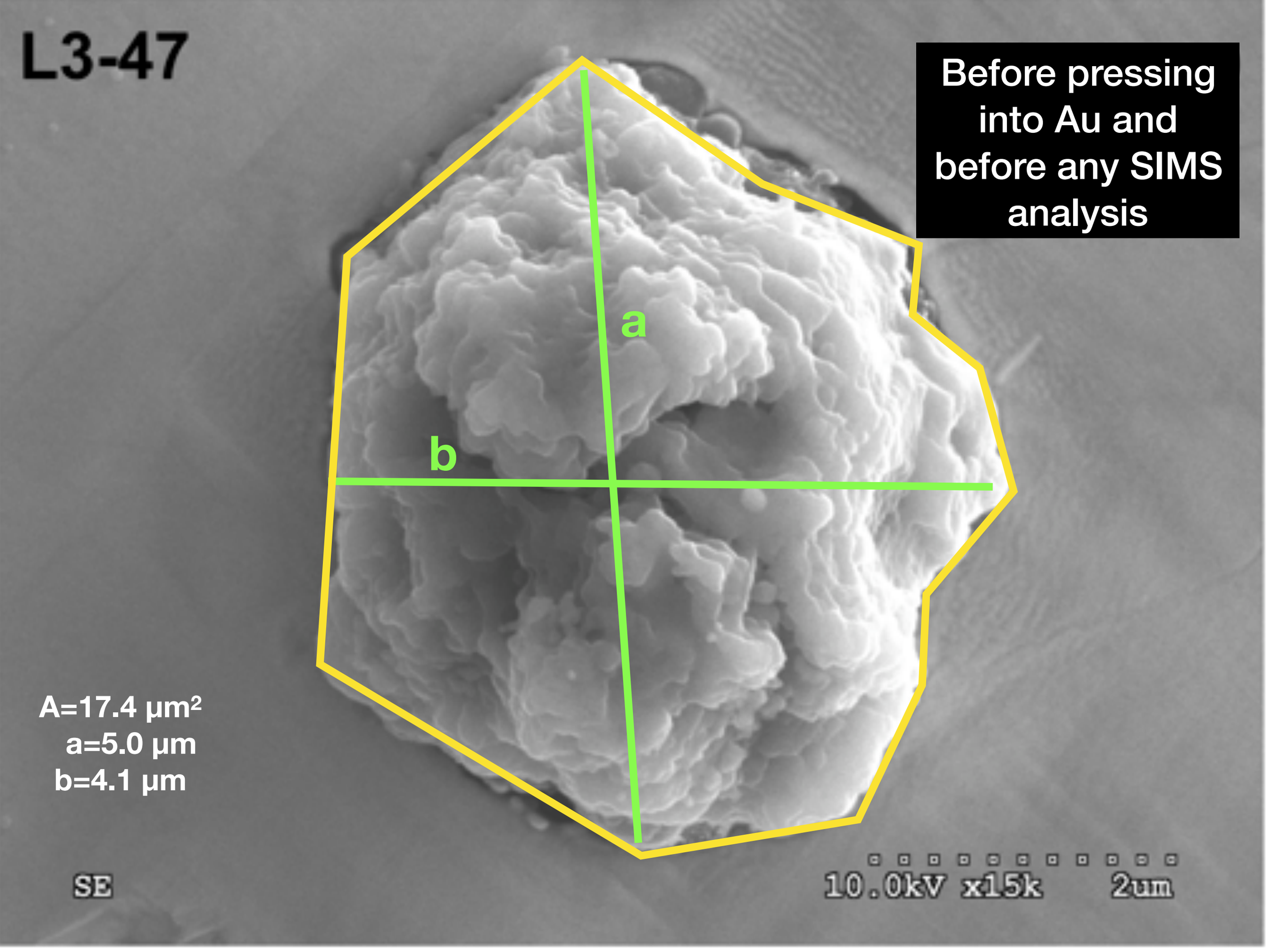
L3-47
Before pressing into Au and before any SIMS analysis
a
b
A=17.4 μm²
a=5.0 μm
b=4.1 μm
SE
10.0kV x15k
2um

L3_47

Before SHRIMP, after NanoSIMS

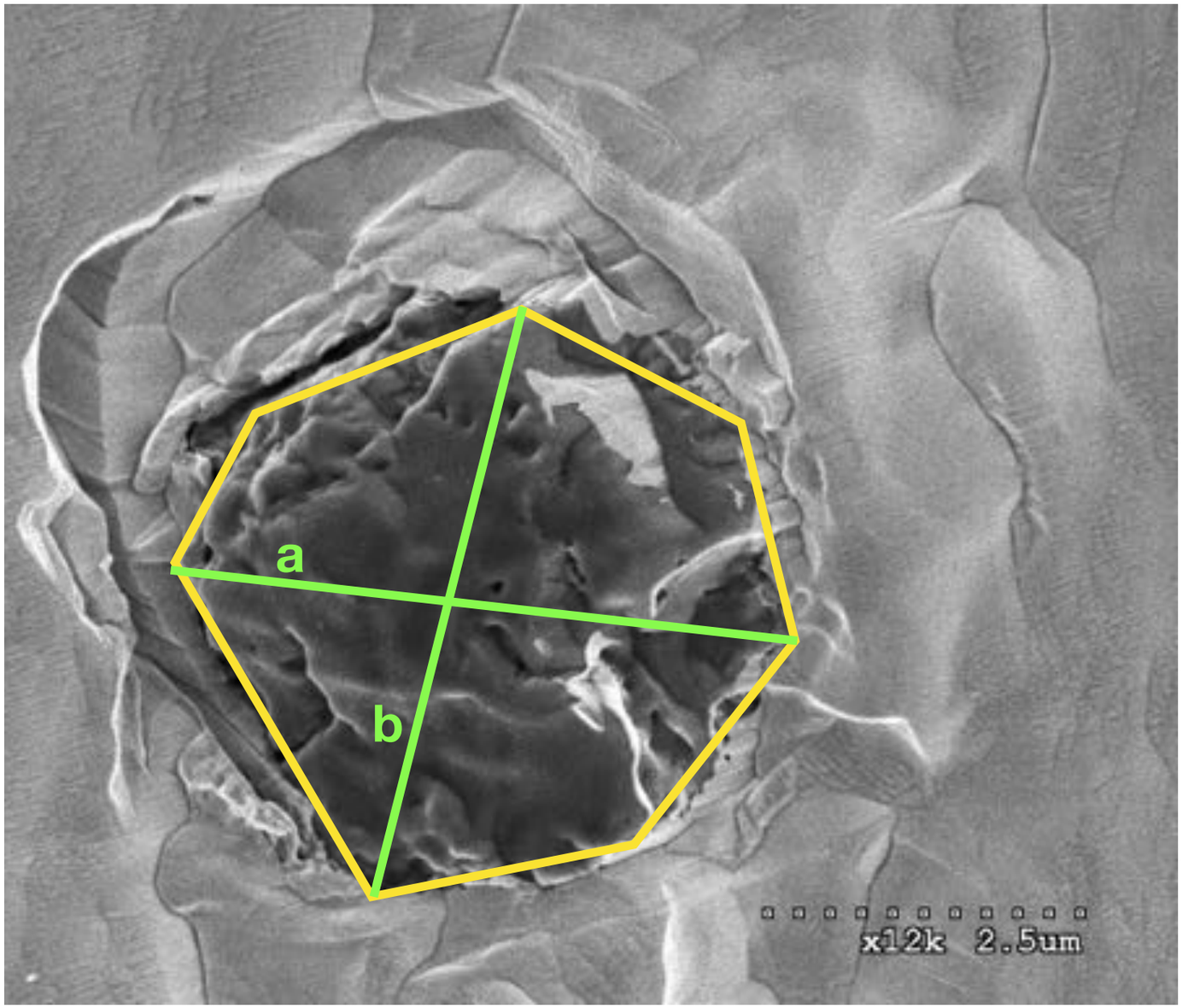

A = 15.8 μm²
a=4.9 μm
b=4.5 μm
V=A×b=70 μm³

ρ=~3.2 g cm⁻³; (LS+LU fraction)
M=V×ρ=2.3E-10 g

Before laser, after SIMS

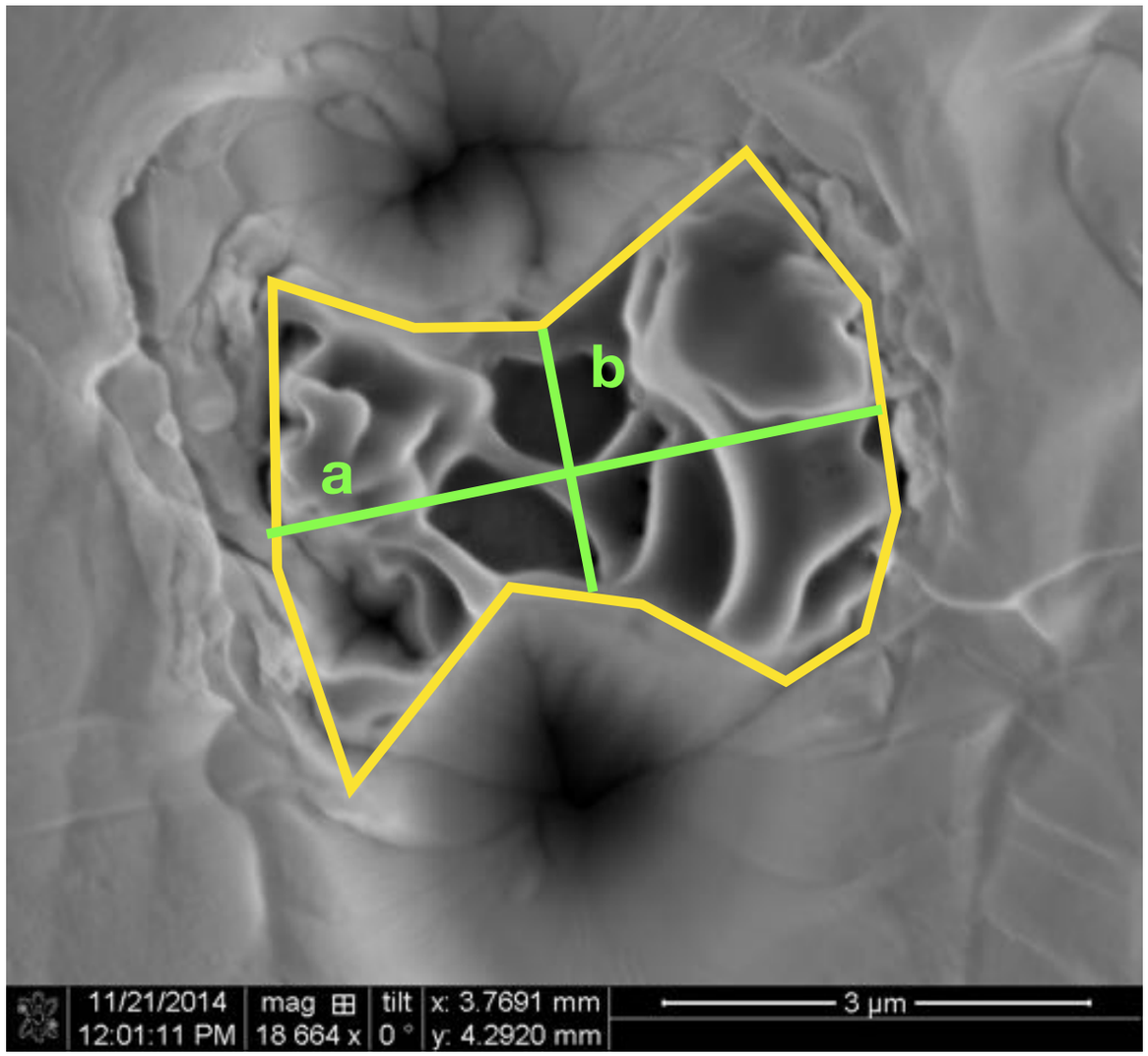

A = 11.3 μm²
a=4.4 μm
b=1.8 μm
V=A×b=21 μm³

ρ=~3.2 g cm⁻³; (LS+LU fraction)
M=V×ρ=6.6E-11 g

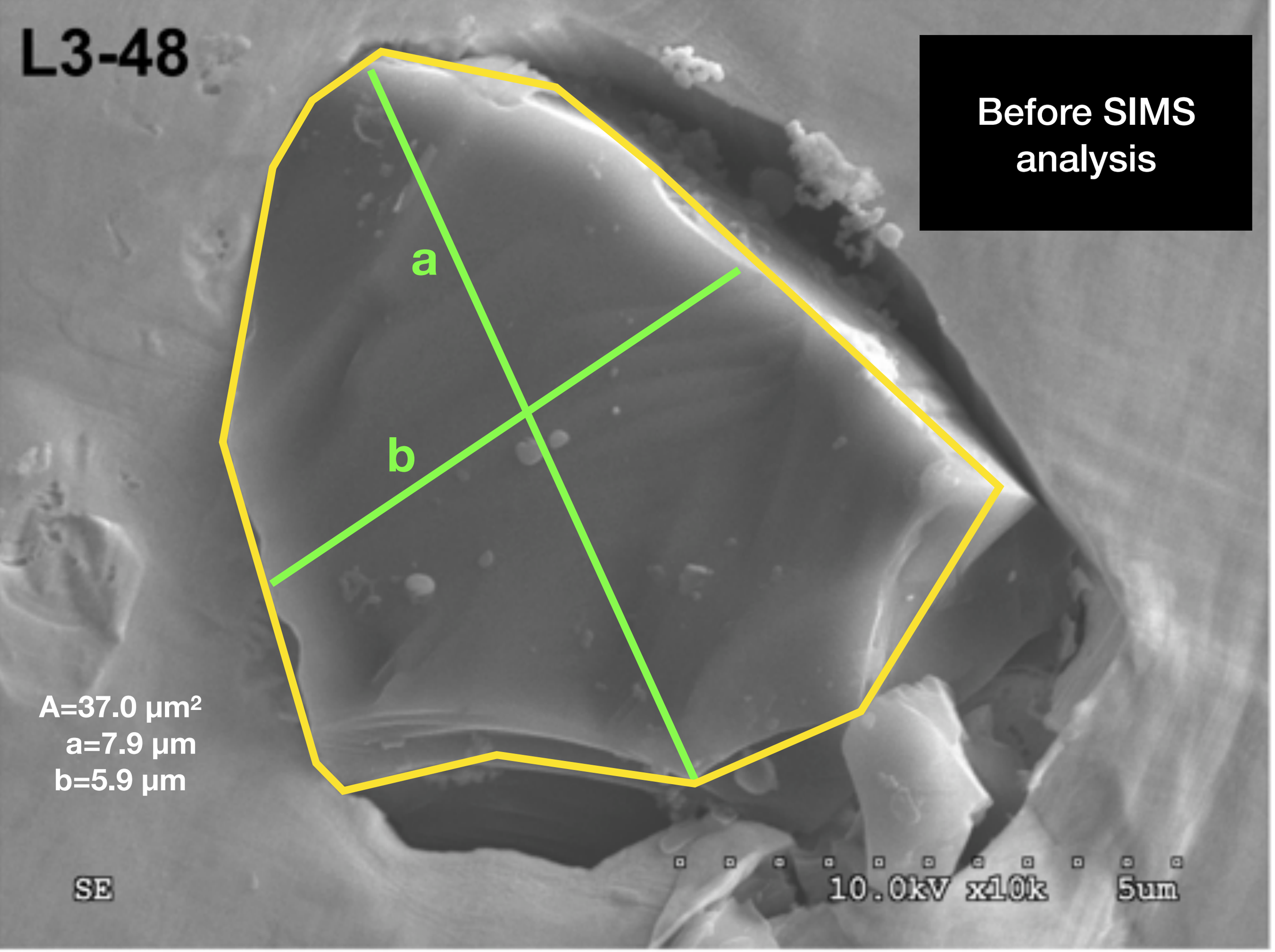
L3-48
Before SIMS analysis
a
b
A=37.0 μm²
a=7.9 μm
b=5.9 μm
SE
10.0kV x10k
5um

Before SHRIMP, after NanoSIMS

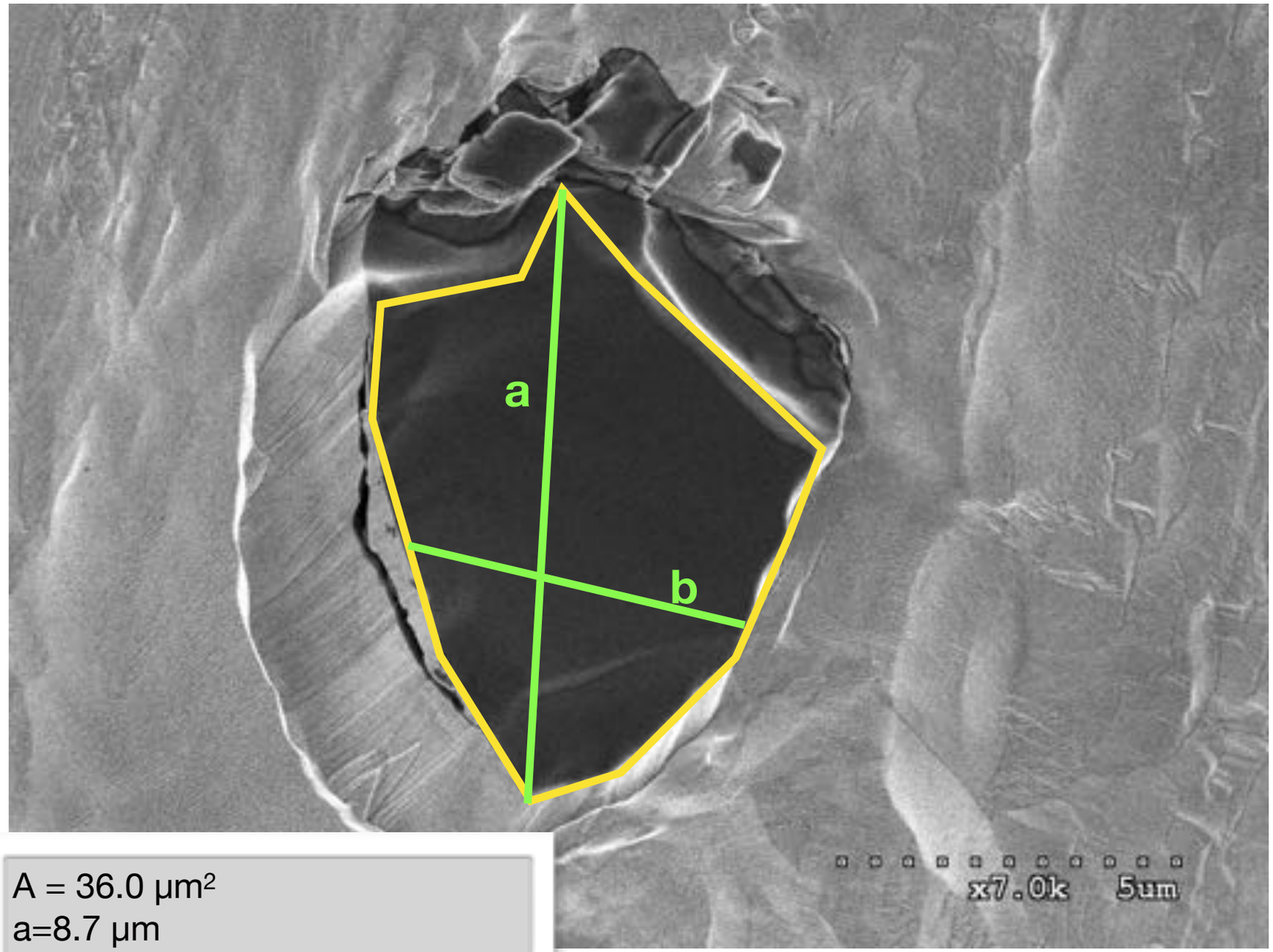

A = 36.0 μm^2
a=8.7 μm
b=5.1 μm
V=A×b=185 μm^3

ρ=~3.2 g cm^{-3}; (LS+LU fraction)
M=V×ρ=5.9E-10 g

L3-49

Before SIMS analysis

a

b

A=18.9 μm²
a=5.8 μm
b=5.0 μm

SE

10.0kV x15k 2um

Before SHRIMP, after NanoSIMS

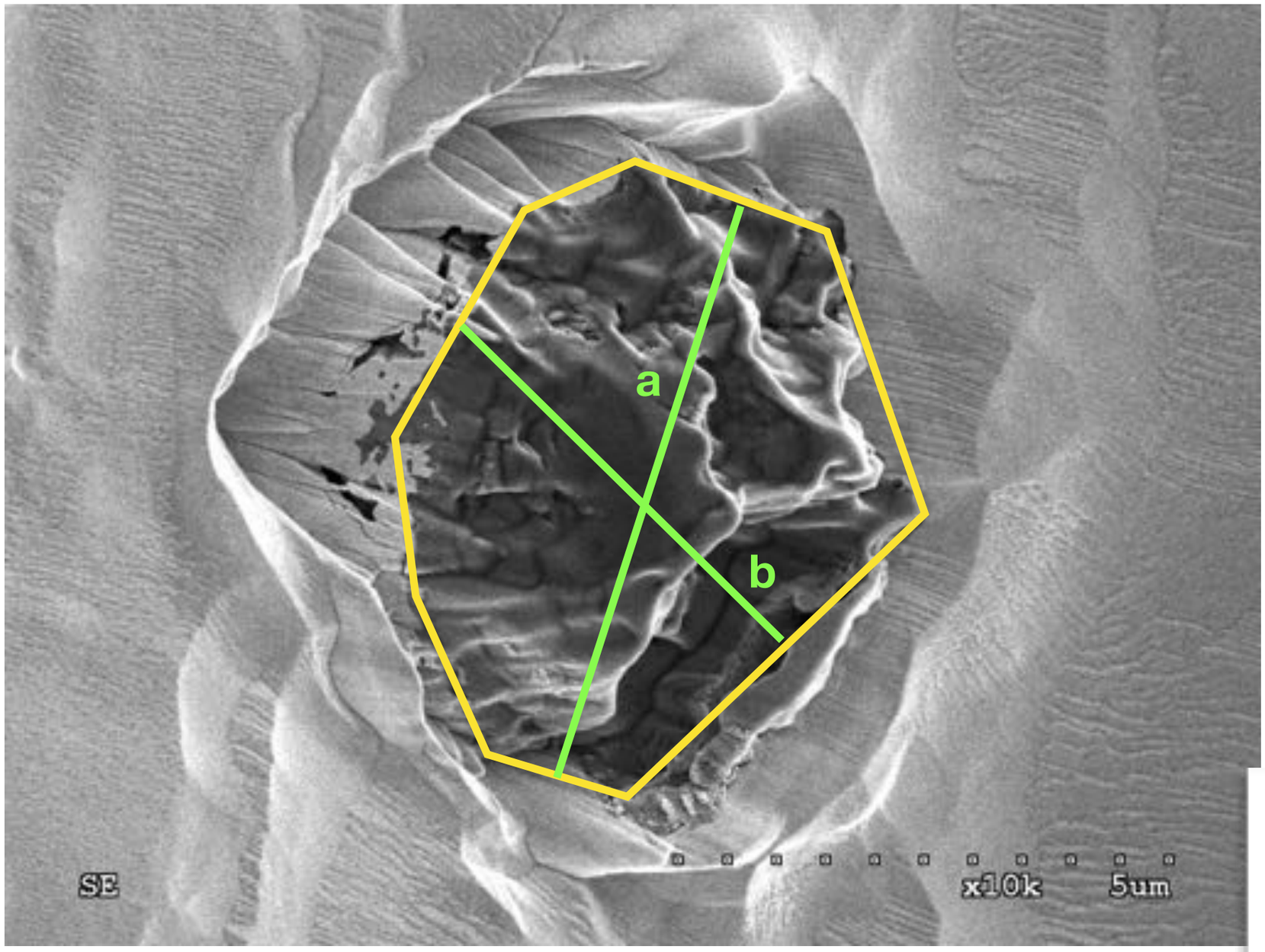

A = 23.0 μm^2
a=5.9 μm
b=5.0 μm
V=A×b=113 μm^3

ρ=~3.2 g cm^{-3}; (LS+LU fraction)
M=V×ρ=3.6E-10 g

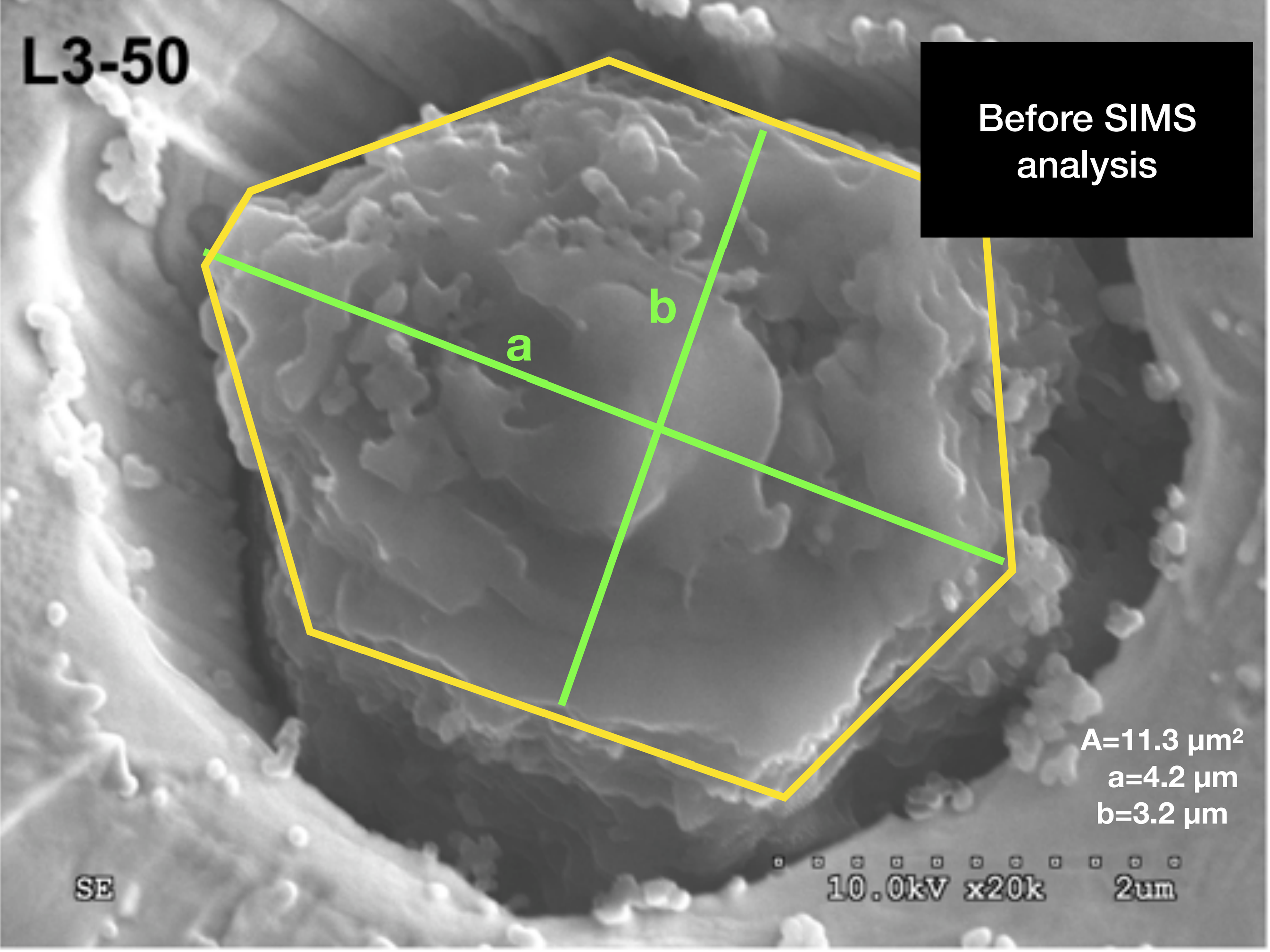
L3-50
Before SIMS analysis
a
b
A=11.3 μm²
a=4.2 μm
b=3.2 μm
SE
10.0kV x20k
2um

L3_50

Before SHRIMP, after NanoSIMS

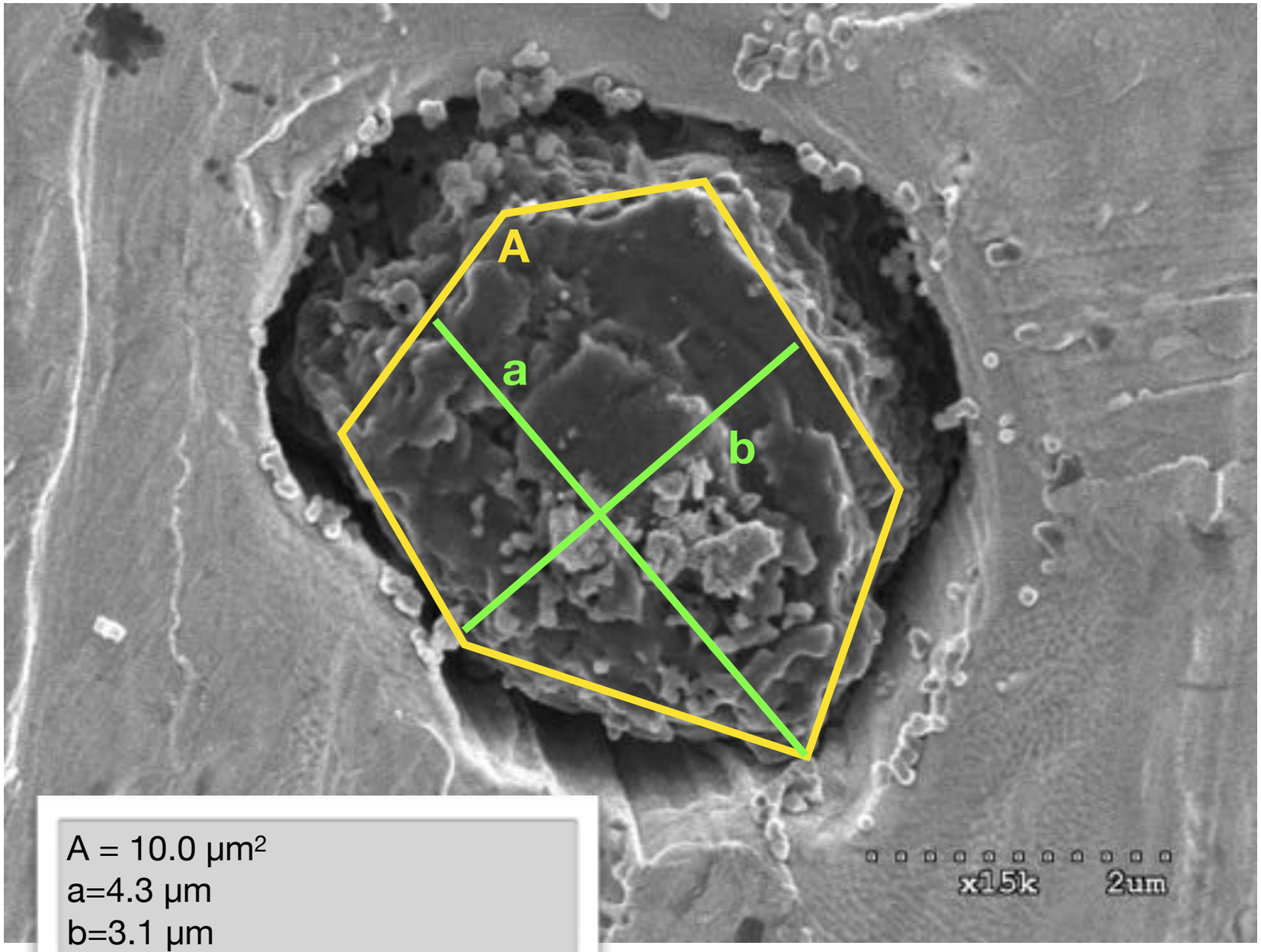

A = 10.0 μm^2
a=4.3 μm
b=3.1 μm
V=A×b=31.2 μm^3

ρ=~3.2 g cm^{-3}; (LS+LU fraction)
M=V×ρ=1.0E-10 g

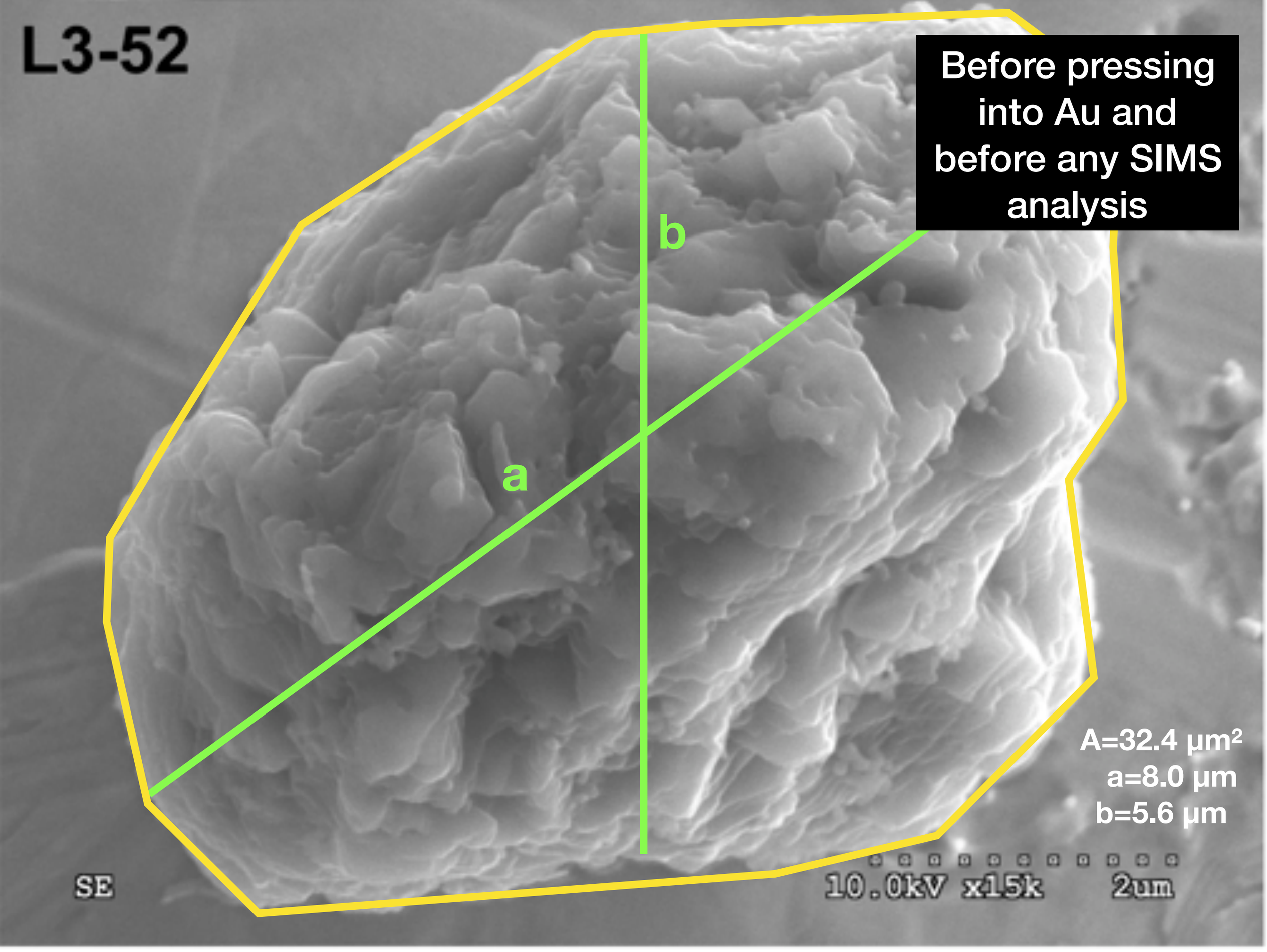
L3-52
Before pressing into Au and before any SIMS analysis
b
a
A=32.4 µm²
a=8.0 µm
b=5.6 µm
SE
10.0kV x15k
2um

Before SHRIMP, after NanoSIMS

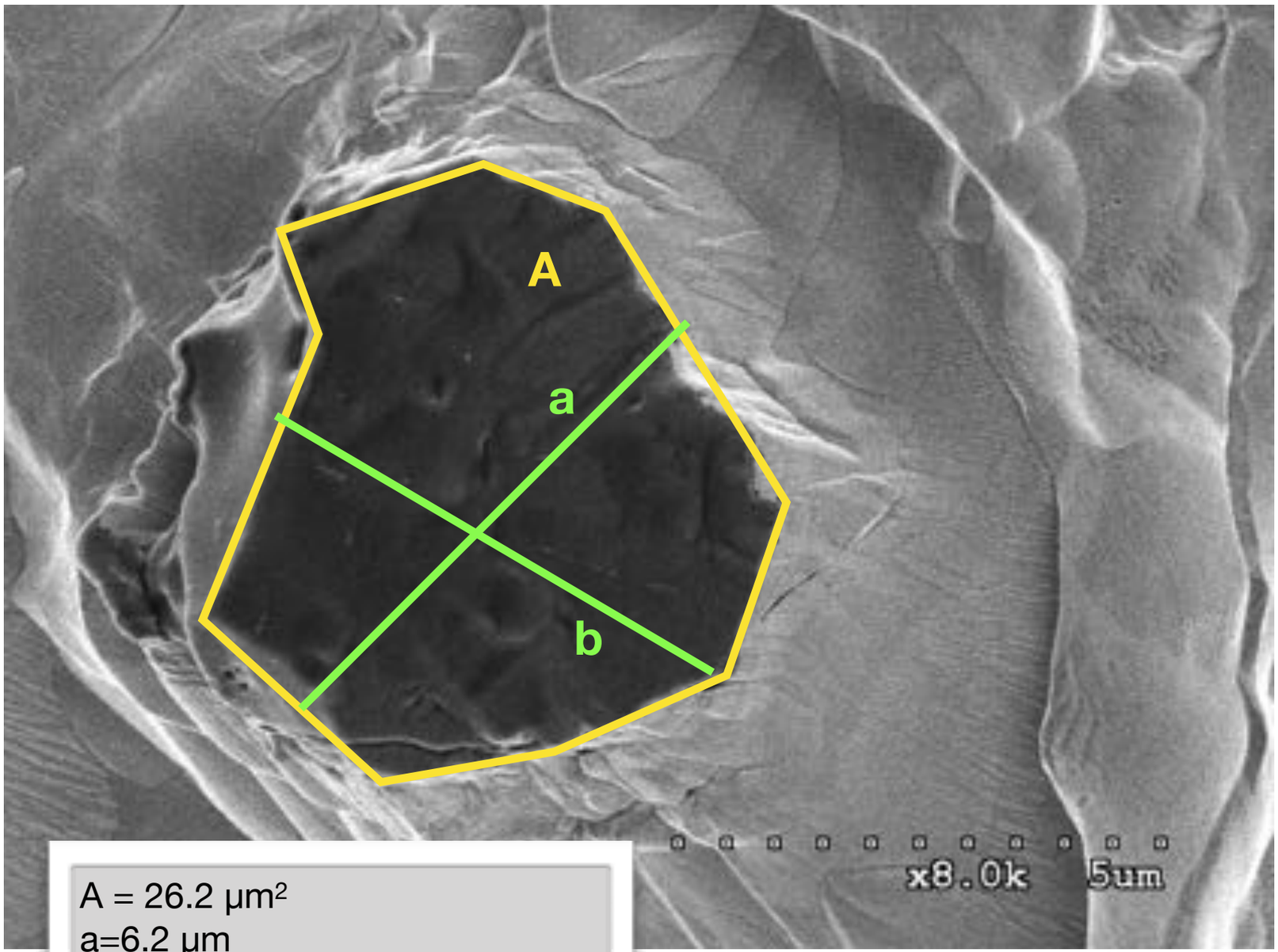

A = 26.2 μm^2
a=6.2 μm
b=5.0 μm
V=A×b=130.9 μm^3

ρ=~3.2 g cm^{-3}; (LS+LU fraction)
M=V×ρ=4.2E-10 g

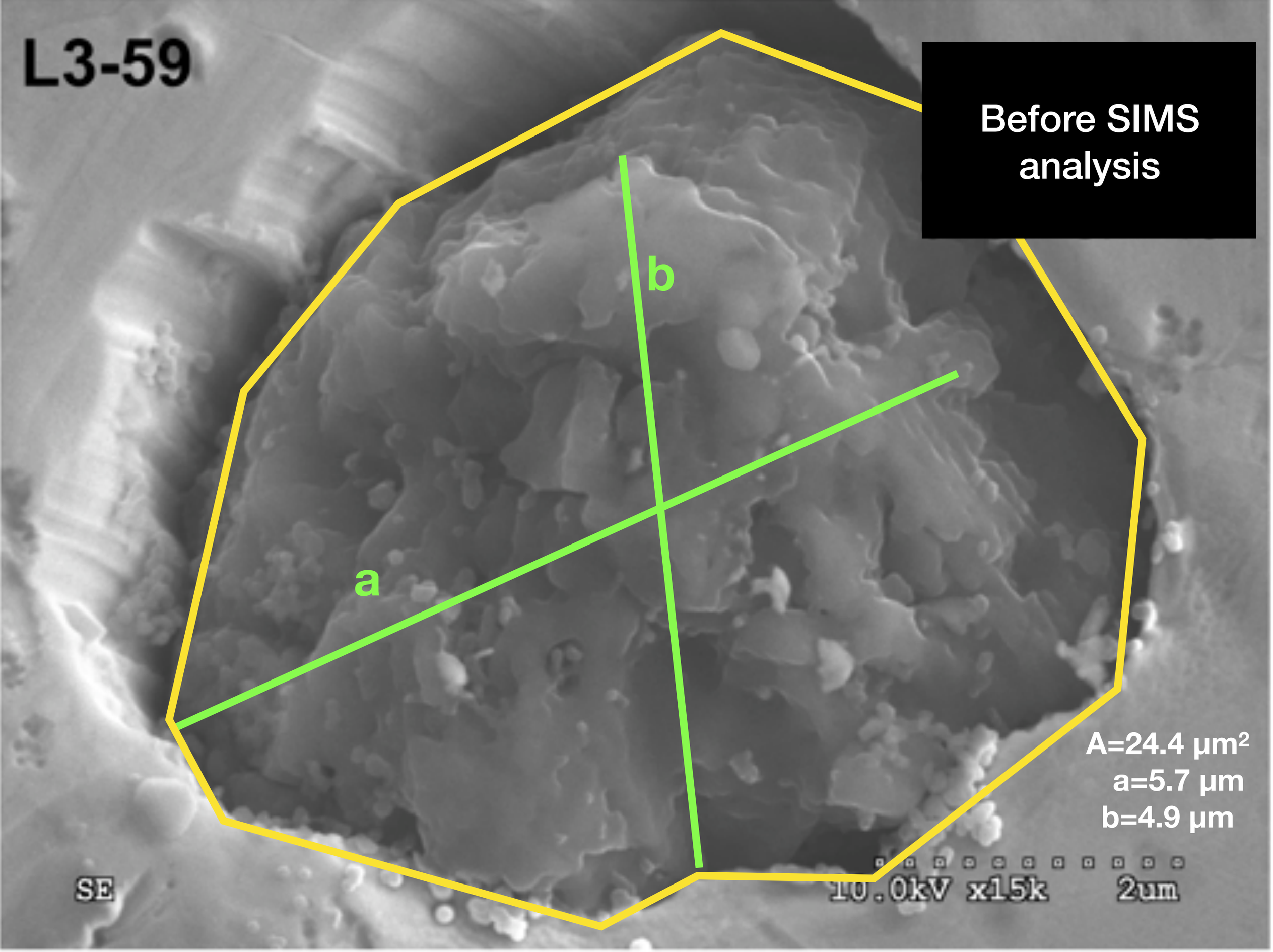
L3-59
Before SIMS analysis
b
a
A=24.4 µm²
a=5.7 µm
b=4.9 µm
SE
10.0kV x15k
2um

Before SHRIMP, after NanoSIMS

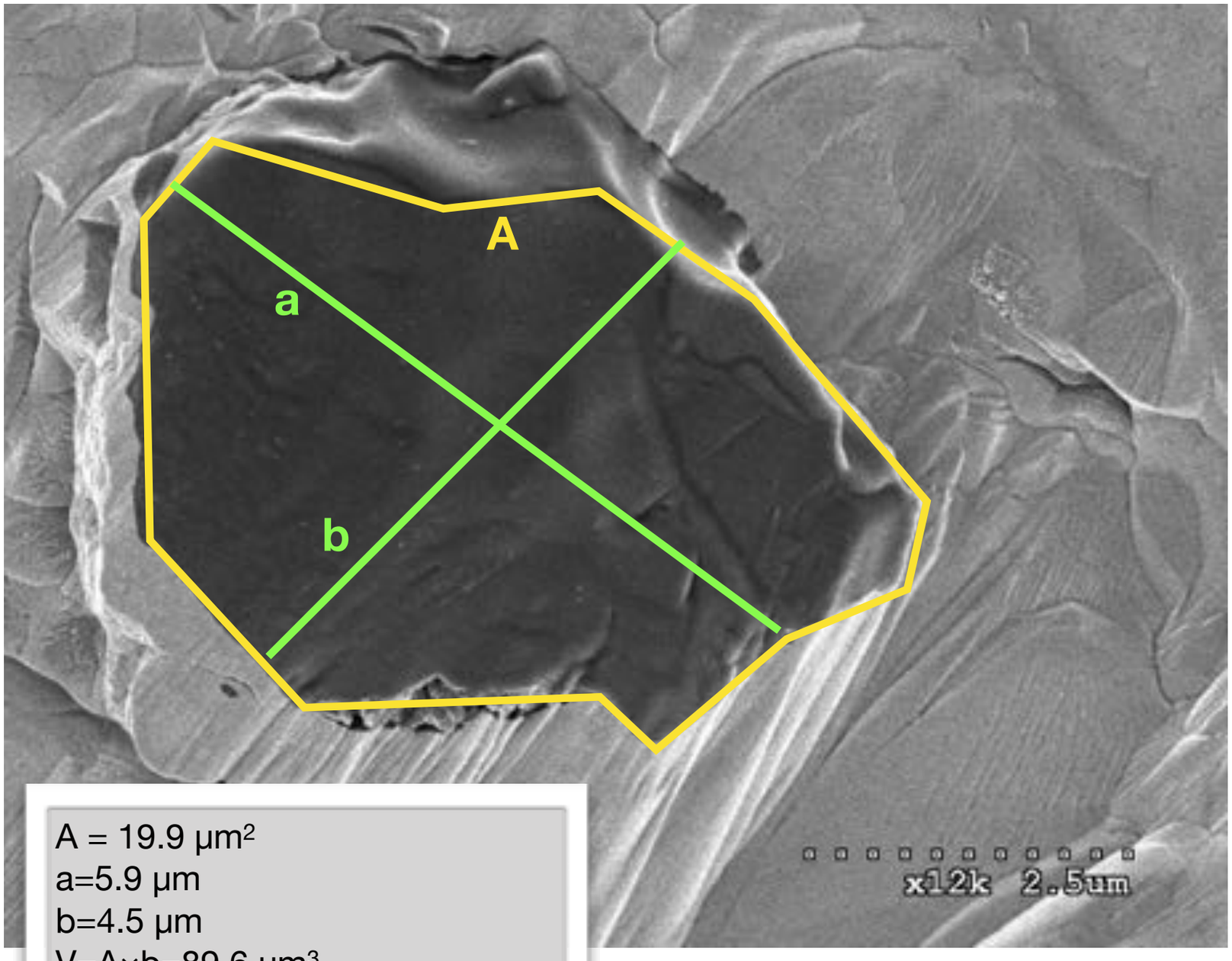

A = 19.9 μm^2
a=5.9 μm
b=4.5 μm
V=A×b=89.6 μm^3

ρ=~3.2 g cm^{-3}; (LS+LU fraction)
M=V×ρ=2.87E-10 g

L2_01

Before NanoSIMS

A = 102.1 μm^2
a=12.7 μm
b=9.2 μm
geometric mean diameter=10.2 μm
V=A×b=1044.4 μm^3

ρ=~3.2 g cm^{-3}; (LS+LU fraction)
M=V×ρ=3.34E-9 g

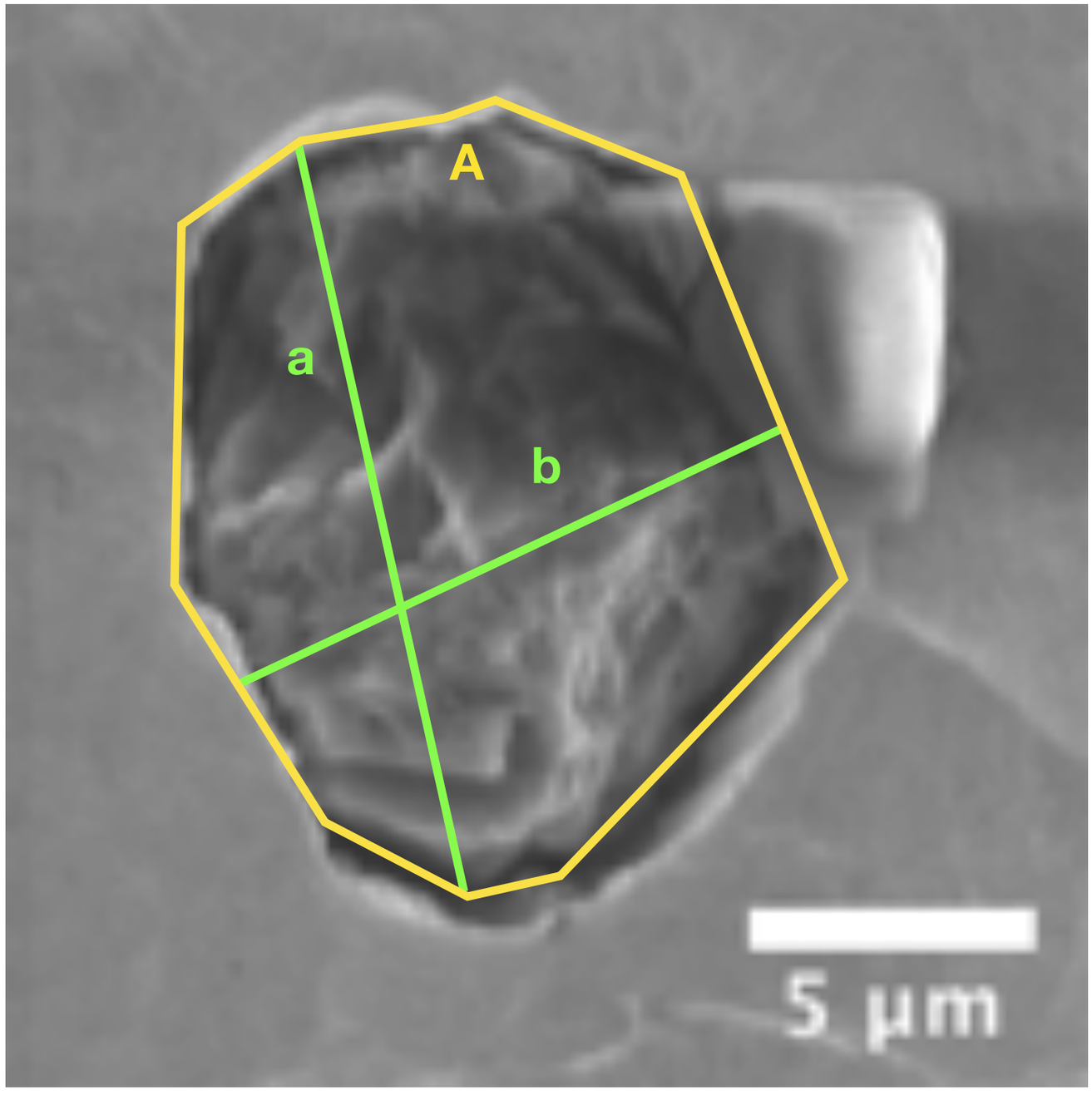

L2_02

Before NanoSIMS

A = 132.3 µm^2
a=14.6 µm
b=11.4 µm
geometric mean diameter=12.4 µm
V=A×b=1639.2 µm^3

ρ=~3.2 g cm^{-3}; (LS+LU fraction)
M=V×ρ=5.25E-9 g

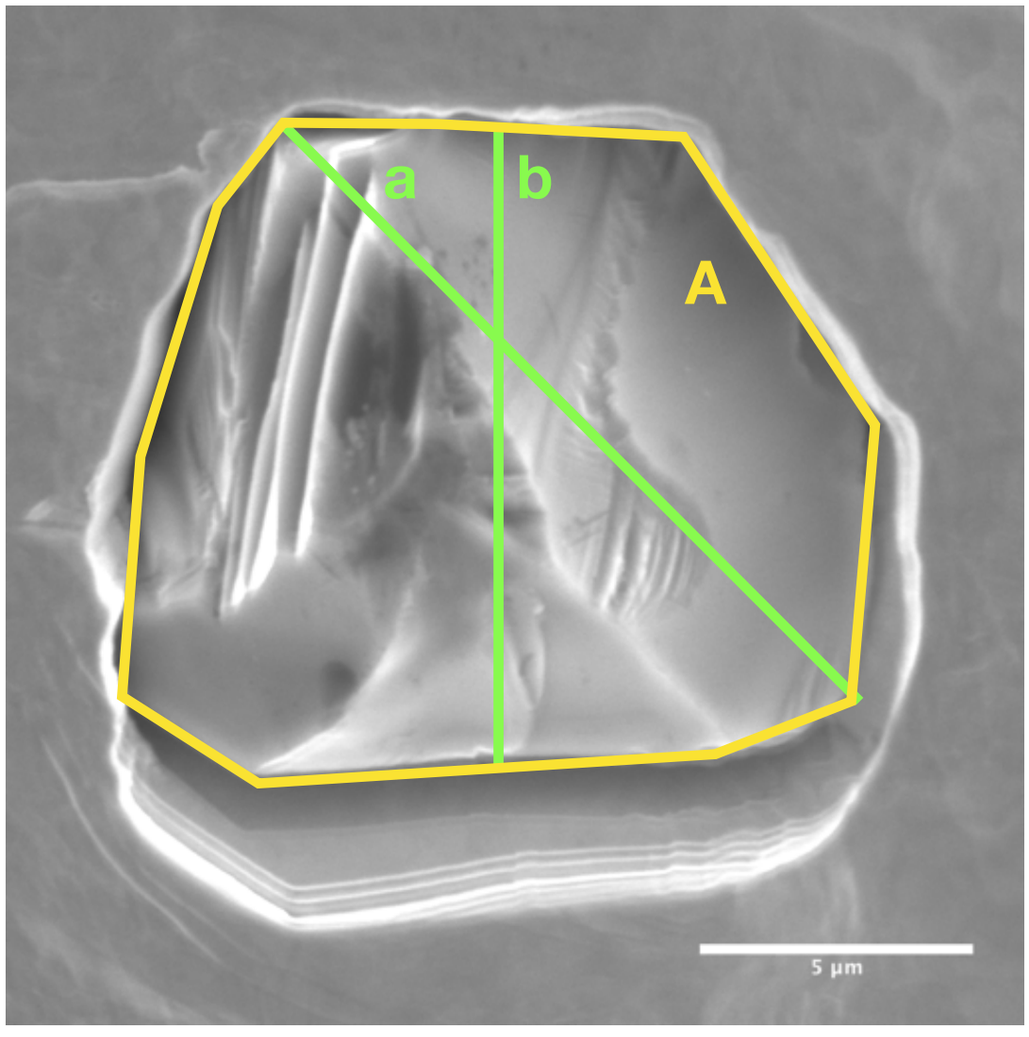

L2_03

Before NanoSIMS

A = 1323.9 μm^2
a=50.8 μm
b=28.0 μm
geometric mean diameter=34.1 μm
V=A×b=45210.1 μm^3

ρ=~3.2 g cm^{-3}; (LS+LU fraction)
M=V×ρ=1.45E-7 g

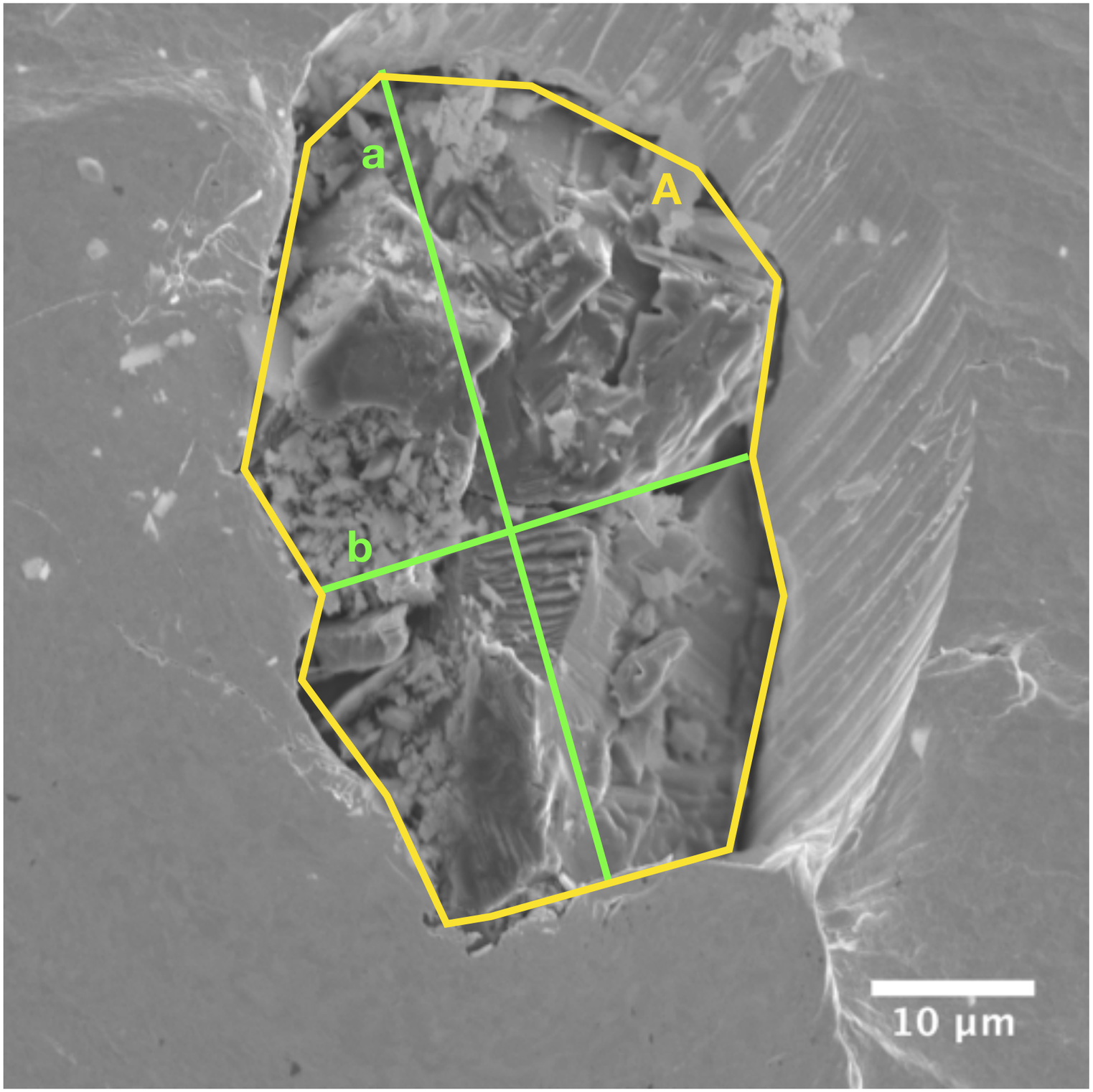

L2_04

Before NanoSIMS

A = 156.9 µm^2
a=15.9 µm
b=12.3 µm
geometric mean diameter=13.4 µm
V=A×b=2105.1 µm^3

ρ=~3.2 g cm^{-3}; (LS+LU fraction)
M=V×ρ=6.74E-9 g

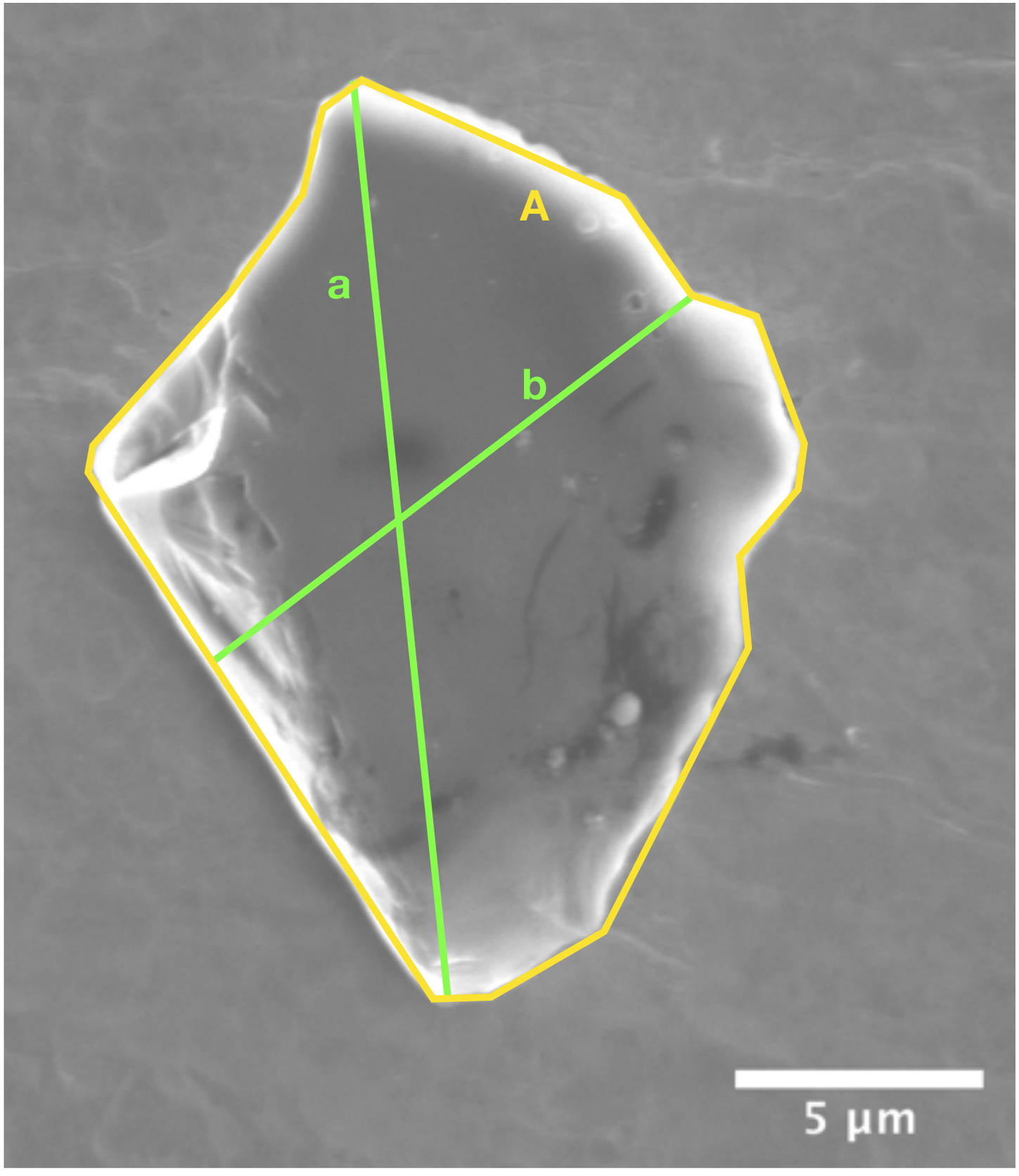

L2_05

Before NanoSIMS

A = 75.7 μm^2
a=13.1 μm
b=7.6 μm
geometric mean diameter=9.1 μm
V=A×b=691.1 μm^3

ρ=~3.2 g cm^{-3}; (LS+LU fraction)
M=V×ρ=2.21E-9 g

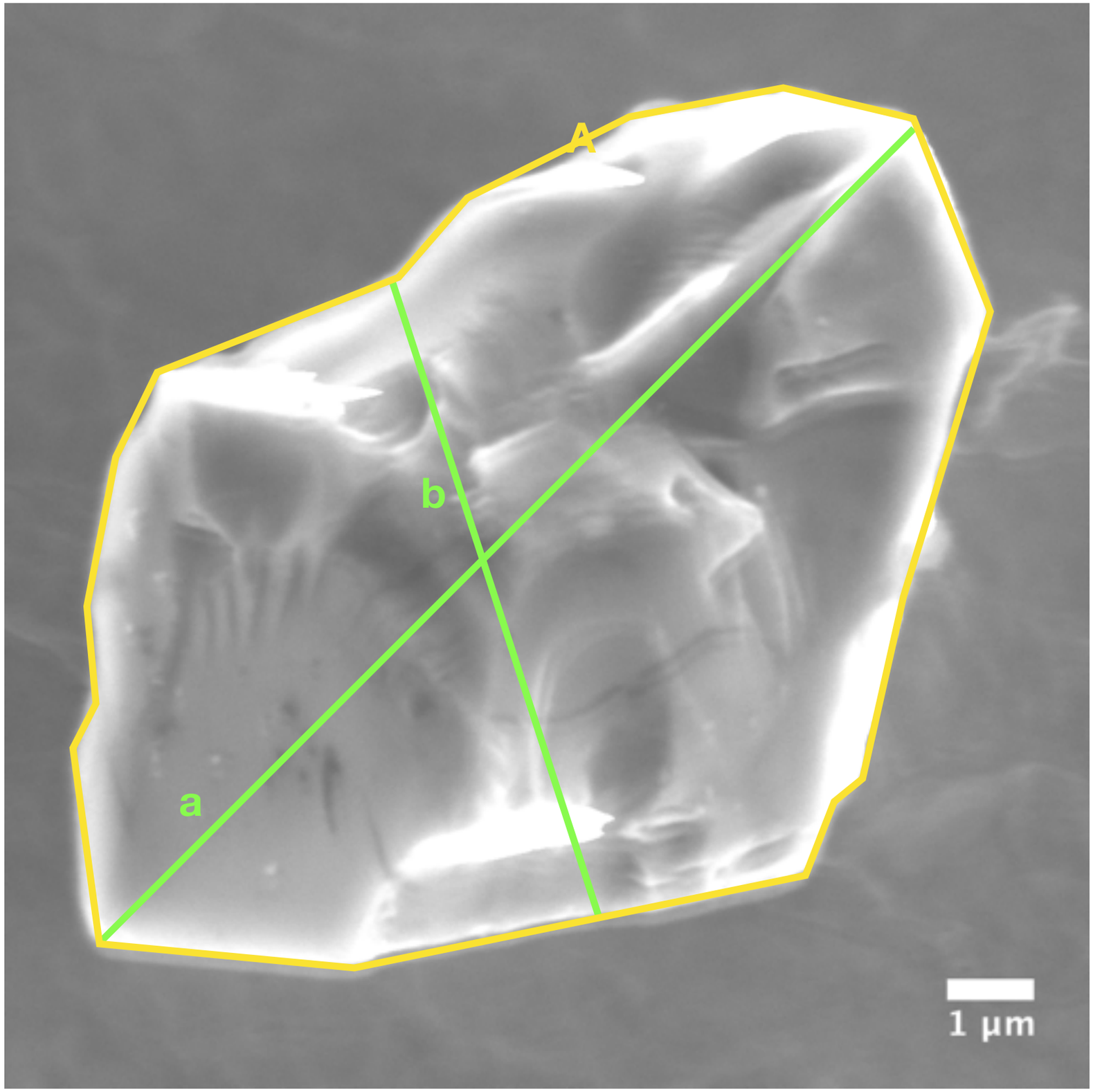

L2_06

Before NanoSIMS

A = 261.7 μm^2
a=24.0 μm
b=15.1 μm
geometric mean diameter=17.6 μm
V=A×b=4605.5 μm^3

ρ=~3.2 g cm^{-3}; (LS+LU fraction)
M=V×ρ=1.47E-8 g

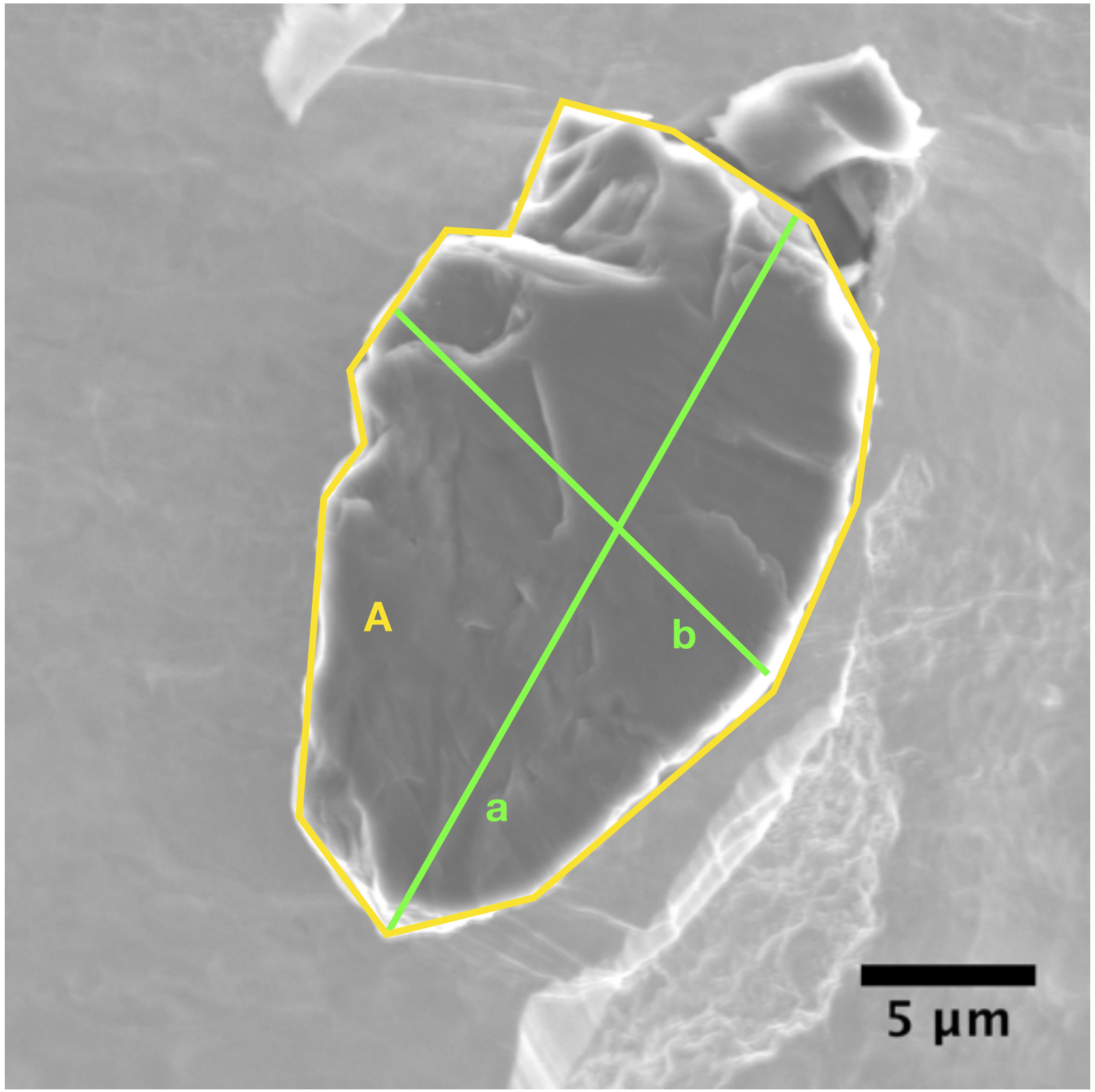

L2_07

Before NanoSIMS

A = 77.6 µm^2
a=14.4 µm
b=7.3 µm
geometric mean diameter=9.2 µm
V=A×b=713.8 µm^3

ρ=~3.2 g cm^{-3}; (LS+LU fraction)
M=V×ρ=2.28E-9 g

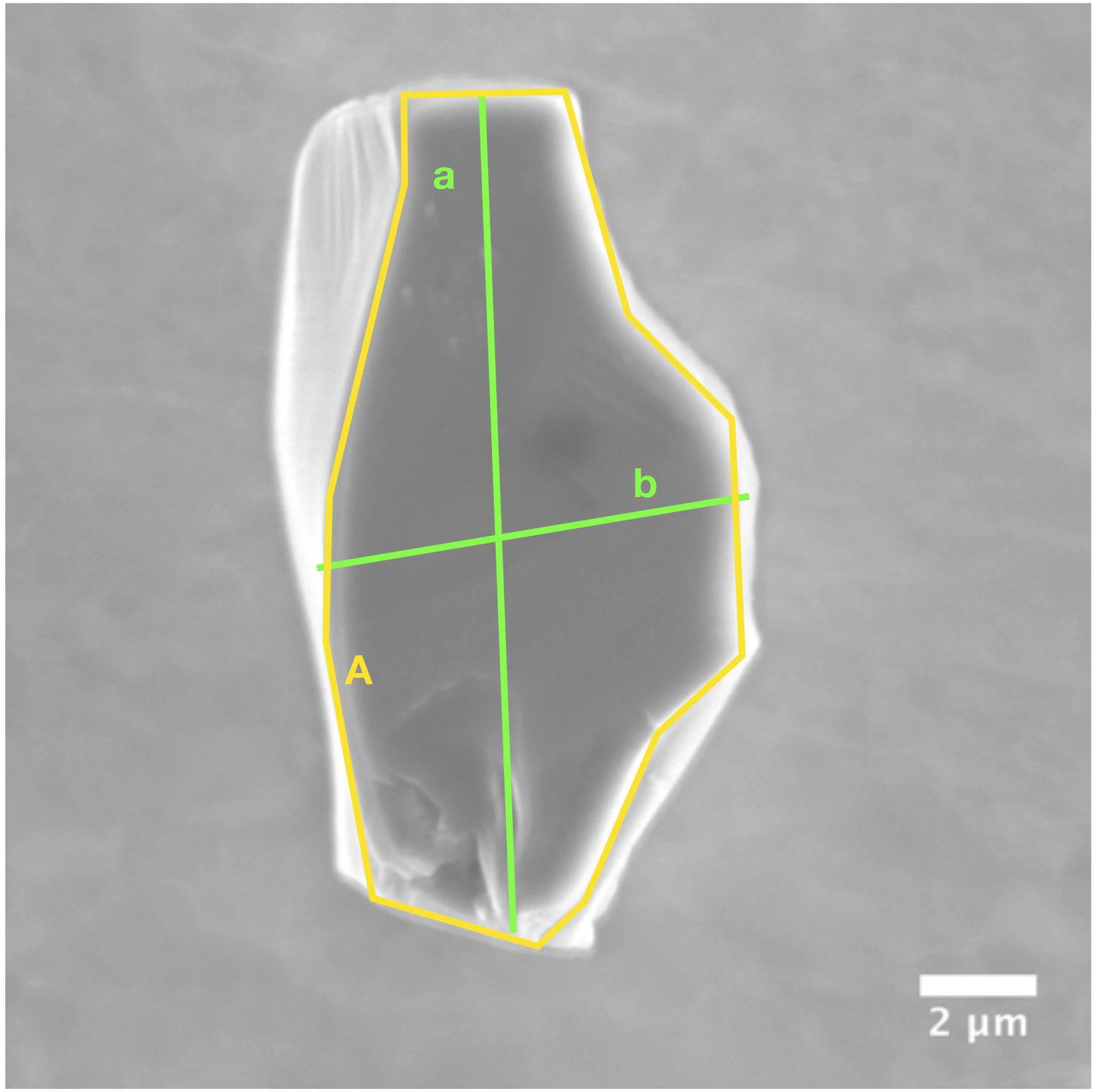

L2_08

Before NanoSIMS

A = 330.4 μm^2
a=31.9 μm
b=15.7 μm
geometric mean diameter=19.9 μm
V=A×b=6562.6 μm^3

ρ=~3.2 g cm^{-3}; (LS+LU fraction)
M=V×ρ=2.10E-8 g

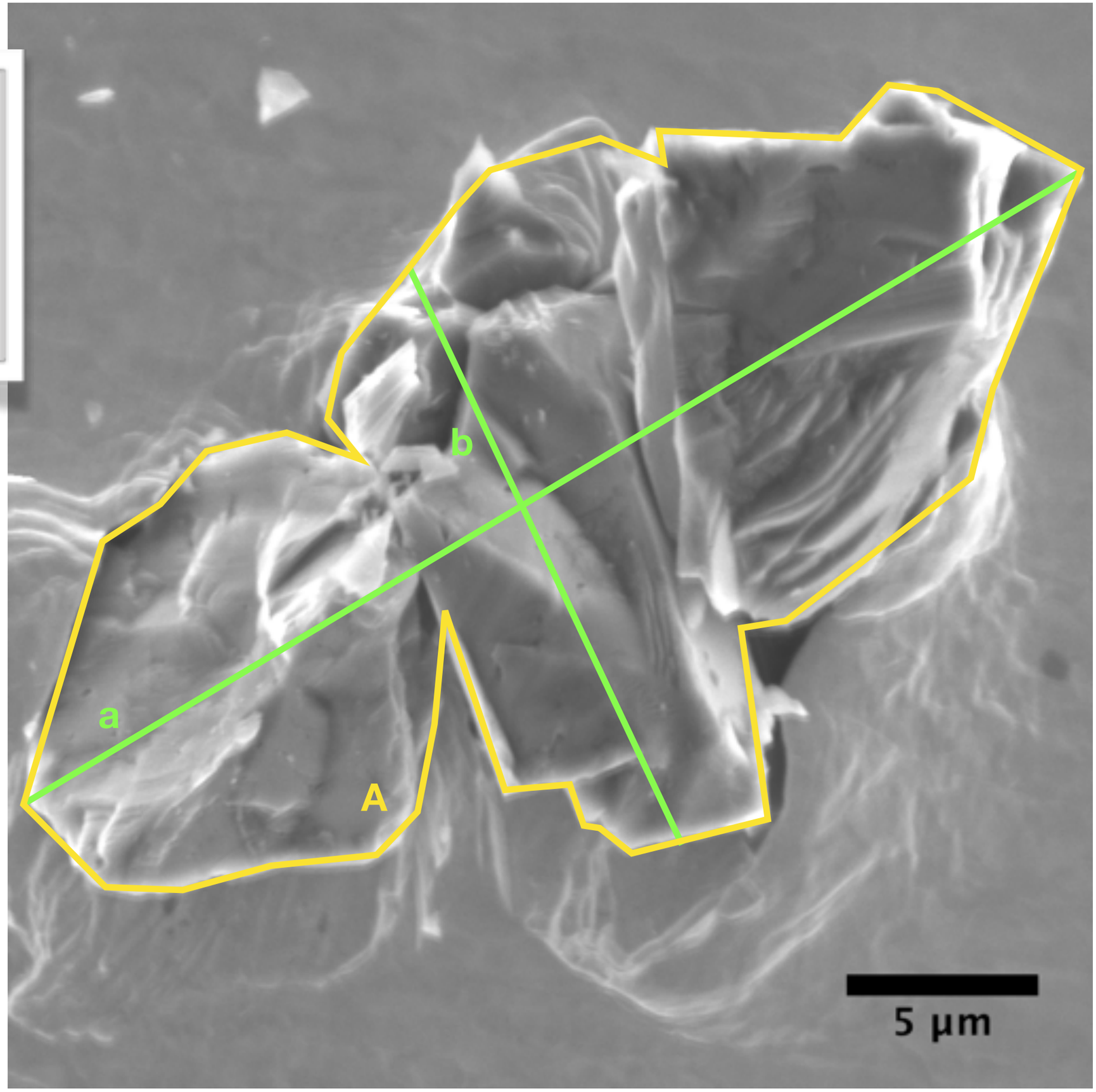

L2_09

Before NanoSIMS

A = 132.5 µm^2
a=18.6 µm
b=9.5 µm
geometric mean diameter=11.9 µm
V=A×b=1579.9 µm^3

ρ=~3.2 g cm^{-3}; (LS+LU fraction)
M=V×ρ=5.06E-9 g

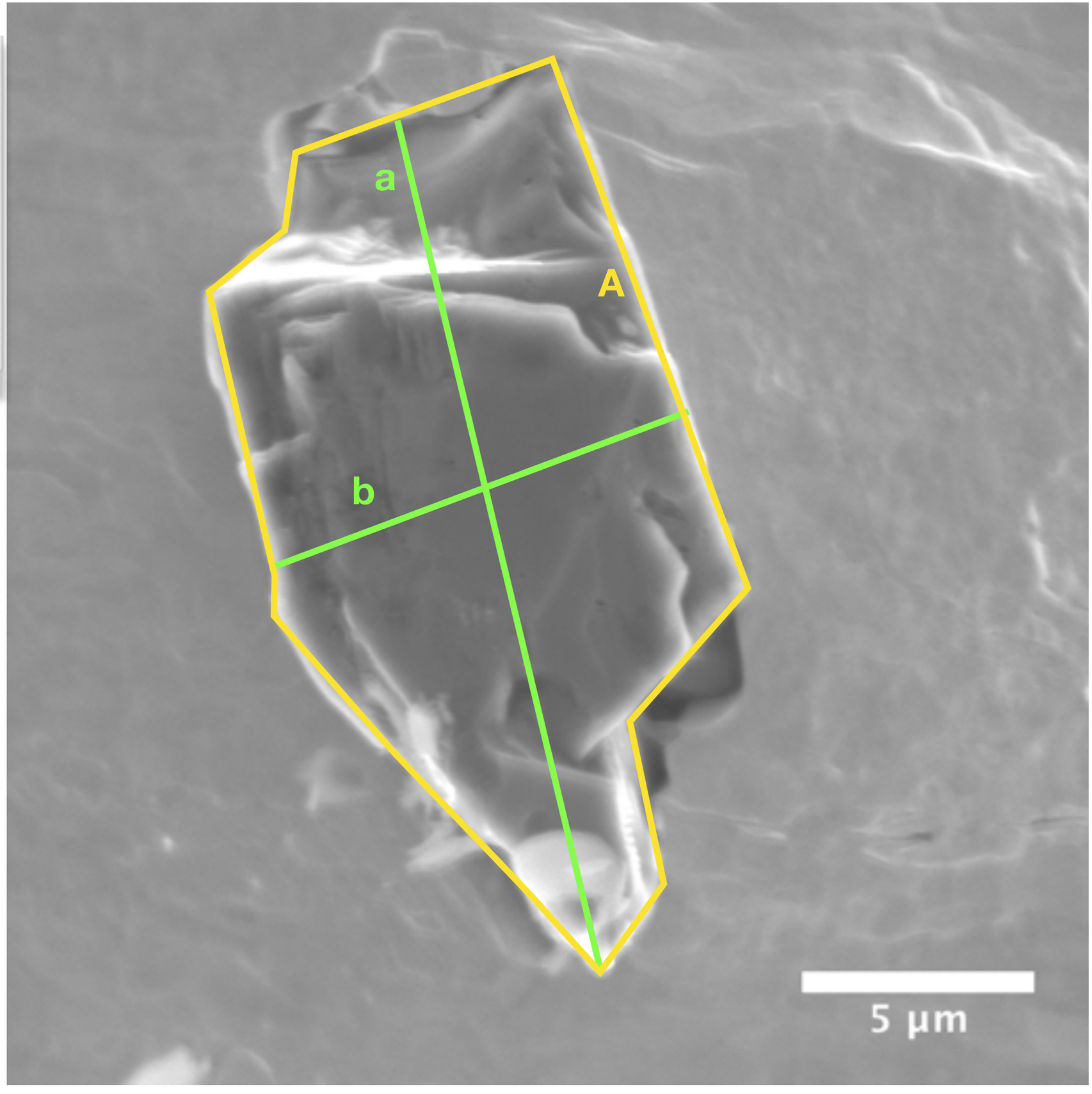

L2_10

Before NanoSIMS

A = 74.2 µm^2
a=10.0 µm
b=9.1 µm
geometric mean diameter=9.4 µm
V=A×b=695.8 µm^3

ρ=~3.2 g cm^{-3}; (LS+LU fraction)
M=V×ρ=2.23E-9 g

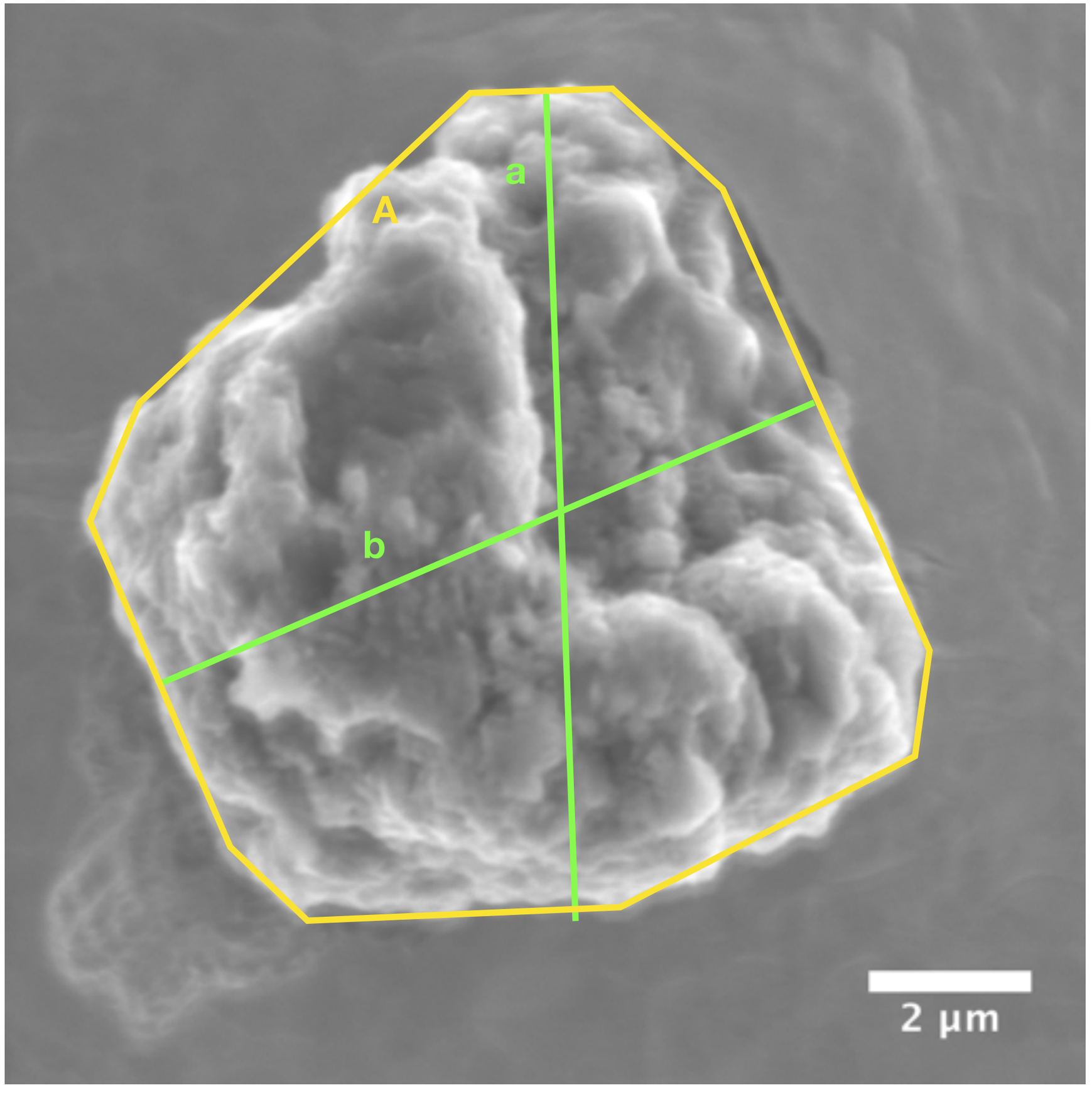

L2_11

Before NanoSIMS

A = 118.2 μm^2
a=11.9 μm
b=11.8 μm
geometric mean diameter=11.8 μm
V=A×b=1398.1 μm^3

ρ=~3.2 g cm^{-3}; (LS+LU fraction)
M=V×ρ=4.47E-9 g

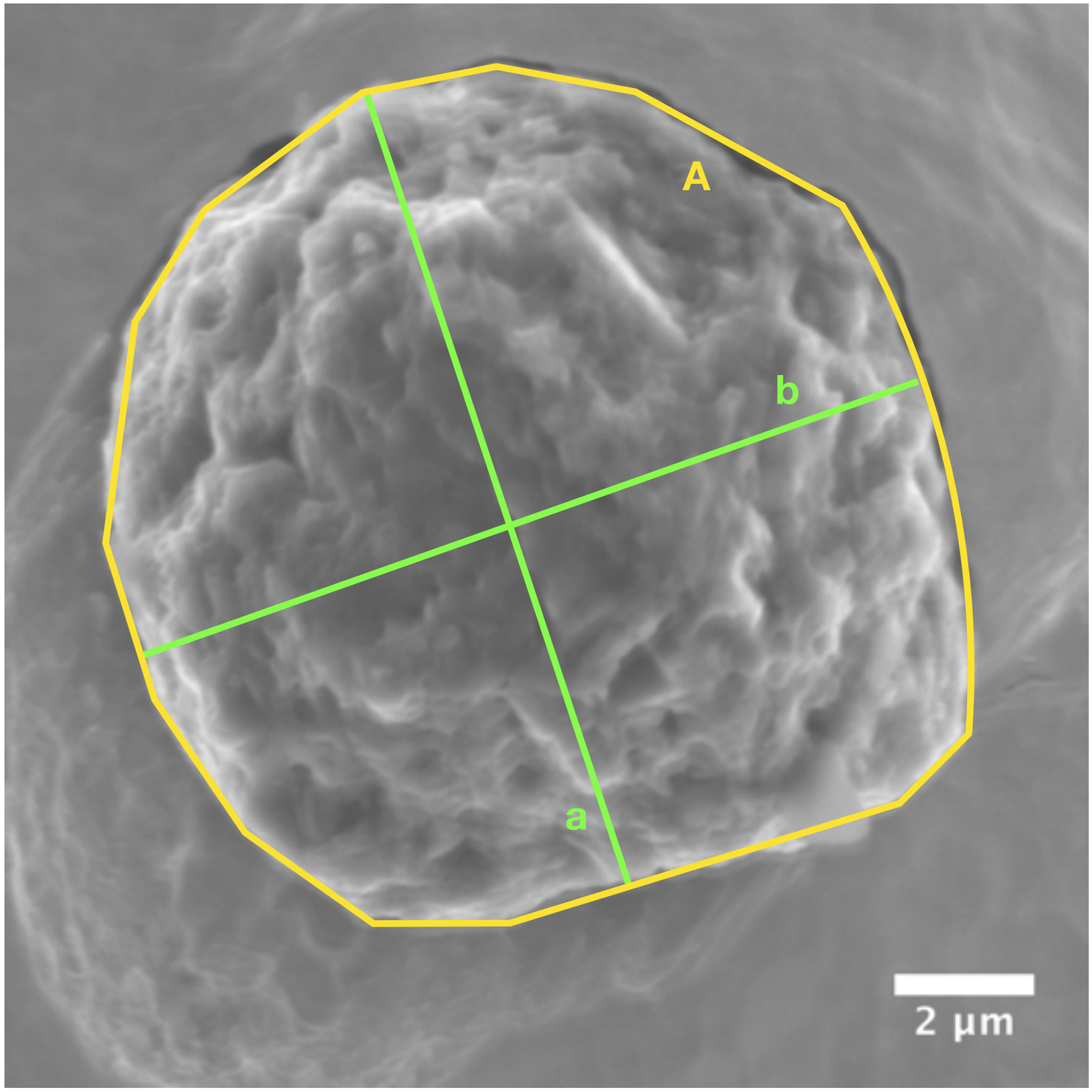

L2_12

Before NanoSIMS

A = 111.6 µm^2
a=12.9 µm
b=11.2 µm
geometric mean diameter=11.7 µm
V=A×b=1308.0 µm^3

ρ=~3.2 g cm^{-3}; (LS+LU fraction)
M=V×ρ=4.19E-9 g

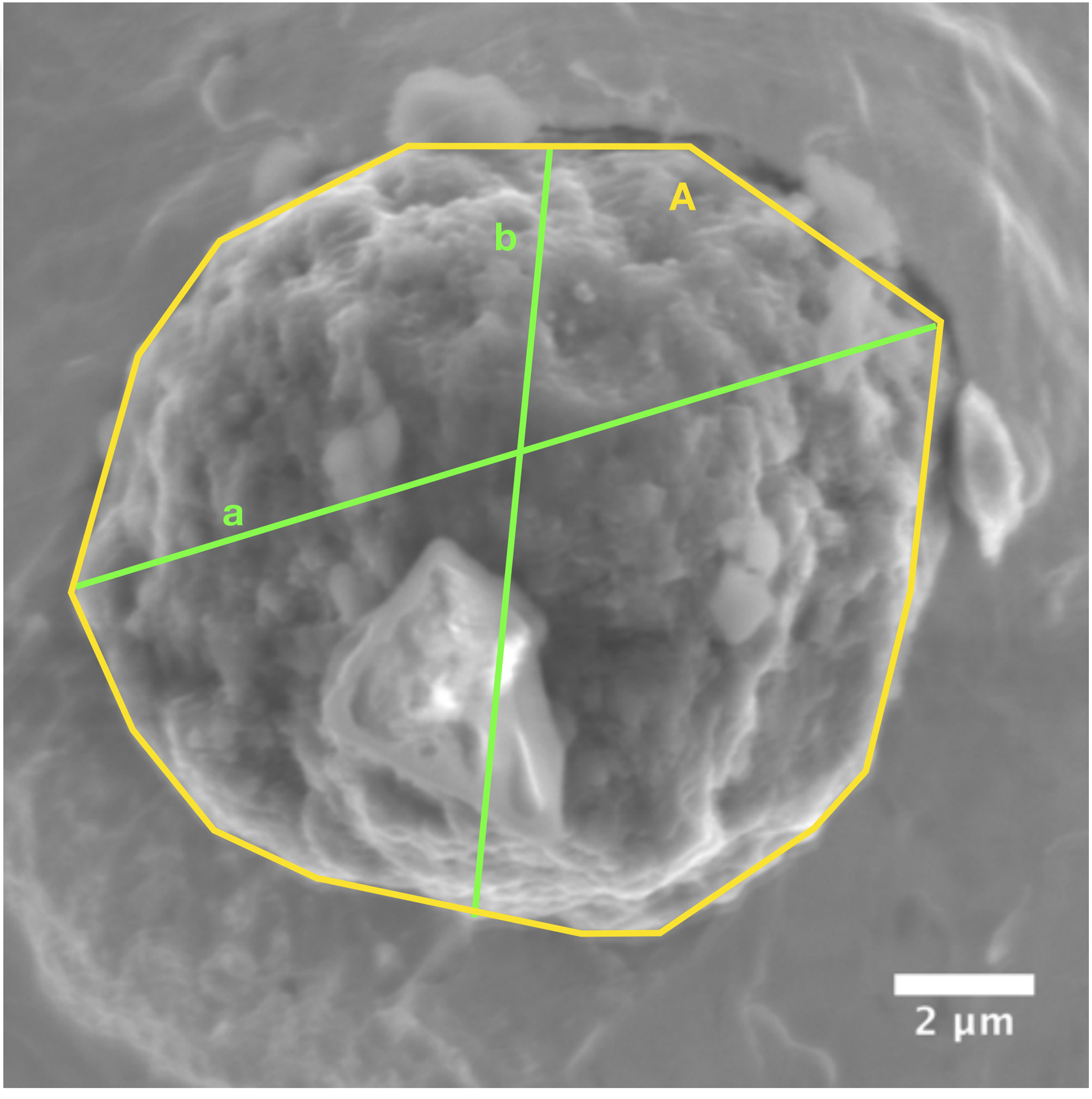

L2_13

Before NanoSIMS

A = 50.4 μm^2
a=8.5 μm
b=7.6 μm
geometric mean diameter=7.9 μm
V=A×b=396.4 μm^3

ρ=~3.2 g cm^{-3}; (LS+LU fraction)
M=V×ρ=1.27E-9 g

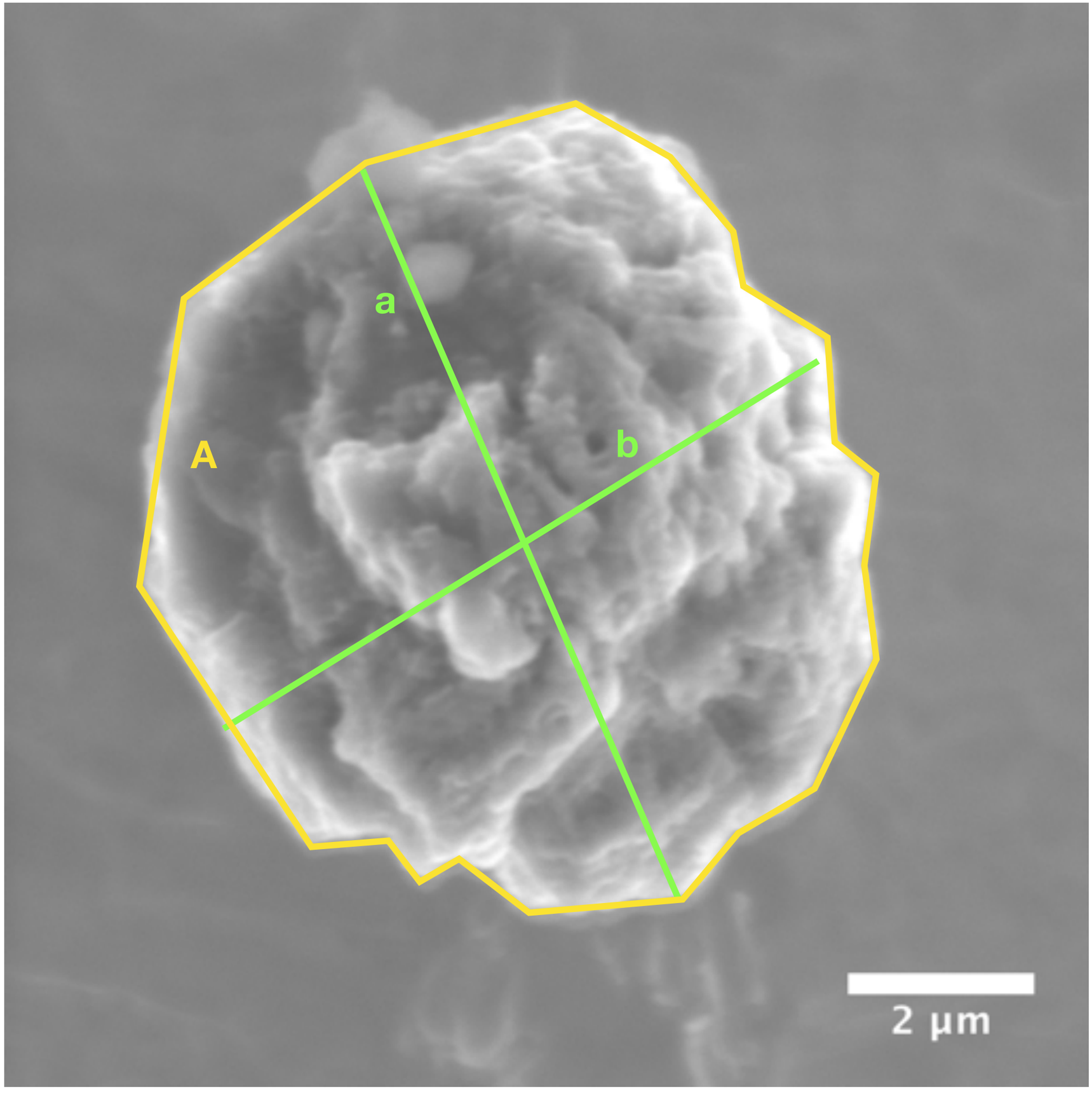

L2_14

Before NanoSIMS

A = 93.8 μm^2
a=13.2 μm
b=9.5 μm
geometric mean diameter=10.6 μm
V=A×b=993.9 μm^3

ρ=~3.2 g cm^{-3}; (LS+LU fraction)
M=V×ρ=3.18E-9 g

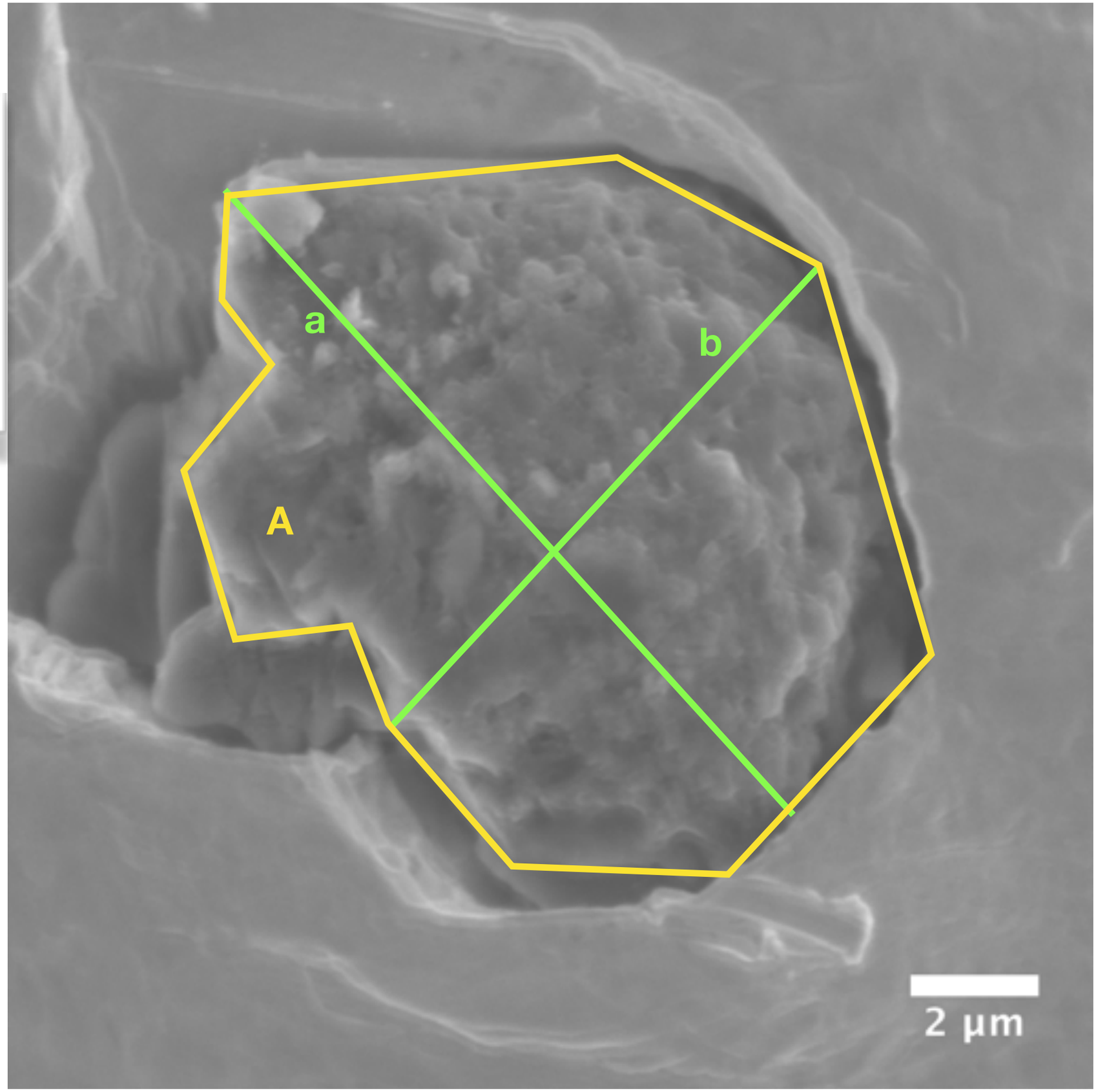

L2_15

Before NanoSIMS

A = 56.8 μm^2
a=10.7 μm
b=7.4 μm
geometric mean diameter=8.4 μm
V=A×b=476.0 μm^3

ρ=~3.2 g cm^{-3}; (LS+LU fraction)
M=V×ρ=1.52E-9 g

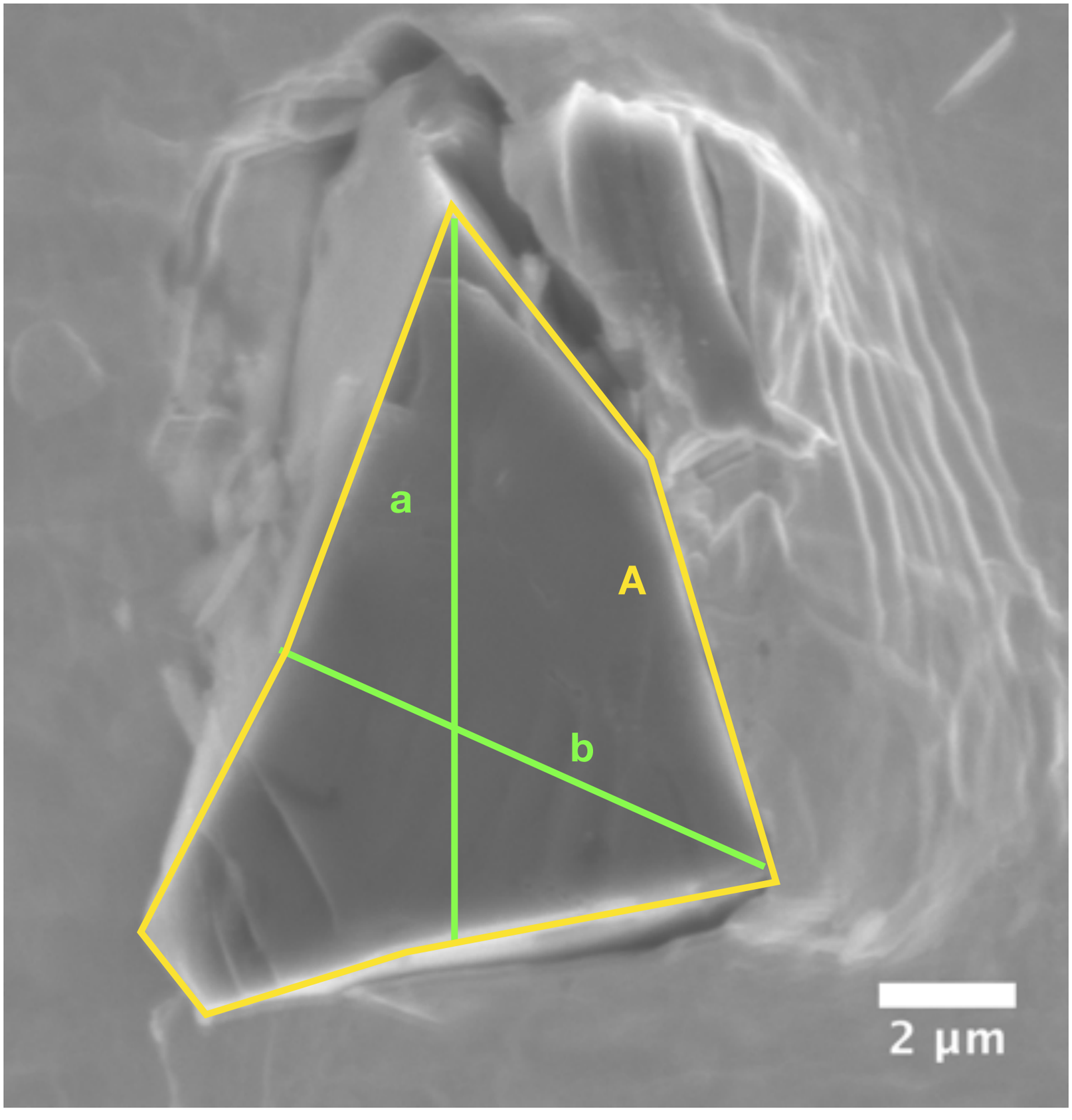

L2_16

Before NanoSIMS

A = 114.6 µm^2
a=17.6 µm
b=8.4 µm
geometric mean diameter=10.7 µm
V=A×b=1231.0 µm^3

ρ=~3.2 g cm^{-3}; (LS+LU fraction)
M=V×ρ=3.94E-9 g

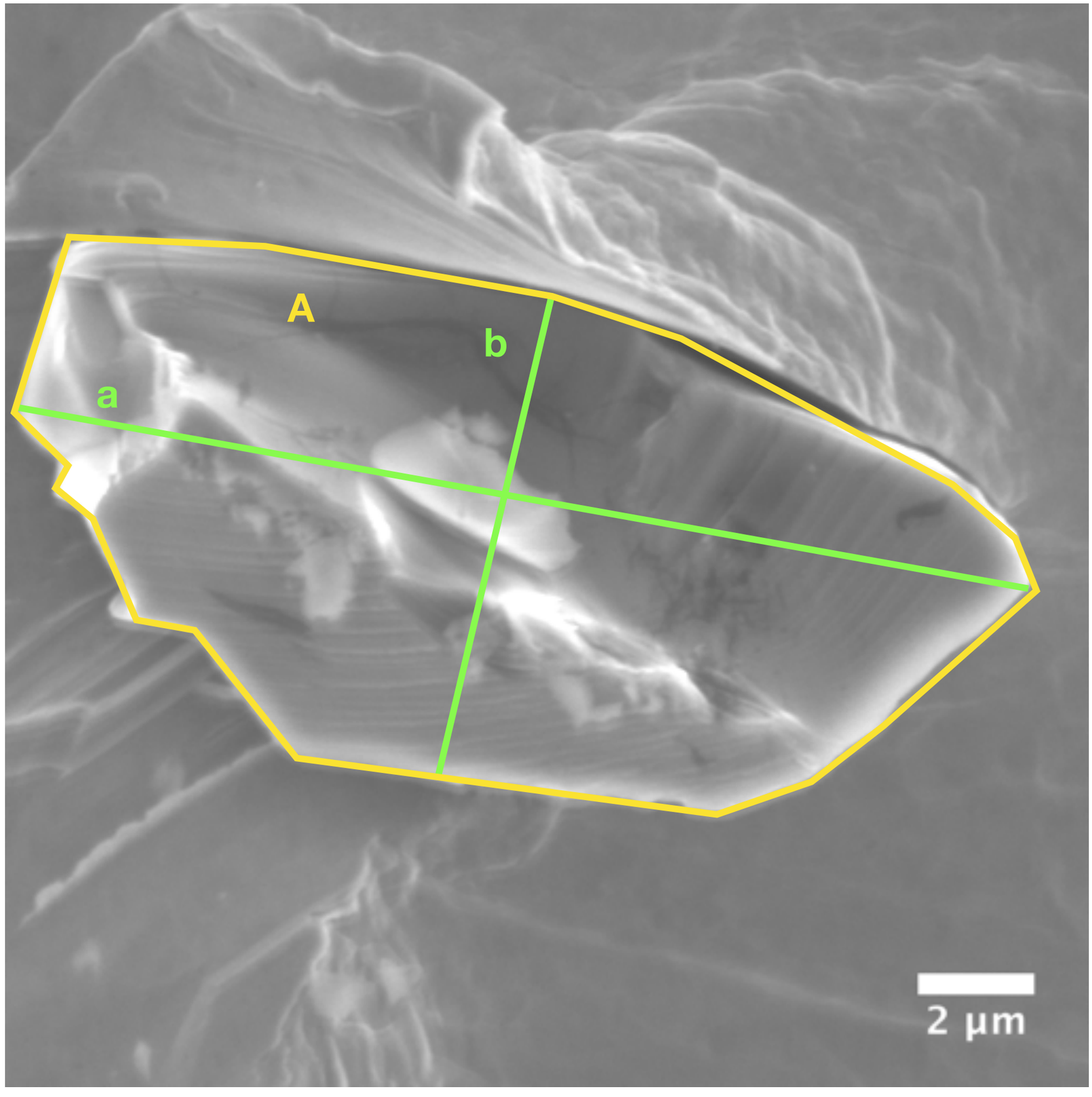

L2_17

Before NanoSIMS

A = 121.8 µm^2
a=16.4 µm
b=9.7 µm
geometric mean diameter=11.6 µm
V=A×b=1409.3 µm^3

ρ=~3.2 g cm^{-3}; (LS+LU fraction)
M=V×ρ=4.51E-9 g

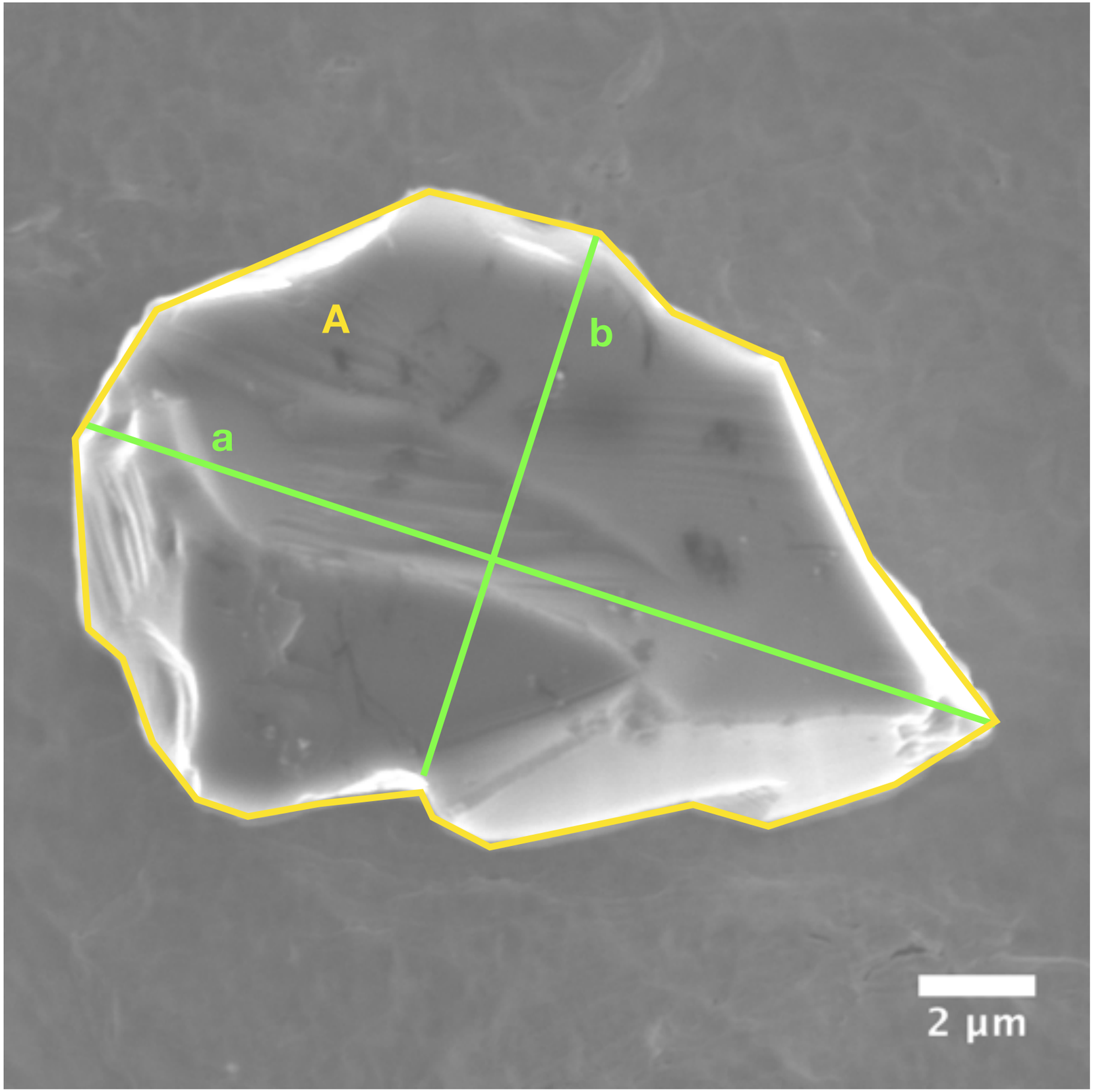

L2_18

Before NanoSIMS

A_1 = 544.8 µm²
a_1=26.8 µm
b_1=24.8 µm
$V_1=A_1 \times b_1$=13859.5 µm³

ρ=~3.2 g cm⁻³; (LS+LU fraction)
$M_1=V_1 \times \rho$=4.46E-8 g

A_2 = 73.7 µm²
a_2=22.8 µm
b_2=4.5 µm
$V_2=A_2 \times b_2$=331.65 µm³

ρ=~3.2 g cm⁻³; (LS+LU fraction)
$M_2=V_2 \times \rho$=1.83E-10 g

geometric mean diameter=25.4 µm
A_{1+2}=69.3 µm²
V_{1+2}=300 µm³
M_{1+2}=4.64E-8 g

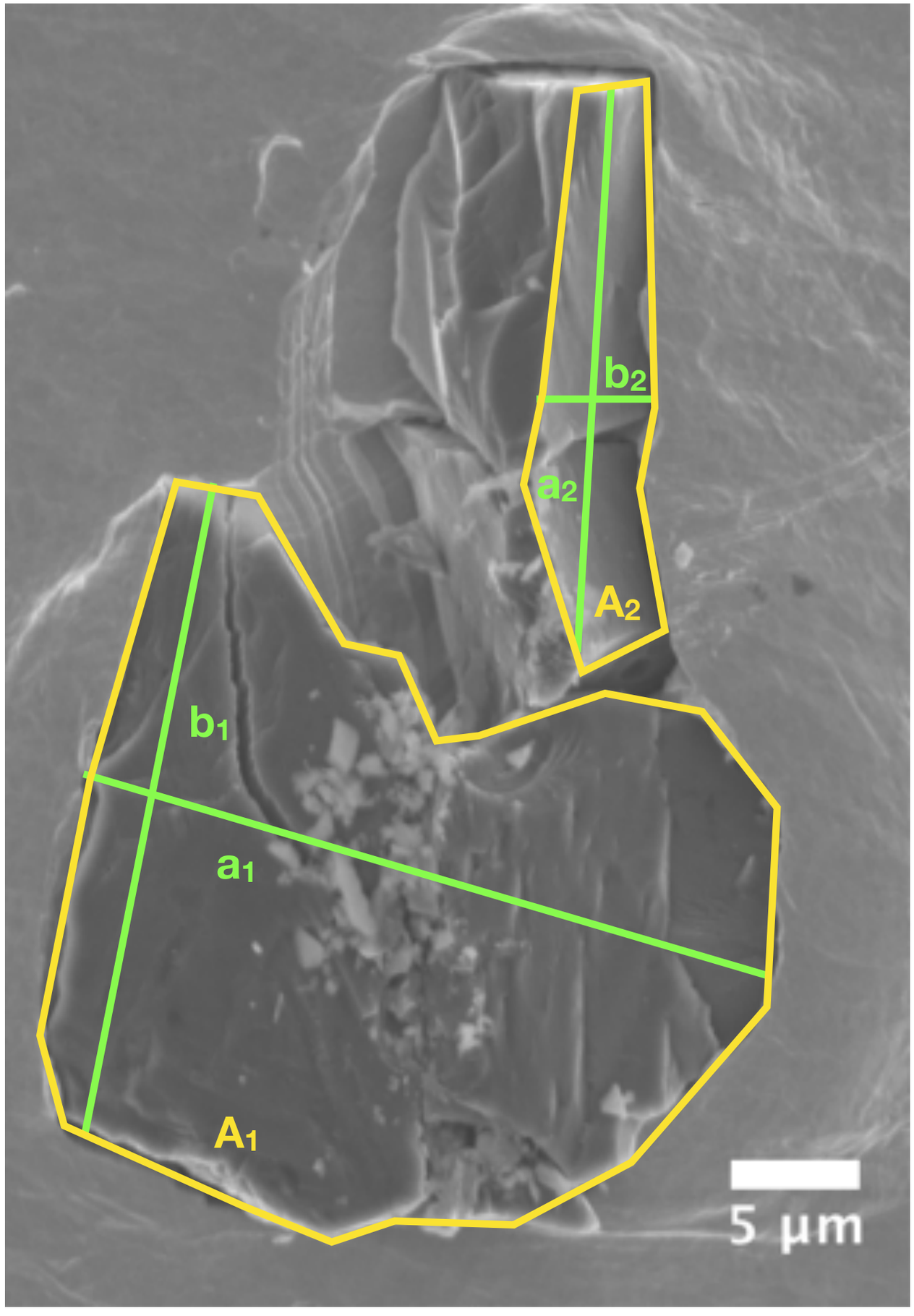

L2_19

Before NanoSIMS

A = 71.8 μm^2
a=10.3 μm
b=8.8 μm
geometric mean diameter=9.3 μm
V=A×b=665.6 μm^3

ρ=~3.2 g cm^{-3}; (LS+LU fraction)
M=V×ρ=2.13E-9 g

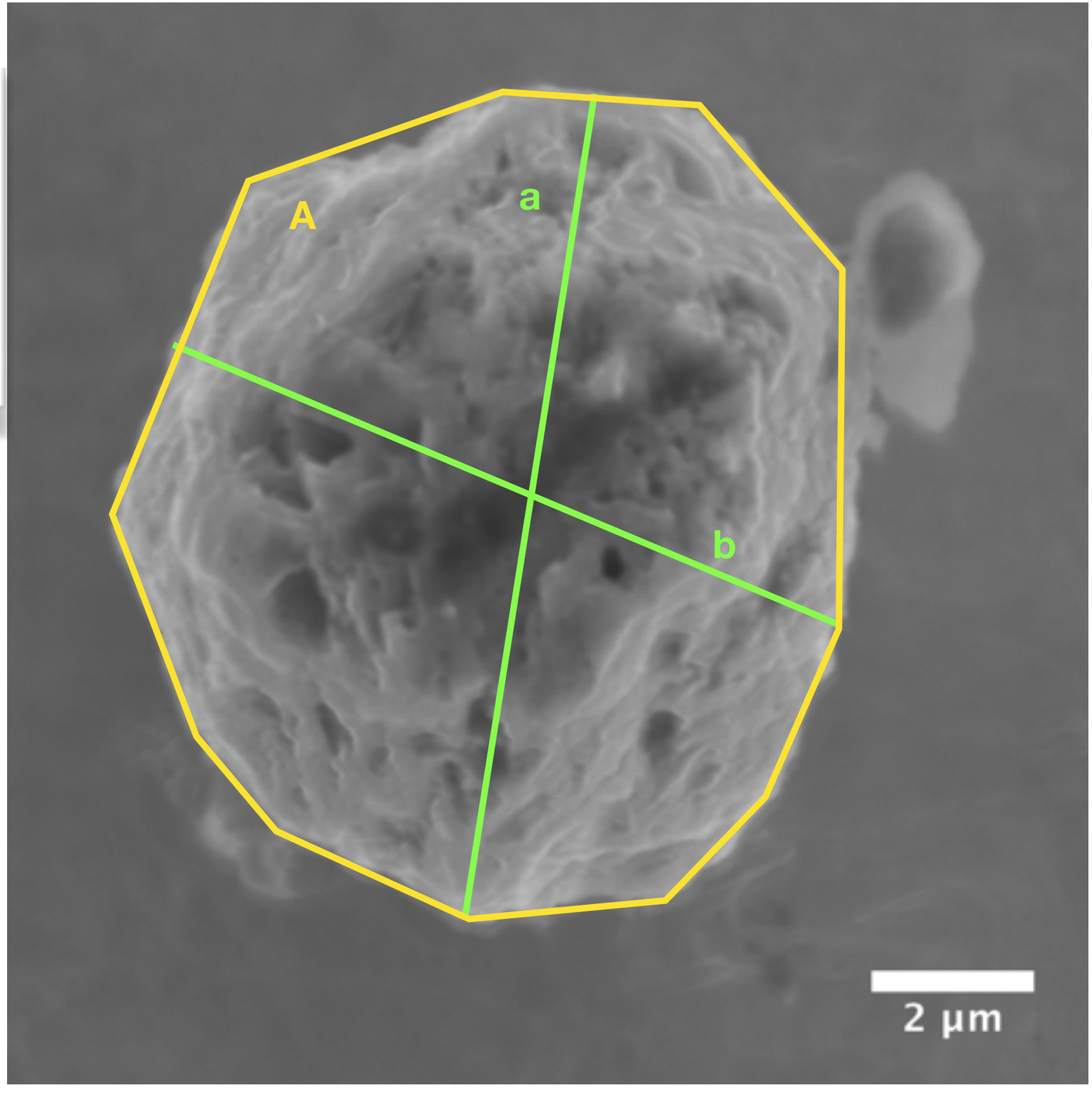

L2_25

Before NanoSIMS

A = 18.2 μm^2
a=5.6 μm
b=3.7 μm
geometric mean diameter=4.3 μm
V=A×b=77.8 μm^3

ρ=~3.2 g cm^{-3}; (LS+LU fraction)
M=V×ρ=2.49E-10 g

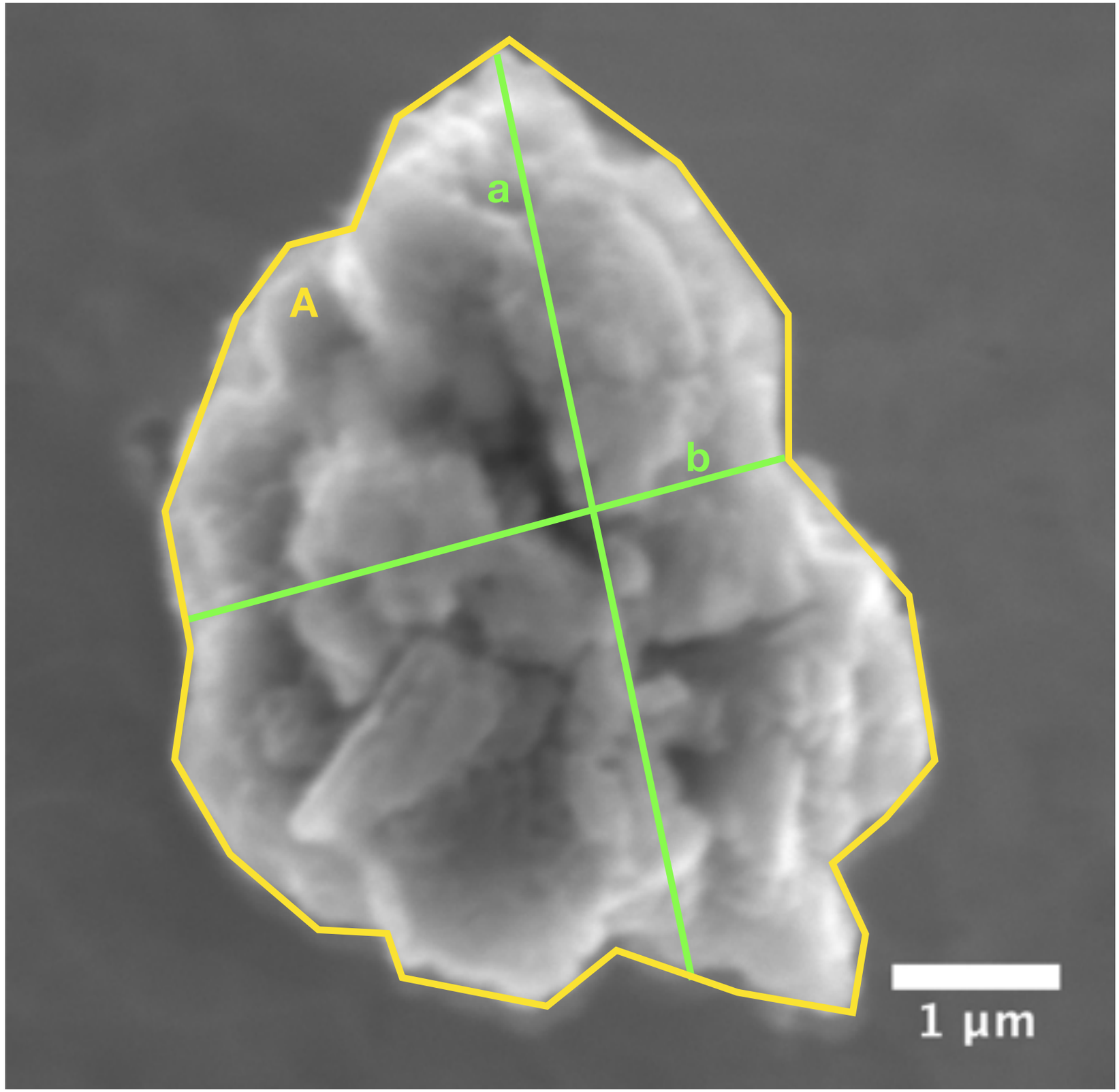

L2_27

Before NanoSIMS

A = 3.6 μm^2
a=2.5 μm
b=1.8 μm
geometric mean diameter=2.0 μm
V=A×b=179.9 μm^3

ρ=~3.2 g cm^{-3}; (LS+LU fraction)
M=V×ρ=2.26-11 g

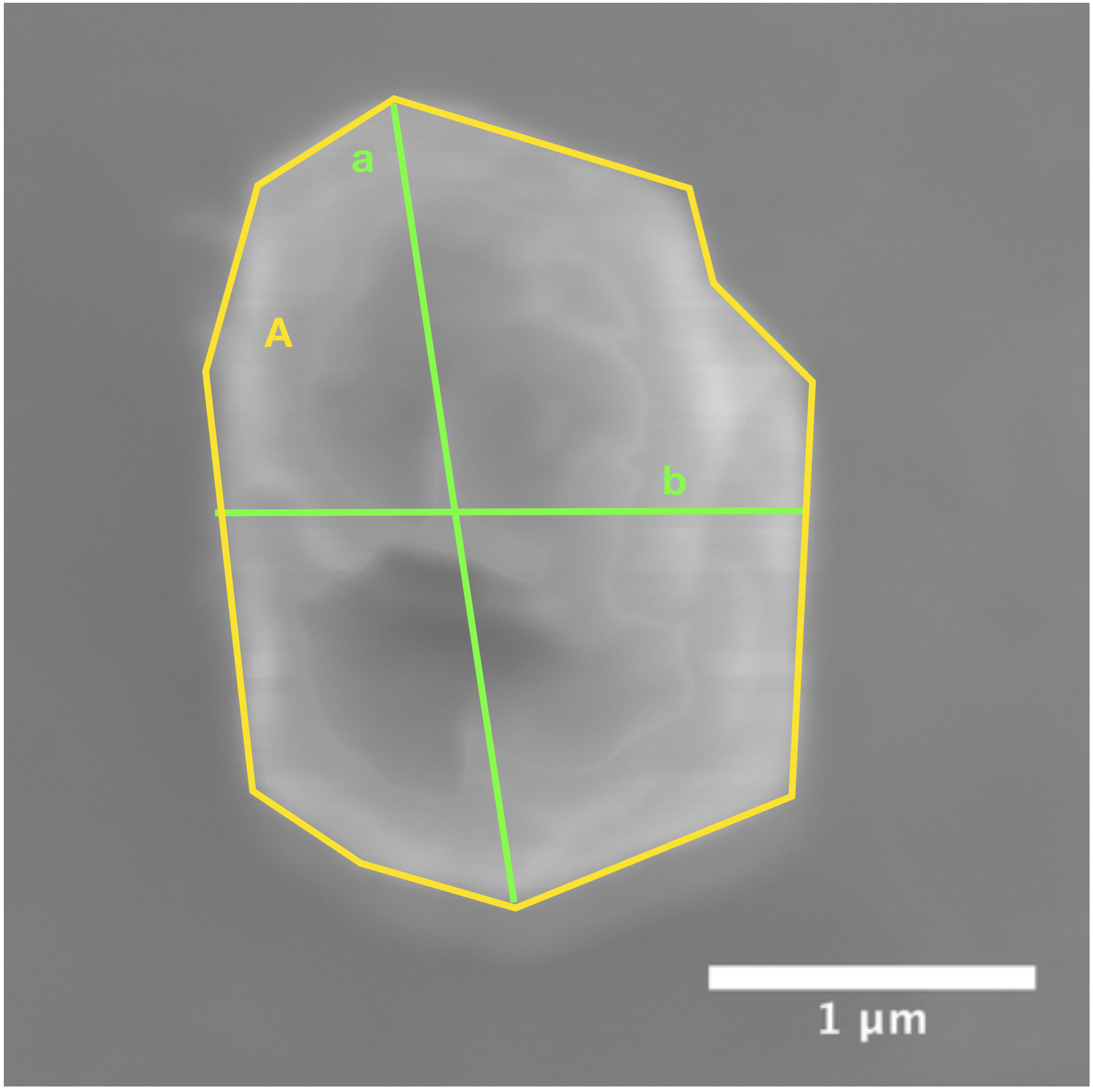

L2_57

Before NanoSIMS

A = 30.2 μm^2
a=6.2 μm
b=5.8 μm
geometric mean diameter=6.0 μm
V=A×b=179.9 μm^3

ρ=~3.2 g cm^{-3}; (LS+LU fraction)
M=V×ρ=5.76E-10 g